State Estimation and Multivariate Process Monitoring in Multiscale Framework

By

SHRENIK B. PATEL

ENGG 01201404022

Bhabha Atomic Research Centre, Mumbai

A thesis submitted to the

Board of Studies in Engineering Sciences

In partial fulfillment of requirements
for the Degree of

DOCTOR OF PHILOSOPHY

of

HOMI BHABHA NATIONAL INSTITUTE

April, 2021

Homi Bhabha National Institute[1]

Recommendations of the Viva Voce Committee

As members of the Viva Voce Committee, we certify that we have read the dissertation prepared by *Shri. Shrenik B. Patel* entitled "*State Estimation and Multivariate Process Monitoring in Multiscale Framework*" and recommend that it may be accepted as fulfilling the thesis requirement for the award of Degree of Doctor of Philosophy.

Viva Voce Committee	Signature	Date
Chairman: Dr. Archana Sharma	Archana	10/04/2021
Guide / Convener: Dr. A.P. Tiwari		10/04/2021
Co-guide & Tech. Advisor: Dr. S. Mukhopadhyay		10/04/2021
Examiner: Dr. Ravindra Gudi		10/04/2021
Member 1: Dr. V.H. Patankar	V.H. Patankar	10/04/2021
Member 2: Dr. Gopika Vinod		10/04/2021
Member 3: Dr. B. Dikshit	B. Dikshit	10/04/2021

Final approval and acceptance of this thesis is contingent upon the candidate's submission of the final copies of the thesis to HBNI.

I/We hereby certify that I/we have read this thesis prepared under my/our direction and recommend that it may be accepted as fulfilling the thesis requirement.

Date: 10/04/2021

Place: Mumbai

(S MUKHOPADHYAY) 21/05/2021 — **Signature** — **Co-guide (if any)**

(A P TIWARI) 21/5/21 — **Signature** — **Guide**

[1] This page is to be included only for final submission after successful completion of viva voce.

STATEMENT BY AUTHOR

This thesis has been submitted in partial fulfillment of requirements for an advanced degree at Homi Bhabha National Institute (HBNI) and is deposited in the Library to be made available to borrowers under rules of the HBNI.

Brief quotations from this thesis are allowable without special permission, provided that accurate acknowledgement of source is made. Requests for permission for extended quotation from or reproduction of this manuscript in whole or in part may be granted by the Competent Authority of HBNI when in his or her judgment the proposed use of the material is in the interests of scholarship. In all other instances, however, permission must be obtained from the author.

Shrenik B. Patel
ENGG 01201404022

DECLARATION

I, hereby declare that the investigation presented in the thesis has been carried out by me. The work is original and has not been submitted earlier as a whole or in part for a degree / diploma at this or any other Institution / University.

Shrenik B. Patel
ENGG 01201404022

List of Publications arising from the thesis

Journals (Published)

1. Shrenik B. Patel, S. Mukhopadhyay, A.P. Tiwari, "Estimation of reactivity and delayed neutron precursors' concentrations using a multiscale extended Kalman filter ", *Annals of Nuclear Energy*, vol. 111, pp. 666-675, 2018. (I.F.=1.380, *ANE*)

2. T. U. Bhatt, S. B. Patel and A. P. Tiwari, "Reactivity and Delayed Neutron Precursors' Concentration Estimation Based on Recursive Nonlinear Dynamic Data Reconciliation Technique,", *IEEE Transactions on Nuclear Science*, vol. 66, no. 2, pp. 541-548, Feb. 2019 (I.F.=1.31, *TNS*)

Journals (Under Review)

Shrenik B. Patel, S. Mukhopadhyay, and A.P. Tiwari. "Fault Isolation Using Multi-Scale Principal Component Analysis for Industrial Processes " *Control engineering practice*

Conferences

1. Shrenik B. Patel, S. Mukhopadhya and A. Tiwar, "Observation of the nuclear reactor using wavelet-based extended Kalman filter, "2018 European Control Conference (ECC), Limassol, 2018, pp. 1-6. (Oral presentation)

2. Shrenik B. Patel, S. Mukhopadhya and A. Tiwari, "Feasibility study of Fast Output Sampling based state estimation technique,"International Conference for Convergence in Technology, Pune, Mar-2019.

Shrenik B. Patel
ENGG 01201404022

Contents

Recommendations of the Viva Voce Committee i

Statement by Author ii

Candidate's Declaration iii

List of Publications iv

Abstract v

List of Figures xi

List of Tables xv

Abbreviations xvi

Symbols xviii

1 Introduction 1

1.1 Multi-scale systems 5
1.2 Nuclear reactor: a multi-scale system 7
1.3 Motivation and objectives of thesis 10
1.4 Contribution of thesis 13
1.5 Outline of thesis 14

2 Literature Survey 16

2.1 Developments of time-frequency analysis techniques 16
2.2 Theory of state estimation: applications to nuclear reactors 18
2.3 Statistical process monitoring 22

3 Estimation of Reactivity and Delayed Neutron Precursors' Concentrations Using multi-scale EKF 27

3.1 Mathematical Model of Nuclear Reactor . . . 27
3.2 Estimation with EKF . . . 28
3.2.1 Representation in multiscale framework . . . 30
3.2.2 Estimation using multiscale EKF (MEKF) . . . 35
3.3 Simulation Results and Discussions . . . 38
3.3.1 Simulations using reference data set . . . 39
3.3.2 Simulations using plant data . . . 40
3.3.3 Validation of the results . . . 43
3.4 Summary . . . 45

4 Reactivity and Delayed Neutron Precursors' Concentration Estimation based on Recursive Nonlinear Dynamic Data Reconciliation Technique 59
4.1 Model Description . . . 60
4.1.1 Neutronic Model . . . 60
4.1.2 State Space Representation of Nonlinear Model . . . 61
4.2 RNDDR algorithm for the state estimation . . . 63
4.3 Validation of proposed RNDDR technique . . . 65
4.3.1 Numerical simulation . . . 66
4.3.2 Using experimental data set of FBTR . . . 71
4.4 Summary . . . 73

5 Estimation of fuel and the coolant temperatures of the nuclear reactor using stationary wavelet transform based multi-scale EKF 78
5.1 Simplified mathematical model of PHWR . . . 79
5.1.1 Reactor core and thermal hydraulic model . . . 79
5.1.2 Core Thermal Hydraulics . . . 80
5.1.3 State Space Representation of the System . . . 81
5.2 Brief introduction to Stationary wavelet transform . . . 83
5.3 State space modeling and estimation in multiscale framework . . . 84
5.3.1 Multiscale Extended Kalman Filtering . . . 86
5.4 Simulation Results . . . 86
5.5 Summary . . . 91

6 Multi-scale PCA for Fault Detection and Isolation 92
6.1 Fault isolation based on reconstruction . . . 93
6.2 Reliability analysis . . . 95
6.2.1 Autocorrelation-test:Ljung-Box Q statistic . . . 95
6.2.2 Variance of Reconstruction Error . . . 96
6.3 Multiscale Principal Component Analysis . . . 98
6.4 Simulation Results . . . 98
6.4.1 TE Process . . . 98

6.5 Summary 110

7 Conclusion and future scopre **111**
7.1 Conclusion 111
7.2 Future scope 113

A Wavelets **115**

B EKF Algorithm **122**

C PCA based fault detection and isolation **124**

Bibliography **129**

List of Figures

1.1 Schematic for process monitoring loop 3
1.2 Schematic of nuclear reactor (PHWR) 8

3.1 Block diagram representation for MEKF-2 32
3.2 Signals at analysis side of Fig. 3.1(a)Measured Signal (b) Approximated coefficient at level-1(c) Detailed coefficient at level-1 (d) Approximated coefficient at level-1 (e) Detailed coefficient at level-2 33
3.3 Signals at synthesis side of Fig. 3.1 (a)Estimated Signal (b) Approximated coefficient at level-1(c) Detailed coefficient at level-1 (d) Approximated coefficient at level-1 (e) Detailed coefficient at level-2 34
3.4 Reference reactivity variation 46
3.5 Simulated neutronic power 46
3.6 Reactivity 46
3.7 Neutrnoic Power 47
3.8 Concentration of a delayed neutron Precursor Group 1 47
3.9 Concentration of a delayed neutron Precursor Group 2 47
3.10 Concentration of a delayed neutron Precursor Group 3 48
3.11 Concentration of a delayed neutron Precursor Group 4 48
3.12 Concentration of a delayed neutron Precursor Group 5 48
3.13 Concentration of a delayed neutron Precursor Group 6 49
3.14 Measured neutronic Power of the research reactor 49
3.15 Variance of innovation process with tuning parameter q 49
3.16 Reactivity variation for power rise followed by fall 50
3.17 Estimated neutrnoic power variation for power rise followed by fall . 50
3.18 Concentration of a delayed neutron Precursor Group 1 for power rise followed by fall 50
3.19 Concentration of a delayed neutron Precursor Group 2 for power rise followed by fall 51
3.20 Concentration of a delayed neutron Precursor Group 3 for power rise followed by fall 51
3.21 Concentration of a delayed neutron Precursor Group 4 for power rise followed by fall 51

3.22 Concentration of a delayed neutron Precursor Group 5 for power rise followed by fall . . . 52
3.23 Concentration of a delayed neutron Precursor Group 6 for power rise followed by fall . . . 52
3.24 Measured neutronic power for shutdown followed by restart . . . 52
3.25 Reactivity variation for shutdown followed by restart . . . 53
3.26 Neutronic power variation for shutdown followed by restart . . . 53
3.27 Delayed neutron precursors' concentration of group 1 for shutdown followed by restart . . . 53
3.28 Delayed neutron precursors' concentration of group 2 for shutdown followed by restart . . . 54
3.29 Delayed neutron precursors' concentration of group 3 for shutdown followed by restart . . . 54
3.30 Delayed neutron precursors' concentration of group 4 for shutdown followed by restart . . . 54
3.31 Delayed neutron precursors' concentration of group 5 for shutdown followed by restart . . . 55
3.32 Delayed neutron precursors' concentration of group 6 for shutdown followed by restart . . . 55
3.33 comparison with reference reactivity for power rise followed by fall . 55
3.34 Error between reference and estimated reactivity for power rise followed by fall . . . 56
3.35 Comparison with reference reactivity for shutdown followed by restart 56
3.36 Error between reference and estimated reactivity for shutdown followed by restart . . . 56
3.37 Auto-correlation function for power rise followed by fall . . . 57
3.38 Auto-correlation function for shutdown followed by restart . . . 57
3.39 Error between normalized measured and estimated neutronic power 57
3.40 Error between normalized measured and estimated neutronic power for shutdown followed by restartup transient . . . 58

4.1 Assumed reactivity variation . . . 66
4.2 Neutronic power variation corresponding to reactivity variation shown in 4.1 . . . 67
4.3 Estimated power during shutdown transient with optimum **Q** and **R** 68
4.4 Estimated reactivity during shutdown transient with optimum **Q** and **R** . . . 68
4.5 Estimated neutronic power during shutdown transient with suboptimum **Q** and **R** . . . 68
4.6 Estimated reactivity during shutdown transient with suboptimum **Q** and **R** . . . 69
4.7 Estimated delayed neutron precursors' concentration of group 1 during shutdown transient with suboptimum **Q** and **R** . . . 69

4.8 Estimated delayed neutron precursors' concentration of group 2 during shutdown transient with suboptimum **Q** and **R** 69
4.9 Estimated delayed neutron precursors' concentration of group 3 during shutdown transient with suboptimum **Q** and **R** 70
4.10 Estimated delayed neutron precursors' concentration of group 4 during shutdown transient with suboptimum **Q** and **R** 70
4.11 Estimated delayed neutron precursors' concentration of group 5 during shutdown transient with suboptimum **Q** and **R** 70
4.12 Estimated delayed neutron precursors' concentration of group 6 during shutdown transient with suboptimum **Q** and **R** 71
4.13 Power variation from the FBTR during a rod drop experiment . . . 74
4.14 Estimated reactivity during a rod drop experiment 74
4.15 Estimated neutronic Power during a rod drop experiment 75
4.16 Estimated delayed neutron precursors' concentration of group 1 during a rod drop experiment 75
4.17 Estimated delayed neutron precursors' concentration of group 2 during a rod drop experiment 75
4.18 Estimated delayed neutron precursors' concentration of group 3 during a rod drop experiment 76
4.19 Estimated delayed neutron precursors' concentration of group 3 during a rod drop experiment 76
4.20 Estimated delayed neutron precursors' concentration of group 3 during a rod drop experiment 76
4.21 Estimated delayed neutron precursors' concentration of group 6 during a rod drop experiment 77

5.1 Block diagram representation for MEKF-2 87
5.2 Reactivity variation by regulating devices 87
5.3 Net reactivity variation 88
5.4 Simulated power 88
5.5 Simulated power with Noise 89
5.6 Estimated reactor Power 89
5.7 Estimated delayed neutron precursors' concentration 90
5.8 Estimated average coolant temperature variation 90
5.9 Estimated average fuel temperature variation 91

6.1 flowchart for multi-scale PCA 99
6.2 Flow-diagram of Tennessee Eastman process 101
6.3 LBQ statistic 103
6.4 Variance of reconstruction error 103
6.5 faulty variable for fault 5: x_{52} 104
6.6 Fault detection index for fault 5 with (a) PCA (b) MSPCA-3a . . . 105
6.7 Fault isolation index for fault 5 with (a) PCA (b) MSPCA-3a . . . 106

6.8 Faulty variables for fault 17 (a) x_9 (b) x_{21} (c) x_{51} 107
6.9 Combined detection index for fault 17 with (a) PCA (b) MSPCA-3a (c) MSPCA-1d 108
6.10 Fault isolation index for fault 17 with (a) PCA (b) MSPCA-3a (c) MSPCA-1d 109

A.1 Time Frequency tiling with STFT and CWT 118
A.2 Non-overlapping bands of ideal wavelet filter 119

C.1 A graphical illustration of the fault detection schemes 127

Chapter 7

Conclusion and future scopre

7.1 Conclusion

In this thesis, two different multi-scale EKF techniques for estimation of some important state variables of the nuclear reactor is presented. In the first technique, a nuclear reactor system is projected on the wavelet projection space by using the wavelet and scaling functions of the discrete wavelet transform as the basis. In the second technique, input and output signals of the nuclear reactor are resolved with the stationary wavelet transform functions. The proposed algorithms not only preserve the merits of the EKF technique but the use of wavelets provides an additional smoothing effect for the estimation. The multi-scale analysis allows online identification of the frequency components of the signals that help in modeling widely varying dynamic modes of a multi-scale reactor system. The proposed algorithm handles the system uncertainties and measurement noise using system covariance matrices which are tuned to have the optimal performance. Although the proposed algorithm is computationally expensive, it does not impose severe limitation with the use of modern high-speed digital computers. Performance of the proposed algorithm is assessed by carrying out estimation from the completely known dataset as well as plant dataset of one of the Indian research reactor. It is found that the proposed algorithm outperforms the standard EKF algorithm. However, it is also observed that the performance of multi-scale EKF algorithm is more susceptible with the sub-optimal tuning parameters than that

of the standard EKF. The proliferation of the proposed wavelet-based state estimation techniques can be done for sensor fault detection. Moreover, a constrained state estimation technique based on the Kalman filter framework, i.e., RNDDR technique is also proposed. The RNDDR has a simple form, which can induce an easy engineering implementation due to its recursive form. It also handles algebraic constraints and bounds on states and parameters. Constraints can arise due to feasibility considerations i.e., non-negativity of reactor power or delayed neutron precursors' concentration for nuclear reactor system. The results demonstrate that the RNDDR provides reliable and accurate reactivity estimations while there exist constraints on states, parameter uncertainties and noisy measurements. Thus, RNDDR will increase control flexibility and safety of nuclear reactors.

Moreover, in order to estimate the special variation of the reactor variables in a large nuclear reactor, the proper flux mapping technique may be integrated with the proposed state estimation algorithms. An important aspect of estimation techniques when considered for online application is its computational time, which should be carefully addressed, i.e., a platform for implementation should be selected so as to meet the computational time requirements.

In this thesis, a multi-scale PCA based MSPM technique is formulated. A new reconstruction based fault isolation technique in multi-scale PCA framework is presented. Although reconstruction based isolation technique eliminates the fault smearing effect, the reliability of the reconstruction procedure depends on the VRE. Results of statistical test for autocorrelation obtained with wavelet transformed coefficients indicate a significant reduction in auto-correlated features in wavelet projection space as compared with the same for the raw measurement space. Therefore, control limits for the PCA model derived over wavelet projection space could be more reliable than the same for the single scale PCA model. Moreover, VRE for the multi-scale PCA models is significantly reduced indicating reliable fault isolation. For the benchmark TE process, the detection and the isolation indices obtained with the multi-scale PCA models effectively monitor some of the faulty variables which are missed out by the single-scale PCA based indices. To find the root cause of the fault, the domain knowledge of the operator is required to do investigation based on the isolated faulty variables. The PCA models

derived in the projection space can give extra information about the frequency range of the fault which is potentially useful for the operator to investigate the cause of the fault.

7.2 Future scope

KFs are well known to have wide applications in sensor fault detection and diagnosis [118] besides for state estimation. As wavelet based multi-scale techniques provide a multi-scale hierarchical representation of the state variables, such a multi-scale representation could be more effective in detection and diagnosis of frequency dependent sensor faults. Therefore, the work reported in this thesis could be proliferated for such applications.

An important aspect of the proposed state estimation techniques when considered for an online applications is the computational time requirement, which should be carefully addressed. In this regards, a choice of the platform for implementation could also be important to meet the computational time requirements.

For state estimation of a nuclear reactors, a class of robust state estimation techniques such as sliding mode observers and H-∞ observers can be explored. Extension of these techniques in a multi-scale framework could perhaps be an interesting and relevant extension.

An important aspect for the multivariate process monitoring applications is the delay associated with the detection of fault. A popular statistical measure in this regard is the average run length [119] defined as average number of samples between the occurrence and the detection of a fault. The value of average run length depends on the selection of detection indices and the corresponding control limits. Different approaches for prior estimation of average run length have also been reported [120]. Reckon that the process monitoring technique reported in this thesis is based on the multiple PCA models derived at the certain wavelet scales. PCA model derived at a selected scale is more sensitive to the cross-correlated features over a certain frequency band and time duration matched to its scale than an approximated model at a single scale. Therefore, an average run length

for multi-scale PCA could be investigated for its potential for shorter duration as compared to a single-scale counterpart.

Finally, the proposed multivariate process monitoring technique belongs to the class of unsupervised fault diagnosis techniques. Although these techniques are useful for finding a root cause of the fault, it may take a considerable amount of time and expertise on part of plant engineers and operators. Provided that reliable reference datasets corresponding to the potential system faults are available, supervised fault diagnosis techniques may be investigated. In this context, theory of pattern classification has found some significant applications for assigning a fault-class for the onsite fault from the reference fault datasets.

Abstract

Modern nuclear, chemical or most other industrial plants are highly complex and operate with a large number of variables under closed loop control. Efficient monitoring and control can improve safety of the plant operations, minimize downtime, and optimize the plant economy. In most of the large scale processes, objectives of the process monitoring exercises are two-fold. The first objective is to estimate important process variables which are not measured directly. Inferring to the values of such variables could be very critical in various maintenance activities as well as in facilitating the state-feedback controller design. The objective of dedicated process controllers is to ensure satisfactory process operation by compensating the effects of potential process disturbances. While the controller can take care of various types of disturbances, there could still be process variations which controllers cannot handle adequately leading to the actuation of safety systems and shutdown thereby affecting the availability. Therefore, the second objective of the process monitoring system is to detect and manage such abnormal process variations. Surveillance of process anomalies is not only important to inform the operators and process engineers about the onsite events but also to assist them in making appropriate actions to recover the process. Moreover, most of such large scale industrial processes are characterized by a combination of phenomena that evolve with different rates or pace. Systems with such phenomena are referred to as 'multi-scale' systems. Monitoring and control of such systems could be more complicated than that of the single-scale systems. Therefore, it is desirable to develop process monitoring techniques which can account for the multi-scale nature of the system.

In this thesis, main objectives are formulation of (i) a multi-scale state estimation technique to estimate various states of complex nonlinear multi-scale system e.g., a nuclear reactor, and (ii) Multivariate Statistical Process Monitoring (MSPM) technique in multiscale framework. A nuclear reactor is a class of a multi-scale nonlinear system in which important variables like reactivity, delayed neutron precursors' concentration, fuel and coolant temperatures cannot be measured directly. Hence, these variables have to be estimated from neutron flux variations. Recently, few Kalman filtering (KF) based techniques were reported to serve the purpose.

While KF based techniques offer easy engineering implementation due to their recursive nature, one of the limitations is that they work at a single scale, i.e., they could not account for the multi-scale nature of the system. In past few decades, wavelets and filter bank theory have emerged as an effective way for multi-scale analysis of the signals and systems. Here, capability of the wavelets have been exploited to formulate two different state estimation formulations for the nuclear reactor systems. While the proposed formulations are based on and preserve the merits of the KF, use of wavelet filters enables multiscale decomposition of the state variables that in turn, effectively captures the multirate nature of the system. The efficacy of the proposed techniqe has been varified using the simulation results obtained from the simulated datasets as well as with the experimental datasets obtained from the research reactors. Moreover, another key limitation of KF and all of its variants, including the proposed wavelet based variants is that they cannot account for the constraints on state variables systematically, which may cause the instability of the filter. Therefore, a constrained state estimation technique based on the recursive nonlinear dynamic data reconciliation (RNDDR) technique is proposed in this thesis. The proposed technique systematically handles the physical constraints of the system and the effectiveness of the technique has been evaluated through the step test signal in the presence of measurement noise and experimental power variation data sets collected from one of the Indian reactors.

Another important aspect of the process monitoring techniques is to detect and manage abnormal events in the process. In this regards, the techniques based on first-principle process models have been extensively studied, however, their applications to large-scale industrial processes have been very limited as development of a sufficiently accurate process model is not always feasible or desirable. Therefore, techniques based on Principal Component Analysis (PCA) are well developed to analyze faults in the industrial processes. As process variables may contain the information of various events containing widely varying contributions over time and frequency, various approaches in wavelet based multi-scale PCA framework have also been reported to effectively detect faults in the process. However, development of multi-scale techniques has taken place at a slower pace compared to that of the single scale techniques. Consequently, some of the important aspects of

the process monitoring have not gained enough attention in multi-scale framework based techniques. After detection of the fault, isolation of the faulty variable is very important in finding the root cause of the onsite event. In this thesis, a fault isolation technique based on the variable reconstruction approach in the multi-scale PCA framework is presented. The process data containing the measured variables are transformed into wavelet projection space using the discrete wavelet transform (DWT), and multi-scale PCA models are derived using the transformed data. It is shown that multi-scale PCA models comply with the assumptions of PCA based multivariate statistical process monitoring (MSPM) because wavelet transformed data are significantly less autocorrelated than the measured data. The reliability of the proposed multi-scale PCA technique is assessed by the autocorrelation test and variance of the reconstruction error. The efficacy of the proposed technique is assessed with the simulation results obtained with the numerical dataset as well as with the dataset of the benchmark Tennessee Eastman process. The proposed technique overcomes some limitations of the standard PCA based technique and effectively detects and isolates various process faults.

Chapter 1

Introduction

For chemical processes, nuclear reactors, and any other large scale industrial processes, a consistent and safe operation is of utmost importance. This is due to increasingly stringent environmental regulation, production specifications, economic and operational constraints. Consequently, the process operations that were acceptable at one time are no longer adequate. Therefore, there is an upward interest in research and development of more reliable plant monitoring systems. In order to meet the higher standards, the modern process monitoring and control systems heavily rely on quality data. In the context of the data acquisition, optimum quality and quantity of the data are important to ensure the desired performance. Employing a large number of sensors to directly measure system variables may not be desirable as it may adversely affect the system reliability. In some cases, direct measurement of some system variables are not even possible due to several

reasons including unavailability of the sensors, feasibility constraints, and plant economics. Considering all these factors, an optimum selection for the number of sensors is important in minimizing the failure rates and improving system reliability. Therefore, for the estimation of the state variables from the measured variables, the state estimation theory has found a prominent space. As many standard controller design techniques are based on the state feedback, the state estimation is inevitably critical in facilitating the controllers. However, the application of the state estimation is not just limited to this, it may play an important role in many applications like data fusion, calibration of the sensors, trajectory estimation and some maintenance routines.

While dedicated controllers can compensate for the effect of various disturbances, there are some disturbances which cannot be handled by the controllers adequately. Such disturbances are defined as 'faults'. Faults may appear due to various causes, i.e., external, internal or combination of both. The external causes may include environmental effects and violation of the input ratings. The internal causes may include wear and tear, miscalibration, leakages, ageing and poor maintenance, etc. The occurrence of the faults may lead to the reduction in the safety margins, off-specification production, reduction of the component life. Usually, the presence of the fault can be detected by its reflections on the signals associated with the system. If faults are not timely detected or remain undiagnosed even after detection, they actuate the safety system and a plant shutdown leading to the loss of availability. Moreover, poor plant monitoring and control may on one hand affect the plant economy, while on the other hand weigh on the risk of safety system failures. For the safety-critical systems such as nuclear reactors and some chemical

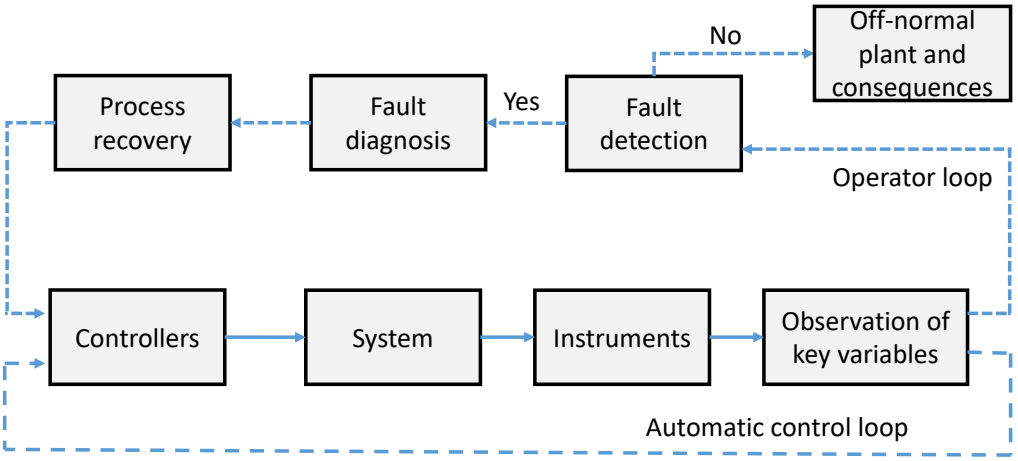

FIGURE 1.1: Schematic for process monitoring loop

processes, safety breaches can be disastrous. The Chernobyl nuclear accident[2], Three Mile Island accident[3], and Bhopal gas tragedy [4] are few examples of such systems. Therefore, faults must be detected and diagnosed before they lead to serious consequences.

In the past few decades, there is a huge push in developing plant automation systems to ensure consistent and safe operation. A simplified schematic of the monitoring and control loop of a large scale industrial process can be devised as shown in Fig 1.1. As depicted, the plants are generally operated into two loops, i.e., an automatic control loop, and an operator loop. In the data acquisition step, important system variables are measured and scaled into a usable digital form. The next step is to estimate the key process variables. This procedure includes the estimation of the state variables of the various sub-systems which may be required for the state feedback controller design and other important variables which may be required for the fault detection and diagnosis procedure. The FDD routine consists of three procedures namely, fault detection, fault diagnosis, and process recovery. The fault detection procedure determines the occurrence of the fault.

Early detection may give invaluable alarm signal on the emerging anomalies, with appropriate actions taken to avoid serious process upsets. If fault goes undetected, it results in the abnormal process behaviour and consequently triggers the safety system which may lead to a plant shutdown. Upon detection of a fault, the fault diagnosis is a procedure to determine a cause of the out-of-control status. More precisely, it is a procedure to find out fault-relevant information such as type, location, magnitude, and time of the fault. This step is essential in determining counteraction for the elimination of the fault. The final step of the loop is process recovery, in which required actions are taken to eliminate the fault and establish normalcy in the process.

The goal of the state estimation is to render accurate estimate the state variables during all the operating conditions. In this context, various performance measures such as robustness, stability, transient and steady-state performance, etc are assessed to determine the efficacy of the state estimation technique. As there is no standard technique that can meet all the performance requirements adequately, the selection of the particular technique could be highly subjective to the problem under investigation. Whereas the goal of process monitoring is to develop measure that are optimally sensitive and robust to all out-of-control errors and disturbances. The process monitoring measures are mainly based on three approaches; namely, measures based on the physical model or first principle model of the process; [5]; data-driven measures based on the empirical models or second principle models developed by using the historical process data[6]; and measures based on hybrid models or semi-empirical models with the prior process knowledge [7]. The selection of the suitable process monitoring technique is highly subjective

to the target problem. If a reliable physical model is feasible to develop, the first principle model based approaches could be preferred for their extrapolation ability. For complex industrial processes, development and calibration of a process model based on the first principle is a difficult task and the model development exercise may result in a too complicated model to be useful. Therefore, data-driven MSPM techniques based on PCA and Partial Least Squares (PLS) are extensively studied and successfully employed for monitoring industrial processes.

In this work, state estimation and multivariate process monitoring problem for a specific class of complex nonlinear systems, i.e., multi-scale systems are investigated. A brief overview of the multi-scale systems followed by the objectives and contribution of this thesis is described subsequently.

1.1 Multi-scale systems

Multi-scale systems are the class of systems in which variables evolve with the widely varying rates in the time as well as in the frequency. The variables of such systems can possess multi-scale phenomenon due to several reasons. First due to the difference in the sampling intervals of the different sensors, i.e., due to the multi-rate sampling scheme [8]. Secondly, in the process industry, sampled variables possess the contributions from the several process events with different localization in time and frequency [9].

Process monitoring and control of multi-scale system could be more complicated than that of the single scale systems [10]. It is well known that the application of the standard control techniques to multi-scale systems may lead to numerical

ill-conditioning, closed-loop instability, etc [11]. To overcome these drawbacks, the multi-scale systems can be represented as a combination of slow and fast modes. By performing such a decomposition, the controller can be designed based on the separate design criteria for each mode. In this context of multi-scale systems, the singular perturbation theory has found a prominent place [11]. Moreover, with the development of techniques based on time-frequency analysis, some powerful tools that can effectively capture the multi-scale nature of systems by exploiting time-frequency features of the system have found strong applications [12][13]. In this work, however, analysis of the multi-scale systems with the technique with wavelets is investigated because of the amenability of wavelets to model time-frequency phenomena.

In the context of the measured data with the contributions localized in time and frequency simultaneously, it is not efficient to represent the data in term of the basis functions defined only at a single scale. Typically, low frequency features of the measured data contain the deterministic variation due to process dynamics and high frequency features of the data contain stochastic variation due to disturbances, noise or faults. In order to separate deterministic process variations from the data, an obvious technique is to employ a low-pass filter. However, any filtering scheme is inherent trade-off between the extent of noise removal and the quality of the retained features. In terms of analyzing the time and frequency dependant features of the data, raw measurements give a good picture in the time domain but completely miss out the information about frequency contents. Similarly, the Fourier transform gives an excellent picture about frequency contents at the cost of losing information about variations in time. Moreover, Fourier

transform works with the assumption of stationarity, i.e, it assumes that the frequency content does not vary with time. However, for most of the real-time processes, measured data are non-stationary. For example, consider the data of a biomedical system, typically the data containing ECG signals are analyzed by considering different signal-segments containing fast and slow variations. Another good example of the multi-scale systems could be the traffic on a multi-lane highway where the movement of the pedestrians, bikes and cars have different scales. Therefore for the multi-scale signals, various techniques like Short Time Fourier Transform, Wigner-Ville Distribution, Hilbert-Huang Transform, Wavelet Transform have been explored to account for the time and frequency-dependent features simultaneously. Among all these techniques, the theory of wavelets has emerged as one of the most powerful tools for analysis of non-stationary signals. It analyzes signals over various frequency ranges or scales providing multi-scale hierarchical representation of the signals.

1.2 Nuclear reactor: a multi-scale system

A nuclear reactor is based on the concepts of a sustained chain of nuclear fission. In nuclear fission, a heavy nucleus like Uranium-235 (^{235}U) is annihilated by the neutron and as a result, the heavy nucleus is fragmented into two or more smaller nuclei. This process also renders two important phenomena namely, (1) a significant amount of kinetic energy of the fission fragments is converted into the heat and, (2) a few neutrons, typically 2 to 3 are generated. These neutrons further cause fission of the heavy nucleus which induces the chain of fission reactions. Soon after the discovery of this phenomenon in 1939, it was perceived as a promising

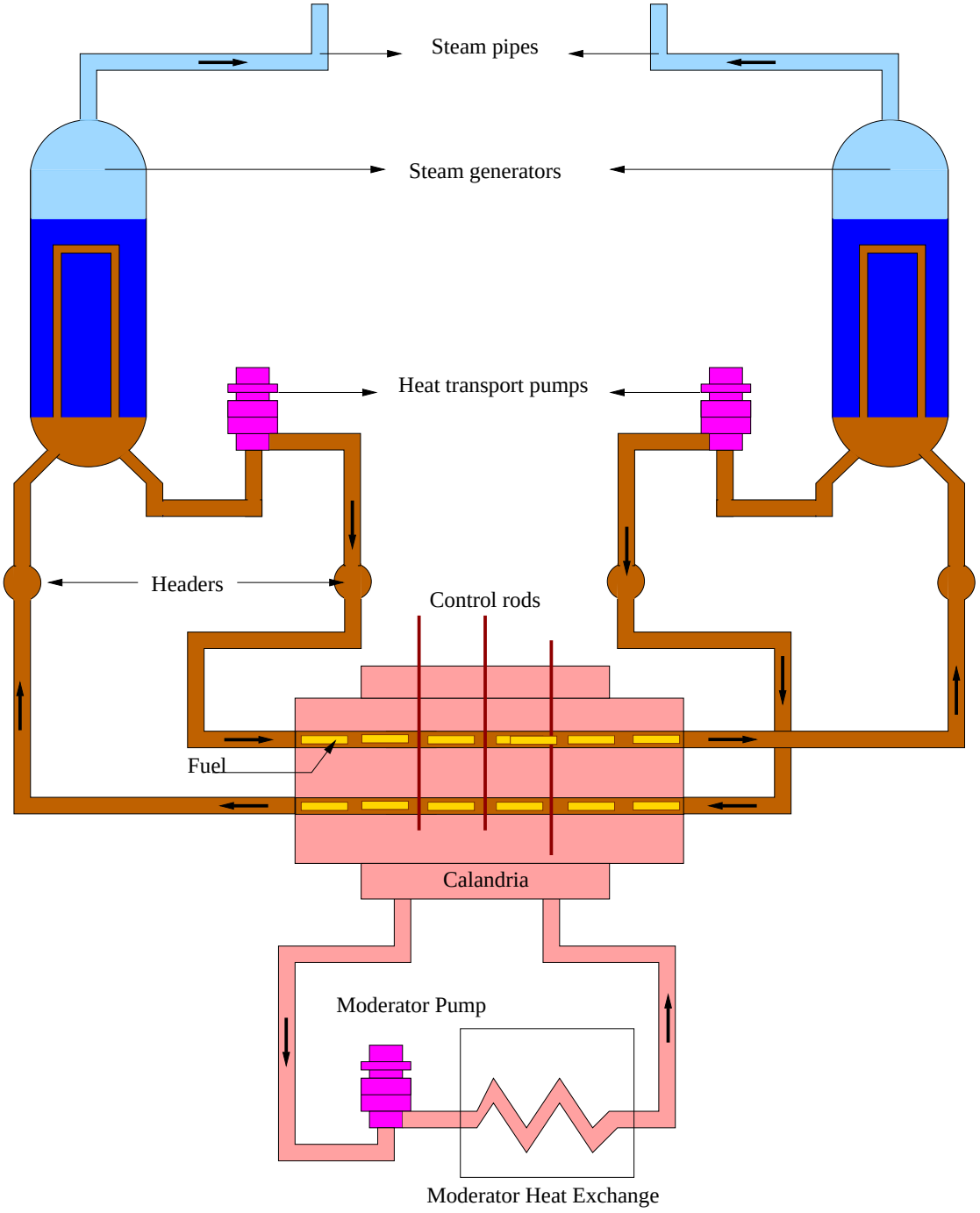

FIGURE 1.2: Schematic of nuclear reactor (PHWR)

new source of the energy. The first nuclear reactor was realized by Enrico Fermi in 1942. However, the serious developments of the modern nuclear reactors began in the 50s and many complex nuclear reactors have been built subsequently. The detailed discussion on the nuclear reactors and related concepts can be found in [14].

A schematic of a Pressurized Heavy Water Reactor (PHWR), a type of nuclear reactor is depicted in Fig. 1.2. The pallets generally containing natural Uranium are filled in the tubes to form a reactor fuel. The key to ensure a sustained nuclear chain reaction in the rector is to maintain an adequate density of neutrons in the reactor core. Considering a fission multiplication factor k denoting an average number of neutrons from one nuclear fission causing another fission, criticality of the reactor is determined. An important parameter to characterize criticality is reactivity which is defined as $\rho = \frac{k-1}{k}$. The reactivity is maintained to zero-level unless it is required to increase or decrease the power level. The reactors geometry and control systems are designed to influence the reactivity in order to ensure a safe and consistent operation. For the nuclear reactors using low enriched uranium or natural uranium, neutron moderators are used by which released neutrons are slowed down to facilitate the fission process. The control rods made with the neutron-absorbing materials such as cadmium are inserted or withdrawn from the core to control the reactivity or to halt the operation. The high-pressure heavy water in the circulating loop serves as primary coolant and removes the heat from the reactor. The heat is transferred to the secondary loop and steam thus generated is sent to the turbine unit.

Neutron density in a nuclear reactor is usually characterized by the point kinetics model which assumes that neutron distribution in space is constant. Such a model provides an adequate degree of accuracy and it has been used for observers or controller design for small reactors. For large nuclear reactors, space-time kinetic models have also been developed to improve the degree of accuracy. Moreover,

the nuclear reactors possess a multi-scale phenomenon as the variation of the system variables occurs at significantly different rates. For example, delayed neutron precursors emit neutrons with different decay rate i.e., the pace of neutron getting liberated is uniquely different for each group. Among all 6 groups usually considered, the first group has the decay constant with the order of $10^{-2}s^{-1}$ (1.2×10^{-2} for ^{235}U), while the sixth group has the same of the order of s^{-1} ($3.01s^{-1}$ for ^{235}U). As a consequence of such phenomena, it is well known that identification, monitoring and control using single-scale approaches are inefficient, and such attempts may lead to numerical ill-conditioning[11]. Therefore, over the time, different methods exploiting two-time scale and three-time scale properties of the system have been investigated [15][16]. Moreover, wavelet-based techniques have also found some strong applications in nuclear engineering for noise removal[17], transient detection[18], system identification and control[19].

1.3 Motivation and objectives of thesis

Traditional approaches for the state estimation in the nuclear reactors work on the assumption that state variables associated with the system are deterministic[20]. However, in reality, due to the presence of inevitable measurement noise and fundamental stochastic nature of the fission process, this assumption is unrealistic. Therefore, state estimation techniques which can work in the stochastic framework, e.g., Kalman filtering have been developed. However, as these techniques work at a single scale, they could not account for the multi-scale nature of the system. In the past few decades, wavelets and filter bank theory have emerged as an effective way for multi-scale analysis of the signals and systems. Therefore, for

a class of multi-scale systems, a state estimation technique that performs simultaneous decomposition and estimation of the state variables could be expected to outperform the standard techniques [21].

One of the primary objectives of the process monitoring systems is to detect and manage abnormal events in the process. In this context, statistical techniques based on PCA have found some strong applications. For the multi-scale systems, multi-scale PCS based techniques through wavelet-based multi-scale framework have been reported to be superior to their single-scale counterparts [22]. However, such techniques possess few limitations. First, the focus of these techniques is limited to fault-detection only. Consequently, they do not assist plant operators and maintenance engineer to identify the root cause of the fault. Although the problem of effective isolation of the faulty variables within a single scale PCA framework has gained significant attention, extrapolation of the same in the multi-scale PCA framework has not gained enough attention. Another limitation is that the monitoring indices implicitly assume that the measured variables are time-independent (uncorrelated). However, due to the process dynamics and structured variations, this assumption is unrealistic in most of the cases [23]. Although it is well known that the discrete wavelet transform (DWT) possess the capability to de-correlate various signals, the effect of this property on the reliability of the FDI techniques has not been reported yet.

Following this, the main objectives of this thesis are listed in the following:

- Formulate a multi-scale model structure by projecting the states of nonlinear autonomous system on the family of wavelets and scaling and functions as

a basis. Implement Extended Kalman Filtering (EKF) algorithm on the system model in the wavelet projection space.

- Evaluate the performance of the proposed multi-scale EKF algorithm by comparing the same with the standard EKF algorithm using the simulation results obtained with various datasets.

- Formulate the stationary wavelet transform (SWT) based model structure that permits working with the forced nonlinear systems.

- Formulate a constrained state estimator based on the recursive non-linear dynamic data reconciliation (RNDDR) technique for estimation of the reactivity and delayed neutron precursors' concentration.

- Assess the effectiveness of the proposed RNDDR technique by the simulation results obtained for different transients.

- Propose a new multi-scale PCA based MSPM technique for effective fault-detection and isolation of variables associated with the onsite fault.

- Validate proposed multi-scale PCA method with the simulation results obtained for a numerical problem as well as for the benchmark Tennessee Eastman process data.

1.4 Contribution of thesis

Contributions of the thesis are as follows:

- A multi-scale model structure is formulated by projecting system states on Haar scaling and wavelet functions as the basis. EKF algorithm is formulated on the system model in the projection space and the same is applied to the point kinetics model of the nuclear reactor. The computational complexity of the proposed algorithm is compared with that of the single-scale counterpart. The estimation has been carried out using reactor power as the only input. In order to justify the effectiveness of the proposed method, simulation results are shown for completely known power variation dataset and experimental power variation data-sets collected from one of the Indian research reactors.

- The thermal-hydraulic analysis is one of the critical design aspects of the nuclear reactor. While nuclear aspects of the design allow the reactor to be operated at any power level, the core temperature distribution and heat transfer rates impose a limitation on the achievable thermal power. A stationary wavelet transform (SWT) based multi-scale EKF algorithm is formulated for the state estimation of a forced nonlinear system and applied on the thermal hydraulic model of a nuclear reactor. The input and output sequence of the system is analyzed to derive the state-space model in the wavelet projection space. The efficacy of the proposed technique is assessed by the simulation results obtained by the simulated data by the thermal-hydraulic model of the PHWR.

- The standard EKF technique is prone to yield unreliable estimates due to violation of physical constraints during a certain process operation such as shutdown. A Recursive nonlinear dynamic data reconciliation (RNDDR) based state estimation technique is proposed. The proposed technique accounts for the physical constraints on the reactor power and delayed neutron precursors' concentrations and retains benefits of the recursive implementation. The feasibility of the RNDDR method has been verified, through step test signal in the presence of measurement noise and experimental power variation data sets collected from a research reactor.

- A fault isolation technique based on the variable reconstruction approach is proposed in the multi-scale PCA framework. The process data containing the measured variables are transformed into wavelet projection space using the discrete wavelet transform (DWT), and multi-scale PCA models are derived using the transformed data. The reliability of the proposed multi-scale PCA technique is assessed by the autocorrelation test and variance of the reconstruction error. The efficacy of the proposed technique is assessed with the simulation results obtained with the numerical dataset as well as with the dataset of the benchmark Tennessee Eastman process.

1.5 Outline of thesis

The rest of the thesis is organized as follows. In Chapter 2, a literature review relevant to the topics of time-frequency analysis, state estimation of the nuclear reactor, and data-driven process monitoring techniques is presented. In Chapter 3, a formulation of a multiscale EKF followed by its application for estimation of

reactivity and delayed neutron precursors' concentration for various scenarios is presented. In Chapter 4, the formulation of an RNDDR based constrained state estimation technique on the application of reactivity and delayed neutron precursors' concentration is presented. Chapter 5 describes the formulation of stationary wavelet transform based EKF technique. Also, its application for estimation of fuel and coolant temperatures of the nuclear reactor is presented. In Chapter 6, a formulation of fault detection and isolation technique for MSPM in a multi-scale PCA framework is presented. A new reconstruction based fault isolation procedure is presented and the reliability of the proposed MSPM technique is assessed by suitable statistical tests. Concluding remarks and the scope for the future work is described in Chapter 7. Appendices discuss a brief overview of the wavelets, EKF algorithm, and PCA based MSPM.

Chapter 2

Literature Survey

In this chapter, a literature survey on topics relevant to the state estimation and process monitoring considered in this thesis is presented. Literature survey includes a brief overview of the developments of time-frequency analysis techniques, the theory of state estimation: applications to the nuclear reactors, and statistical process monitoring techniques. However, the survey is not intended to be exhaustive.

2.1 Developments of time-frequency analysis techniques

The problem of analyzing non-stationary multi-scale signals by exploiting features over different time and frequency has gained significant attention from researchers. The efforts made in this context lead to the development of several time-frequency analysis techniques [12]. However, the basic idea of all the time-frequency analysis techniques is to use the basis functions which analyze the signals over a certain time and frequency range. Therefore, a choice of basis functions or transforms is made to meet the requirement of the time-frequency localization characteristics of the target problem. However, a fundamental result in this context is that the ability of any basis function for simultaneous localization in time and frequency is limited by 'duration-bandwidth principle'.

Short-Time Fourier Transform (STFT)[24] is one of the key historical developments. Although STFT offered a significant improvement over the traditional approaches, its applicability has been limited due to concerns over its practical usability. Therefore, efforts on devising the alternate techniques lead to the developments on the theory of wavelets. A detailed review on the historical developments can be found in [12].

The theory of wavelets has been extensively studied by several research communities in the field of mathematics, physics and engineering. One of the earliest and popular contributions was offered by Haar in 1910 [25]. A method was proposed to represent a smooth function as a linear combination of discontinuous functions, an idea dual of the Fourier analysis. However, at that time, a term wavelet was unknown. The concepts of the wavelets in the existing theoretical form were pioneered by Grossman and Morlet [26]. The wavelet transform in its original form yields a redundant or overlapping representation in a time-frequency plane. It was Meyer's contribution which opened a direction towards orthogonal wavelet transform having some attractive properties such as minimal representation, compact support, etc. A significant momentum in the application of wavelets was gained with the discovery of connections between the wavelets and multi-rate filter banks formalized by Mallat [27] and conditions on the perfect reconstruction by Vetterli [28].

The literature on the time-frequency analysis techniques based on wavelets is very rich. Various variants of the wavelet transform alongwith their implementations, each customized to meet application-specific requirements have been reported [29][30]. However, all such variants are essentially modifications of the basic wavelet transform, i.e., Continuous Wavelet Transform (CWT)[27]. Moreover, some excellent textbooks with in-depth descriptions on the foundations and applications of the wavelets are also available [31–34].

The wavelets are well known to render some key properties like compact support, wavelet shrinkage, multi-resolution approximations, decorrelation in the wavelet projection space etc. Due to these properties wavelets have found a prominent

space in some of the engineering applications such as modelling, control, system identification, filtering, and process monitoring.

2.2 Theory of state estimation: applications to nuclear reactors

The state of a dynamic system is defined as a set of memory storing elements or variables, which completely characterize the system at any given instant of time. The evolution of a system can be predicted by knowing the system state and excitations. Assuming that the system is observable, traditional state estimation techniques were developed to estimate the state variables using system model and input-output sequences [35]. However, these techniques assume system variables to be deterministic. But in reality, measurement signals are inevitably corrupted with noise arising from detectors, communication channels and over and above due to fundamental stochastic nature of the process dynamics. The classical techniques do not address the stochastic nature of the system and measurements.

The foundation of the modern state estimation techniques was established in early 1800 by the theory of least squares estimation proposed by Gauss. The mathematical framework for the modern state estimation theory was originated with the work of Wiener in the late 1940s. However, it was the contribution offered by R.E. Kalman in 1960 [36], after which research and application of the modern state estimation theory gained significant momentum. This contribution is considered as one of the greatest discoveries of the 20th century. The milestone contribution is popularly known as the Kalman filter. The Kalman filter in its original form was devised for the linear systems, however, different variants of the Kalman filter each customized to meet application requirements have been devised.

The Kalman filter is a recursive data processing algorithm for the linear dynamical systems, optimal under the assumption that the system uncertainties and measurement noise are white and Gaussian [37]. More precisely, the Kalman filter optimally estimates the current states by using the knowledge about the system and measurement device dynamics alongwith the statistical description of errors

associated with them. It has been widely used for the various industrial applications such as inertial navigation[38], spacecraft tracking [39], economic time series estimation [40] and so on. For the real-time complex systems, recursive nature of the algorithm has vital importance for the practical implementation. Moreover, for the class of non-linear systems, the Kalman filter is employed with linearization procedure at the filtering steps. The Kalman filter so derived is popularly known as extended Kalman filter (EKF).

There are various derivations of the Kalman filter through different perspectives. Few derivations along with the required mathematical preliminaries can be found in [41–44]. Instead of reiterating these derivations, the basic algorithm is described in the Appendix section.

Nuclear reactors are complex non-linear systems with coexisting multi-time scale phenomena. System variables like reactivity, delayed neutron precursors' concentration, temperatures of the fuel and the coolant inside the reactor core cannot be measured directly. Reactivity in the nuclear reactor is a very important variable which indicates the status of the reactor core. Online measurement of reactivity is very important for calibration of control devices, monitoring shutdown margins, quantification of the worth of fuel bundles, etc. [45], [46]. Other important variables are concentrations of the delayed neutron precursors which emit delayed neutrons that in turn, play an important role in reactor control [47].

Due to lack of suitable sensors, variables like reactivity and delayed neutron precursors' concentrations cannot be measured directly [48]. Consequently, these variables need to be estimated from neutron flux/power measurements using an appropriate estimation algorithm [49]. Traditionally, Inverse Point Kinetics (IPK) like algorithms were used to serve the purpose [50]. However, these techniques assume system variables to be deterministic. But in reality, measurement signals are inevitably corrupted with noise arising from detectors, communication channels and over and above due to fundamental stochastic nature of the fission process itself. The classical techniques do not address the stochastic behaviour of reactor kinetics and measurement process. Commonly used method to eliminate noise is

to employ a low pass filter but it may as well remove some of the information-rich frequency components generated by the reactor system.

Kalman filter (KF) is one of the promising modern optimal state estimation algorithms that permits working in a stochastic framework under the assumption that process uncertainties and measurement noise have Gaussian distribution [51]. Many attempts have been made for the observer design problem of the nuclear reactor using the Kalman filter. Racz [52] proposed Kalman filtering method for reactivity estimation for small changes in the reactivity. Zhe [53] reported the application of robust Kalman filter to estimate various state variables of a reactor such as neutronic flux, concentrations of delayed neuron precursors, average fuel temperature, coolant temperature inside the reactor and coolant temperature entering the reactor core. T.U. Bhatt et. al. [20] reported Extended Kalman Filtering (EKF) technique for online reactivity estimation of the nuclear reactor and justified merits of the EKF technique over conventional IPK like technique. Silva et. al. [54] demonstrated simulation results for reactivity estimation during reactivity initiated accidents using EKF technique. Shimazu and Rooijen [55] reported qualitative performance comparison between IPK and EKF techniques. Peng et. al. [56] demonstrated comparative study of two EKF techniques using different Jacobian structures. In [57], authors reported EKF technique to estimate the poisons' concentrations in the PWR nuclear reactors based on the reactor power measurement. They have carried out a comparative study of the results obtained from the continuous-time EKF with that from KF and Luenberger observer. The KF based state estimation techniques are perceived as a very promising candidate for state estimation of the nuclear reactors as they offer easy engineering implementation due to their recursive nature. However, ignorance of the process features such as multi-scale nature of the system and physical constraints on the estimated state variables may raise concern over their performance potential.

An important feature of the Kalman filter algorithm is that almost all the available information about the system can be used to improve estimator's performance. In this thesis, the motivation is to formulate a reliable Kalman filter based state estimation technique for the nuclear reactor. It stems from the fact that a nuclear reactor is a nonlinear multi-scale and there exists a physical limitation on the

state variables like reactor power and delayed neutron precursors' concentration. In order to exploit multi-scale nature into the Kalman filtering algorithm, one of the interesting formulations was proposed by Hong et al.[21]. They reported an interesting way for simultaneous decomposition and estimation for a class of autonomous systems. Inspired by this work, a multi-scale EKF algorithm for a multivariate nonlinear system is formulated and its feasibility to estimate variables of a nuclear reactor is investigated by the authors in [58] which is described in Chapter 3. However, the applicability of multi-scale EKF algorithms reported in [58] and [21] is limited to a class of autonomous system. Nounou et al. [59] reported stationary wavelet-based multi-scale Kalman filter for the class of the nonlinear systems modelled in a fuzzy framework. The input and output signals are decomposed upto a certain number of scales before deriving the state-space model of the system in the projection space using only approximation coefficients. However, the detail coefficients which may contain significant information were completely discarded. Motivated from this, a stationary wavelet transform based multi-scale EKF algorithm has been formulated for the state estimation from the forced nonlinear system and applied on the nuclear reactor system.

Another limitation of KF based algorithms is that they cannot handle physical constraints on the estimated state variables, consequently, the estimator may render infeasible estimates which may results in instability of the filter [60]. One of the most popular constrained state estimation techniques is the moving horizon estimation (MHE) [61], which is computationally demanding and raises real-time implementation concerns due to its non-recursive form. Various methods for the constrained state estimation using KF are surveyed by Simon [62]. In order to perform the state estimation with the inequality constraints, the estimated states may be projected to the constraint surface by formulating a quadratic programming problem [63]. One of the promising candidates to solve the problem is Recursive nonlinear dynamic data reconciliation (RNDDR) technique [64]. It is essentially MHE with horizon size one. The RNDDR technique can account for the constraints on the state variables and retains the computational advantages due to its recursive form for implementation. In this technique, for each time instant, the prediction step is followed by an update step similar to EKF. In RNDDR,

the predicted state variables and error covariance matrix are obtained as in EKF, while the updated state variables are obtained as the solution of a constrained optimization problem. RNDDR is identical to EKF if there are no bounds on variables or algebraic constraints. Hence, RNDDR can be viewed as one form of a constrained EKF, which is easy for practical implementation.

2.3 Statistical process monitoring

Data-driven statistical process monitoring techniques have been very popular in analyzing and managing abnormal process scenarios. Numerous methods have been developed with different objectives and choice of statistical parameters to characterize the process anomalies. The suitability of the monitoring technique can be subjective to the problem under investigation and characteristics of the associated data. Detailed review on various data-driven process monitoring techniques can be found in [1][65].

Traditionally, monitoring methods based on 'limit sensing' were very popular [66][67]. These univariate techniques raise an alarm signal when process variables violate predefined threshold limits. These methods, however, do not account for the relationship among the variables. In most of the industrial processes, often the measured variables tend to have a correlation between them. This is because a large number of sensors are generally employed and measured variables are likely to reflect the process equilibrium, environmental effects, controller actions for reference tracking, conservation laws such as energy and material balances, etc. Therefore, a univariate statistical process monitoring technique that ignores the correlation structures, may raise alarm signals for so many variables. Consequently, they may misguide the process operators and maintenance engineers [68].

The necessity of accounting the spatial correlation structure among the measured variables lead to the development of the PCA based monitoring techniques. The concepts of PCA as a linear dimensionality reduction technique were first introduced by Karl Pearson [69]. The theoretical framework for the use of PCA for the

process monitoring applications was offered by Wise [70] and Wold [71]. Comprehensive reviews regarding the data-driven process monitoring techniques can be found in [6] and [72].

The historic process data containing measured variables under the normal operating condition are used to develop the PCA model[73][74]. The model thus obtained transforms the measurement space into two subspaces, i.e., the principal component space (PCS) and the residual space (RS). When a new measurement is obtained, the PCA model projects it on PCS and RS. Subsequently, to detect the fault, abnormal projections on PCS and RS are analyzed by computing Hotelling T-squared index and square prediction error (SPE), also called or Q index [75] [76]. Yue and Qin [77] proposed a single detection index (φ index) that effectively combines the T-squared and Q indices to observe the abnormal projections on PCS and RS simultaneously. The fault in the process is suspected if any of the detection indices violates the predefined control limits derived by the PCA model. In the past few decades modified PCA based FDI techniques such as dynamic PCA[78], distributed PCA [79], kernel PCA[80], sparse PCA[81], etc. have also been developed. The dynamic PCA is suitable for highly correlated data where the data matrix is formed by stalking lagged measurements to reduce the autocorrelation in the data. The kernel PCA is suitable when the measured variables possess highly non-linear relationship between them. The space PCA is used while accounting all the measured variables is not desirable, here, the PCA vectors are derived by solving an optimization problem by imposing the scarcity constraints in PCA vectors. However, in all these variants the basic idea is to remain the same, i.e., to exploit the cross-correlation of the data for more meaningful interpretation.

In all these techniques, the measured variables are interpreted at a single scale. However, the variables for most of the industrial processes may have contribution due to various scenarios like abrupt parameter variations, measurement noise, sensor failures, operator-induced events etc. Every event may have its contribution over time and frequency. Consequently, PCA based MSPM techniques employed at a single scale cannot account for the multi-scale variations of the system variables. The wavelet transform is one of the most powerful tools to analyzes multi-scale

signals. It analyzes signals over various frequency ranges or scales providing multi-scale hierarchical representation of the signals. Various fault detection techniques with wavelet-based multi-scale PCA framework are devised to account for multi-scale features of the measured variables. Bakshi et al. [22] first devised a wavelet-based multi-scale PCA technique for fault detection. Discrete wavelet transform (DWT) was employed to assess correlation within the variables and PCA was employed to assess correlation across the variables. Misra et al. [82] reported a multi-scale PCA technique for various sensor fault scenarios for the industrial processes and demonstrated the efficacy of multi-scale PCA over single-scale PCA. Zhang et al. [83] reported that the PCA model developed over wavelet transformed data comply with the statistical assumptions of the PCA based fault detection techniques. Nounou et al. [84] reported a fault detection technique based on the Generalized Likelihood Ratio Test (GLRT) in multi-scale PCA framework applied on the benchmark Tennessee Eastman (TE) process.

Although these techniques claim significant improvement over the single-scale PCA, they possess the following limitations.

- Monitoring indices implicitly assume that the measured variables are not interdependent (uncorrelated). However, due to the process dynamics and structured variations, this assumption is unrealistic in most of the cases. Although it is well known that the discrete wavelet transform (DWT) possesses the capability to decorrelate various signals, the effects of this property on the efficacy of the fault detection and isolation procedures have not been studied.

- In order to identify the root cause of the on-site event, isolation of the faulty variables is critically important. Although the problem of effective isolation of the faulty variables within a single scale PCA framework has gained significant attention and some promising isolation techniques that isolate the faulty variables without fault-smearing effect have also been reported, extrapolation of same in the multi-scale PCA framework has gained very limited attention.

The effect of autocorrelation on monitoring indices of PCA based MSPM technique was discussed by many authors [23, 85–87]. In order to deal with the autocorrelated data, one of the most popular ways is to modify the raw data before employing PCA. In this regards, dynamic PCA based techniques have found a prominent place in which, PCA model is built with the data containing lagged measurements. However, such approaches also demand careful selection of the number of lags and significantly increases the model complexity. Moreover, monitoring indices based on dynamic PCA may still yield autocorrelated PCS [88].

In the past few years, various fault isolation techniques have been studied extensively [89–92]. Among these techniques, contribution analysis based techniques which evaluate the contribution of each variable to the fault detection index are most popular. A comprehensive review of the fault isolation techniques based on the contribution analysis can be found in [93][94]. However, these techniques are well known to possess some common drawbacks, such as misdiagnosis due to *fault smearing*, i.e., the contribution statistics calculated for the non-faulty variables may become higher than the same for the faulty variables [94], and control limits derived from the normal operating condition are not useful to isolate the faults. In order to overcome these drawbacks, various alternative approaches have been explored. Zhou [95] proposed a k-Nearest Neighbor (kNN) based technique to isolate multiple faulty variables without smearing effect. Alcala and Qin [96] proposed reconstruction-based contributions method which guarantees correct diagnosis for the single faulty variable even though fault smearing still exists. Liu [97] proposed an improved fault isolation technique using the reconstruction based contribution analysis ensuring correct isolation of multiple faulty variables without smearing effect. It was assumed that the faulty variables can be accurately reconstructed by the other measured variables. However, the reliability of the reconstruction procedure was not discussed.

Following this, a fault smearing free isolation in multi-scale PCA framework is identified as an open problem. Wavelet-based multi-scale PCA techniques are generally formulated in two different ways, namely, 1) the techniques in which wavelets are employed as a pre-processing tool, i.e., data are decomposed, thresholded at selected scales, and reconstructed back to the original measurement space,

then, a single PCA model is build using the processed data, 2) the techniques in which wavelets are used to decompose the data and multiple PCA models are build by using wavelet transformed coefficients. For the correlated data, the second techniques make more sense. This is because the use of wavelets can decorrelate the data, as PCA based techniques implicitly assume that data are uncorrelated, PCA models are built on the transformed data may comply with this assumption. It is widely known that single scale PCA process monitoring may not yield reliable results for the correlated data. However, the effect on the reliability of the process monitoring procedures in the light of the powerful decorrelation property of the wavelets has not been investigated. Moreover, the effective isolation of the faulty variables without fault smearing effect has been emphasised in past the few years[98][99]. In this regards, a reconstruction based fault isolation techniques have emerged as a promising candidate [100][101]. However, as these techniques work on the assumption that each of the measured variables can be reconstructed with the other measured variables, in order to assess the likelihood of the successful reconstruction, it important to evaluate the reliability of the reconstruction procedure.

Chapter 3

Estimation of Reactivity and Delayed Neutron Precursors' Concentrations Using multi-scale EKF

In this chapter, a discrete wavelet transform based multi-scale EKF technique for estimation of Reactivity and delayed neutron precursors' concentrations is presented. The proposed technique is based on and preserves the merits of EKF, at the same time use of wavelet transform effectively captures the multi-scale process variations. The description of the mathematical model of the nuclear reactor followed by the proposed estimation techniques and simulation results are presented in the subsequent sections.

3.1 Mathematical Model of Nuclear Reactor

Neutron density in a nuclear reactor is a function of time as well as space. But, the point kinetics model which assumes that the neutron distribution in space is constant in time provides adequate degree of accuracy. The model [102] assuming

small change in the reactivity is used for the purpose of estimation. It can be expressed as:

$$\dot{n} = \left(\frac{\rho - \beta}{l}\right) n + \sum_{i=1}^{6} \lambda_i C_i \tag{3.1}$$

$$\dot{C}_i = \frac{\beta_i}{l} n - \lambda_i C_i \,, \quad i = 1, 2, \cdots, 6 \tag{3.2}$$

where the variables ρ, n and C_i indicate reactivity, neutronic power and delayed neutron precursors' concentration of the i^{th} group respectively. β_i and λ_i are fraction and decay rate of the delayed neutron precursors of the i^{th} group with $\beta = \sum_{i=1}^{6} \beta_i$. l denotes prompt neutron lifetime.

Reactivity in (3.1) Reactivity is an input to the system which is also influenced by the internal reactivity feedbacks arising from the nuclear reactor. In this work, however, internal feedbacks are ignored and the net effect is considered as an unknown quantity, and it is modelled by the simple random walk model [103], i.e.,

$$\dot{\rho} = 0. \tag{3.3}$$

3.2 Estimation with EKF

In order to employ EKF algorithm described in Appendix B, the reference model given by (3.1) needs to be transformed into the state space form as:

$$\dot{\mathbf{x}} = f(\mathbf{x}) = \mathbf{F}_n \mathbf{x} \tag{3.4}$$

where the matrix $\mathbf{F}_n$ and the state vector $\mathbf{x}$ are defined as:

$$\mathbf{F}_n = \begin{bmatrix} \frac{-\beta}{l} & \lambda_1 & \lambda_2 & \cdots & \lambda_6 & \frac{n}{l} \\ \frac{\beta_1}{l} & -\lambda_1 & 0 & \cdots & 0 & 0 \\ \frac{\beta_2}{l} & 0 & -\lambda_2 & \cdots & 0 & 0 \\ \vdots & \vdots & \vdots & \ddots & \vdots & \vdots \\ \frac{\beta_6}{l} & 0 & 0 & \cdots & -\lambda_6 & 0 \\ 0 & 0 & 0 & \cdots & 0 & 0 \end{bmatrix} \tag{3.5}$$

$$\mathbf{x} = \begin{bmatrix} n & C_1 & C_2 & C_3 & C_4 & C_5 & C_6 & \rho \end{bmatrix}^\top \tag{3.6}$$

The superscript $\top$ denotes transpose of a vector. System represented by (3.4) is nonlinear due to the presence of the state variable n in $\mathbf{F}_n$ as well as in state vector $\mathbf{x}$. Jacobian of this nonlinear system can be defined as:

$$\mathbf{F} = \frac{\partial f(\mathbf{x})}{\partial \mathbf{x}} \tag{3.7}$$

All the elements of the matrix $\mathbf{F}$ will be same as the corresponding elements of the matrix $\mathbf{F}_n$ except the element $\mathbf{F}(1,7)$ which is given as $\mathbf{F}(1,7) = \frac{n}{l}$.

In order to apply EKF in the discrete-time domain, (3.4) must be transformed into a set of difference equations. If sampling is carried out at a uniform interval of T_s seconds, a set of difference equations are

$$\begin{aligned} \mathbf{x}[k] &= \mathbf{\Phi}_n[k-1]\mathbf{x}[k-1] + \mathbf{w}[k-1] \\ \mathbf{\Phi}_n[k] &= e^{\mathbf{F}_n[k]T_s} \end{aligned} \tag{3.8}$$

where k denotes the sampling instant. $\mathbf{w}$ is the system uncertainty which is assumed to have zero mean and covariance $\mathbf{Q}$. $\mathbf{F}_n[k]$ denotes the system matrix $\mathbf{F}_n$ defined by (3.5) at the k^{th} sampling instant. Similarly, discretization of Jacobian matrix is represented by $\mathbf{\Phi}_k = e^{\mathbf{F}[k]T_s}$ where $\mathbf{F}[k]$ denotes the Jacobian matrix $\mathbf{F}$ defined by (3.7) at the k^{th} sampling instant. The measurement process is governed

by the following equation:

$$\mathbf{z}[k] = \mathbf{H}\mathbf{x}[k] + \mathbf{v}[k] \tag{3.9}$$

where $\mathbf{v}$ is measurement noise with zero mean and covariance $\mathbf{R}$ and

$$\mathbf{H} = \begin{bmatrix} 1 & 0 & 0 & 0 & 0 & 0 & 0 & 0 \end{bmatrix}. \tag{3.10}$$

Now we have the system and measurement dynamics represented by (3.8) and (3.9) respectively. Appendix B indicates how the EKF algorithm can be applied to the dynamic systems represented in the form of (3.8) and (3.9).

3.2.1 Representation in multiscale framework

A multi-scale analysis is often used to effectively analyze fine and coarse variations of the signals or systems. The Appendix A gives the basic concepts.

Consider a sequence of a signal $s[n]$, $n \in \mathbb{Z}$ at scale depth $m = 0$ [21]. $s[n]$ can be decomposed into approximation and detail coefficients at scale level $m = 1$ using half band low pass filter (LPF) and high pass filter(HPF). Considering that the impulse responses of the LPF and HPF are $h_a[n]$ and $g_a[n]$ respectively, the approximation and detail coefficients of the DWT can be obtained by down-sampling the filter output by a factor of 2. The same can be written as

$$s_L^1[n] = \sum_k h_a[2n-k]s[k], \tag{3.11}$$

and

$$s_H^1[n] = \sum_k g_a[2n-k]s[k] \tag{3.12}$$

where $s_L^1[n]$ and $s_H^1[n]$ denote approximation and detail components at scale depth $m = 1$. The underlying consideration is that the coefficients of the filter banks meet the design criteria for the perfect reconstruction [104]. With synthesis filter bank having impulse response functions $h_s[n]$ and $g_s[n]$, the reconstructed signal can be written as

$$s[n] = \sum_k h_s[2k-n]s_L^1[k] + \sum_k g_s[2k-n]s_H^1[k].$$

For a sequence of the signal, it is convenient to describe a wavelet transform as an operator. Consider the portion of the signal s with length M at scale 0 denoted as

$$\boldsymbol{\varsigma}^0[k] = \begin{bmatrix} s[k-M]\, s[k-M+1] \cdots s[k-1] \end{bmatrix}^\top \tag{3.13}$$

It can be mapped to its approximation and detail components, $\boldsymbol{\varsigma}_L^1[k]$ and $\boldsymbol{\varsigma}_H^1[k]$, at next scale 1, using following transformation

$$\begin{aligned} \boldsymbol{\varsigma}_L^1[k] &= \mathbf{H}_a^1 \boldsymbol{\varsigma}^0[k] \\ \boldsymbol{\varsigma}_H^1[k] &= \mathbf{G}_a^1 \boldsymbol{\varsigma}^0[k] \end{aligned} \tag{3.14}$$

where the operators $\mathbf{H}_a^1$ and $\mathbf{G}_a^1$ map block of the signal at a scale 0 to that at 1. Rows of these operators are composed of appropriate translations of half band filters in (3.13). Conversely, signal at scale 1 can be mapped to that at 0 using operators $\mathbf{H}_s^1$ and $\mathbf{G}_s^1$ as

$$\boldsymbol{\varsigma}^0[k] = \mathbf{H}_s^1 \boldsymbol{\varsigma}_L^1[k] + \mathbf{G}_s^1 \boldsymbol{\varsigma}_H^1[k]. \tag{3.15}$$

Multi-scale signal analysis and synthesis can also be carried out with the filter bank as shown in Figure 3.1. The signals associated with the analysis side of block diagram are shown in Fig. 3.2. Whereas the signals associated with the synthesis side of the block diagram are shown in Fig. 3.3. These signals are obtained for one plant data-set selected for the simulation results discussed in section 3.3. Furthermore, EKF block shown in Figure 3.1 will also explained later. For instance, a m scale decomposition of $\boldsymbol{\varsigma}^0[k]$ can be carried out by the following analysis operator [21].

$$\boldsymbol{\varsigma}^m[k] = \mathbf{T}_a^m \boldsymbol{\varsigma}^0[k] \tag{3.16}$$

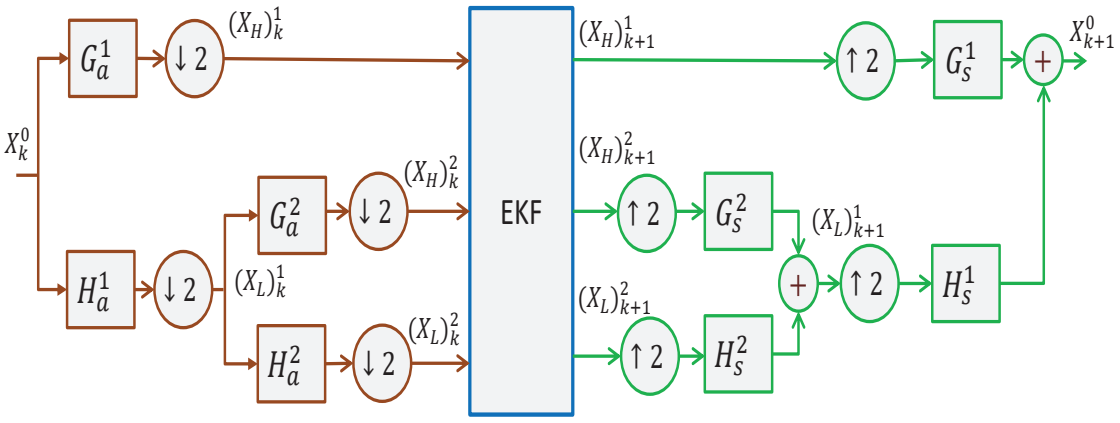

FIGURE 3.1: Block diagram representation for MEKF-2

where

$$\mathbf{T}_a^m = \left[\prod_{p=1}^{m} \mathbf{H}_a^p,\ \mathbf{G}_a^{m-1}\prod_{p=1}^{m-1} \mathbf{H}_a^p,\ \ \dots\ ,\mathbf{G}_a^1\right]^\top . \tag{3.17}$$

Selection of the wavelet basis function depends on time-frequency localization property needed for the particular application. In this application, Haar basis is used for the sake of simplicity in designing the operator $\mathbf{T}_a$. The bank of high pass and low pass filters for the Haar transform are given respectively as

$$\mathbf{H}_a = \left[\frac{1}{\sqrt{2}}\ \ \frac{1}{\sqrt{2}}\right] \quad \text{and} \quad \mathbf{G}_a = \left[-\frac{1}{\sqrt{2}}\ \ \frac{1}{\sqrt{2}}\right]. \tag{3.18}$$

Corresponding to the decomposition up to scale depth 2, the analysis operator in Eq. (3.16) can be given by the following orthogonal matrix.

$$\mathbf{T}_a^2 = \begin{bmatrix} \frac{1}{2} & \frac{1}{2} & \frac{1}{2} & \frac{1}{2} \\ -\frac{1}{2} & -\frac{1}{2} & \frac{1}{2} & \frac{1}{2} \\ -\frac{1}{\sqrt{2}} & \frac{1}{\sqrt{2}} & 0 & 0 \\ 0 & 0 & -\frac{1}{\sqrt{2}} & \frac{1}{\sqrt{2}} \end{bmatrix}. \tag{3.19}$$

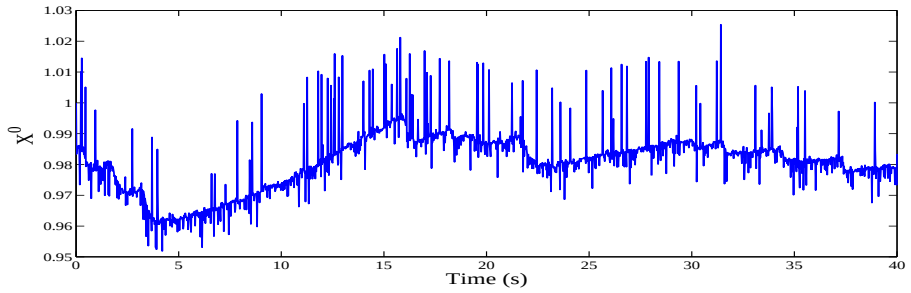

(a)

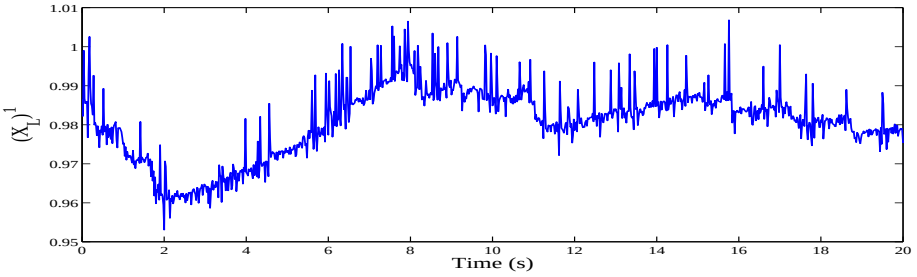

(b)

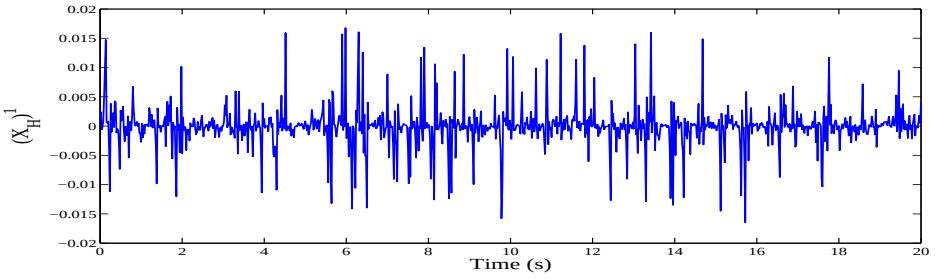

(c)

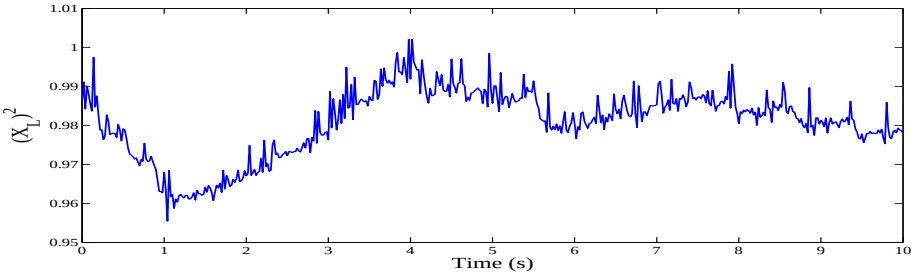

(d)

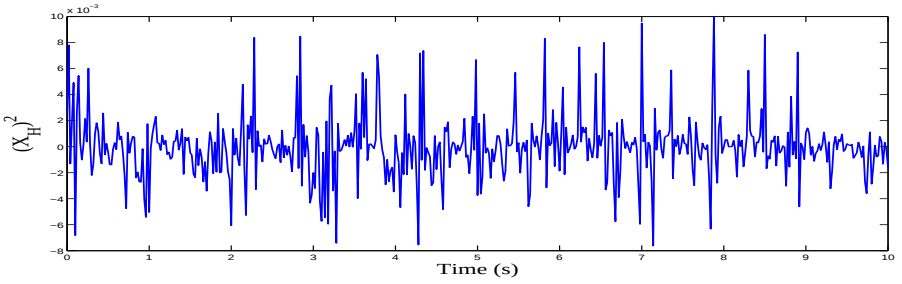

(e)

FIGURE 3.2: Signals at analysis side of Fig. 3.1(a)Measured Signal (b) Approximated coefficient at level-1(c) Detailed coefficient at level-1 (d) Approximated coefficient at level-1 (e) Detailed coefficient at level-2

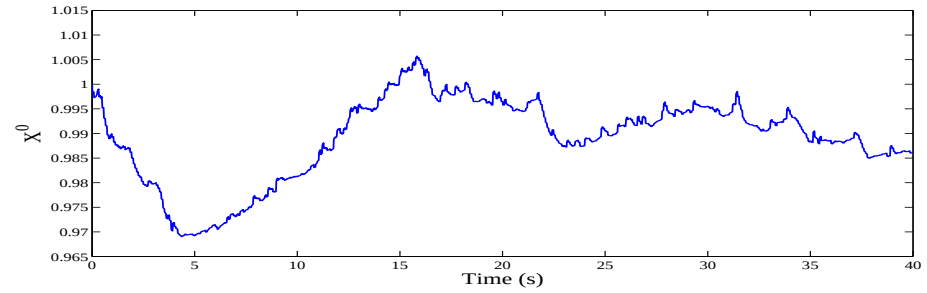

(a)

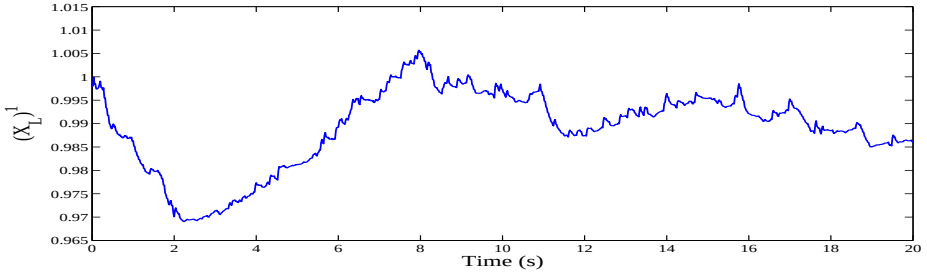

(b)

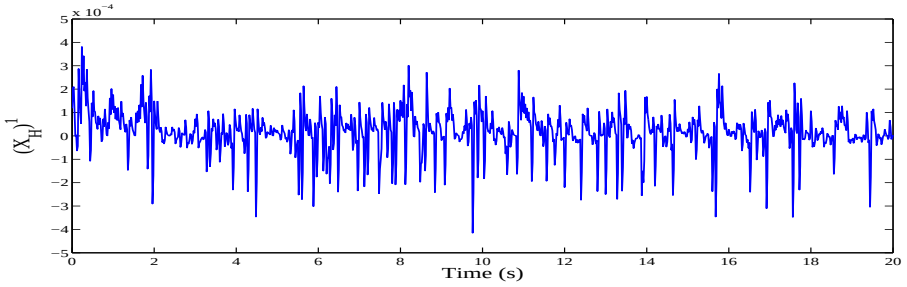

(c)

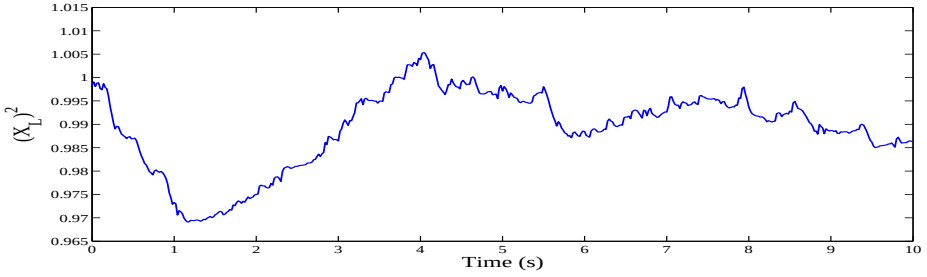

(d)

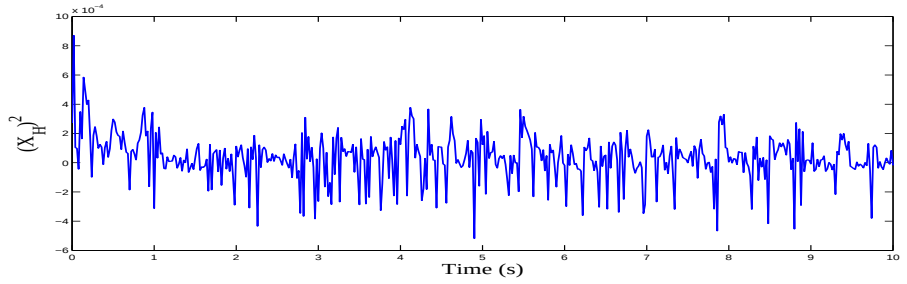

(e)

FIGURE 3.3: Signals at synthesis side of Fig. 3.1 (a)Estimated Signal (b) Approximated coefficient at level-1(c) Detailed coefficient at level-1 (d) Approximated coefficient at level-1 (e) Detailed coefficient at level-2

3.2.2 Estimation using multiscale EKF (MEKF)

Estimation algorithm for multi-scale EKF is presented in this subsection. For this purpose decomposition of the sequence of the state vector x defined by (3.6) is performed. Assuming that we have a sequence of the state vectors at resolution 0, we can have decomposition of the sequence at scale m by considering a block of $M = 2^m$ data points.

$$\mathbf{X}^0[k] = \left[\begin{array}{cccc} \mathbf{x}[k-M]^\top & \dots & \mathbf{x}[k-2]^\top & \mathbf{x}[k-1]^\top \end{array} \right]^\top. \tag{3.20}$$

In order to transform the system into the wavelet projection space, the equivalent system needs to be derived in data-block form as discussed in [21]. Generalization of this concept for the multivariable case can be obtained as explained in the following by assuming $\mathbf{\Phi}_n[k-1] = \mathbf{\Phi}_n[k-2] = \ldots = \mathbf{\Phi}_n[k-M] = \hat{\mathbf{\Phi}}_n$. The state equation given by (3.8) is rewritten as

$$\mathbf{x}[k] = \hat{\mathbf{\Phi}}_n \mathbf{x}[k-1] + \mathbf{w}[k-1] \tag{3.21}$$

or

$$\mathbf{x}[k] = \hat{\mathbf{\Phi}}_n^2 \mathbf{x}[k-2] + \hat{\Phi}\mathbf{w}[k-2] + \mathbf{w}[k-1] \tag{3.22}$$

or

$$\begin{aligned} \mathbf{x}[k] \;=\; & \hat{\mathbf{\Phi}}_n^{M-1} \mathbf{x}[k-M+1] + \hat{\mathbf{\Phi}}_n^{M-2} \mathbf{w}[k-M+2] + \\ & \ldots + \hat{\mathbf{\Phi}}_n \mathbf{w}[k-2] + \mathbf{w}[k-1] \end{aligned} \tag{3.23}$$

or

$$\begin{aligned} \mathbf{x}[k] \;=\; & \hat{\mathbf{\Phi}}_n^{M} \mathbf{x}[k-M] + \hat{\mathbf{\Phi}}_n^{M-1} \mathbf{w}[k-M+1] + \\ & \ldots + \hat{\mathbf{\Phi}}_n \mathbf{w}[k-2] + \mathbf{w}[k-1] \end{aligned} \tag{3.24}$$

Adding (3.21)-(3.24)

$$\begin{aligned}\mathbf{x}[k] &= \frac{1}{M}(\hat{\mathbf{\Phi}}_n^{M}\mathbf{x}[k-M] + \hat{\mathbf{\Phi}}_n^{M-1}\mathbf{x}[k-M+1] + \\ &\quad \ldots + \hat{\mathbf{\Phi}}_n^{2}\mathbf{x}[k-2] + \hat{\mathbf{\Phi}}_n\mathbf{x}[k-1]) + \mathbf{\Omega}_1. \end{aligned} \tag{3.25}$$

where

$$\mathbf{\Omega}_1 = \frac{1}{M}\left(\hat{\mathbf{\Phi}}_n^{M-1}\mathbf{w}[k-M] + 2\hat{\mathbf{\Phi}}_n^{M-2}\mathbf{w}[k-M+1] + \ldots + M\mathbf{w}[k-1]\right). \tag{3.26}$$

Similar representations for $\mathbf{x}[k+i]$, $i = 1, 2, \ldots, M-1$ can be obtained to have dynamic system in a data-block form, i.e.,

$$\mathbf{X}^0[k+1] = \mathbf{\Upsilon}_n[k]\mathbf{X}^0[k] + \mathbf{W}[k] \tag{3.27}$$

where

$$\mathbf{\Upsilon}_n[k] = \begin{bmatrix} \frac{1}{M}\hat{\mathbf{\Phi}}_n^{M} & \frac{1}{M}\hat{\mathbf{\Phi}}_n^{M-1} & \ldots & \frac{1}{M}\hat{\mathbf{\Phi}}_n \\ \mathbf{O} & \frac{1}{M-1}\hat{\mathbf{\Phi}}_n^{M} & \ldots & \frac{1}{M-1}\hat{\mathbf{\Phi}}_n^{2} \\ \vdots & \vdots & \ddots & \vdots \\ \mathbf{O} & \mathbf{O} & \ldots & \hat{\mathbf{\Phi}}_n^{M} \end{bmatrix}, \tag{3.28}$$

$$\mathbf{X}^0[k+1] = [\ \mathbf{x}[k]^\top \quad \mathbf{x}[k+1]^\top \quad \ldots \quad \mathbf{x}[k+M-1]^\top\ ]^\top, \tag{3.29}$$

and

$$\mathbf{W}[k] = [\ \mathbf{\Omega}_1 \quad \mathbf{\Omega}_2 \quad \ldots \quad \mathbf{\Omega}_M\ ]^\top, \tag{3.30}$$

where $\mathbf{O}$ is a zero matrix of order $N_s \times N_s$, N_s is the total number of state variables. $E(\mathbf{W}[k]) = \mathbf{0}$ and $E(\mathbf{W}[k]\mathbf{W}[k]^\top) = \bar{\mathbf{Q}}$.

Similarly we can define discretized Jacobian matrix $\mathbf{\Upsilon}[k]$ by replacing $\hat{\mathbf{\Phi}}_n$ of (3.28) by $\hat{\mathbf{\Phi}}$ where $\hat{\mathbf{\Phi}} = \mathbf{\Phi}[k-1] = \mathbf{\Phi}[k-2] = \ldots = \mathbf{\Phi}[k-M]$. The measurement model associated with (3.9) can be written in data block form as

$$\mathbf{Z}[k] = \mathbb{H}\mathbf{X}^0[k] + \mathbf{V}[k] \tag{3.31}$$

where $\mathbf{Z}[k] = [\mathbf{z}[k-M]\ \mathbf{z}[k-M+1] \ldots\ \mathbf{z}[k-1]]^\top$ and $\mathbb{H} = diag.[\mathbf{H}\ \ \mathbf{H} \ldots\ \mathbf{H}]$.

Further, $E(\mathbf{V}[k]) = \mathbf{0}$ and $E(\mathbf{V}[k]\mathbf{V}[k]^\top) = \bar{\mathbf{R}}$. In order to have a two level decomposition, sequence of each state variable corresponding to state vectors $\mathbf{x}$ needs to be filtered through analysis filter bank. Assuming that measurements are taken at scale 0, let us define an operator $\mathbb{T}_a^m$, a square matrix of the order $N_s \times M$ which maps X_k^0 to scale m as

$$\mathbf{X}^m[k] = \mathbb{T}_a^m \mathbf{X}_k^0. \tag{3.32}$$

Key elements of the operator can be written as

$$\mathbb{T}_a^m(N_s(i-1)+k, N_s(j-1)+k) = \mathbf{T}_a^m(i,j) \tag{3.33}$$

where $i, j = 1, 2, ..., M$ and $k = 1, 2, ..., N_s - 1$. The rest of the elements of the matrix $\mathbb{T}_a^m$ are zero. Using (3.32) into (3.27) we can obtain:

$$\mathbf{X}^m[k+1] = \bar{\mathbf{\Upsilon}}_n[k]\mathbf{X}^m[k] + \bar{\mathbf{W}}[k] \tag{3.34}$$

where $E(\bar{\mathbf{W}}[k]) = \mathbf{0}$, $E(\bar{\mathbf{W}}[k]\bar{\mathbf{W}}[k]^\top) = \hat{\mathbf{Q}}$ and $\bar{\mathbf{\Upsilon}}_\mathbf{n}[\mathbf{k}] = \mathbb{T}_a^m \mathbf{\Upsilon}_\mathbf{n}[\mathbf{k}] \left(\mathbb{T}_a^m\right)^\top$, $\bar{\mathbf{W}}[k] = \mathbb{T}_a^m \mathbf{W}[k]$, $\hat{\mathbf{Q}} = \mathbb{T}_a^m \bar{\mathbf{Q}} \left(\mathbb{T}_a^m\right)^\top$. The model described by (3.34) is a multi-resolution model corresponding to dynamical system described by (3.27). Measurement model associated with this system can be obtained by substituting (3.32) into (3.31), which yields:

$$\mathbf{Z}[k] = \bar{\mathbb{H}}\mathbf{X}^m[k] + \mathbf{V}[k] \tag{3.35}$$

where $\bar{\mathbb{H}} = \mathbb{H}\left(\mathbb{T}_a^m\right)^\top$. Now, we have a system represented by (3.34) and measurement model represented by (3.35). Now, EKF algorithm as described in Appendix B can be employed to optimally estimate decomposed states. States of the original system can be synthesised from optimally estimated states at multiple scales by application of the inverse operator $\mathbb{T}_s^m = \left(\mathbb{T}_a^m\right)^\top$. This algorithm is denoted by MEKF-m if the estimation runs upto the scale depth m. The block diagram representation for the MEKF-2 algorithm is shown in Figure 3.1.

Remark: It is to be noted that while deriving an equivalent system in a datablock form, linearity in a system is assumed for a time duration equivalent to the number of samples in a block of data. This means that the equivalent system derived at

the wavelet scale m, is regarded to be linear for 2^m samples. Consequently, the prediction step of the multi-scale EKF would work on such a linearity assumption.

Computational complexity

It may be noted that the dimensions of matrices and state vectors associated with the MEKF algorithm are higher than those of the EKF. Therefore, computational complexity of MEKF relative to EKF is expected to be higher. The most complex step in the EKF iterations is Eq. (B.4). It requires multiplication of an $n \times n$ matrix with another $n \times n$ matrix. With one of the best known techniques, i.e, the Coppersmith-Winograd algorithm it runs to $O(n^{2.376})$ [105]. Therefore, the total time complexity of the EKF algorithm is also $O(n^{2.376})$. In case of MEKF-m, the dimension of the state vector is higher by a factor of 2^m. Therefore, time required to perform single iteration is increased by a factor $2^{2.376m}$. However, as MEKF-m is derived with a block of 2^m datapoints, the number of iterations required to perform total computation is reduced by a factor 2^m. Hence, relative to EKF, the overall computation time required to perform MEKF-m is increased by a factor $F = 2^{2.376m-m} = 2^{1.376m}$, i.e, with the increment in the scale depth by one level, the computation time increases by a factor $2^{1.376}$ than that at the previous scale.

3.3 Simulation Results and Discussions

In this section simulation results from EKF and Wavelet based Multiscale EKF techniques are presented. Simulations were carried out for two cases: (1) using reference data set and (2) using experimental data set collected from a research reactor. In the first case, data set is generated by exciting the point kinetics model of the reactor by a known reactivity variation and the power variation thus obtained is used as an input to estimation algorithms. While, in the second case, two datasets, collected from one of the Indian research reactors are used for estimation purpose. Details of the datasets followed by corresponding simulation results are presented in the following subsections.

3.3.1 Simulations using reference data set

As mentioned earlier, this data set is generated by using point kinetics model of the nuclear reactor given by (3.1) and (3.2) by subjecting it to reactivity variation shown in Figure 3.4. Delayed neutron parameters used in the simulation are shown in Table 3.1. Initially, the reactor is assumed to be in a steady-state at 1 unit power and delayed neutron precursors' concentrations are in equilibrium corresponding to this power level. Measurement noise of zero mean and variance equal to 10% of the nominal value of reactor power is added to the output generated from the simulation. Figure 3.5 shows the output power variation with noise.

For the EKF, the values of $\mathbf{R}$ and $\mathbf{Q}$ which denote covariances of measurement noise and system uncertainty are selected as 1×10^{-2} and diag. $[0, 0, 0, 0, 0, 0, 5 \times 10^{-8}]$ respectively. Wavelet-based estimation algorithm is expected to give better estimation results besides providing multi-scale analysis of the signals. The sequences of the state variables are analysed upto 5 different scales.

Figures 3.6 through 3.13 show outputs obtained form EKF and MEKF algorithms described in the previous section. In each plot, zoomed variation over a small interval is also shown in an inset box. It is assumed that input signal to the estimation algorithm i.e. simulated power variation is at scale 0. To assess the filtering effect, results obtained only from MEKF-2 through MEKF-5 are plotted in the Figure 3.6 through Figure 3.13. As defined earlier, MEKF-$m, m = 2, 3, \cdots, 5$ are the state estimation algorithms which estimate the system states by synthesizing optimally estimated analyzed states upto scale depth m. Although the computations

TABLE 3.1: Delayed neutron data for the reference dataset.

Group Index	$\beta_i\,(\times10^{-3})$	$\lambda_i\,(s^{-1})$
1	0.2112	0.0124
2	1.4016	0.0305
3	1.2544	0.111
4	2.5280	0.310
5	0.7360	1.140
6	0.2688	3.010

Prompt neutron generation time, $l = 10^{-3}$ s

could be successfully carried out upto scale depth 5, numerical ill-conditioning was encountered for scale 6 and beyond.

The quantitative performance of the proposed algorithm can be assessed by observing the mean squared error (MSE) defined as

$$MSE = \frac{1}{n}\sum_{i=1}^{n}\left(Y_i - \hat{Y}_i\right)^2 \tag{3.36}$$

where n is the total number of samples, and Y_i and $\hat{Y}_i$ denote estimated and reference quantities respectively. MSE for estimation of the variables with EKF and MEKF-m, $m = 2$ to 5 are given in Table 3.2. For this purpose 50 runs of the Monte Carlo simulations have been considered. It can be observed that the values of MSE in the estimation of fast varying states, i.e., reactivity and neutronic power are comparatively smaller for MEKF-5 than those for EKF. Moreover, there is a marginal improvement for the estimates of delayed neutron precursors' concentrations of group 2 to 5 at a particular intermediate scale. It is evident that groups of delayed neutron precursors suffer from the over smoothing after a certain scale.

TABLE 3.2: Mean Squared Error (50 Monte Carlo runs)

Quantity	Mean Squared Error				
	EKF	MEKF-2	MEKF-3	MEKF-4	MEKF-5
$\rho(\times 10^{-7})$	7.2571	6.9342	6.5412	5.87613	**5.2458**
$p(\times 10^{-4})$	1.3917	1.3478	1.2985	1.2105	**1.0878**
$C_1(\times 10^{-6})$	7.6360	**7.6244**	7.6349	7.9246	11.3082
$C_2(\times 10^{-5})$	1.2872	**1.2851**	1.2861	1.3372	1.84024
$C_3(\times 10^{-5})$	2.5379	**2.5306**	2.5271	2.6152	3.3703
$C_4(\times 10^{-5})$	4.2033	4.1804	**4.1658**	4.2614	4.9821
$C_5(\times 10^{-5})$	7.7699	7.6822	7.6226	**7.5894**	7.6794
$C_6(\times 10^{-4})$	1.0750	1.0568	1.0400	0.9982	**0.9563**

3.3.2 Simulations using plant data

As already stated earlier, the proposed estimation algorithm has also been tested on the plant data of a research reactor known as 'Apsara' [106]. It was operational till the year 2010. The reactor designed for 1 MW thermal power capacity, used an enriched uranium fuel and water as a coolant. Reactivity in it was regulated by four cadmium control rods, three of them having higher worth are called shim rods.

These were used for regulation of power as well as protection. The fourth control rod, namely a fine control rod was used for a fine control of the power. To regulate the reactor power shim rods were manually moved upward or downward as a single bank. The fine control rod position was regulated based on the difference between demand power and measured power. In the operating range, reactor power was measured by seven range linear dc channel (MRDC channel) and a six-decade log channel.

For comparison, both EKF and MEKF algortithms are employed to estimate the state variables using experimental datasets collected from the Apsara reactor. As mentioned earlier, two different cases have been considered. In the first case, power variation data are collected during one of the experiments where reactor power is increased by a factor of 2.5 from its initial power level of 9.7 kW, held constant at the new level for a short time and subsequently decreased to the initial level of 9.7 kW. In the second case, the power variation data are collected while reactor undergoes a shutdown from its initial power of 201 kW followed by a restart to reach the same power level. In both cases, neutronic power variations are normalized to full power, i.e, 1 MW. Further, assumption is that the reactor is at steady state and delayed neutron precursors' concentrations are in equilibrium corresponding to the initial power level. The delayed neutron parameters corresponding to the Apsara reactor are given in Table 3.5.

Measured neutronic power with time variation depicted in Figure 3.14 serves as an input to the estimation algorithms in the first case. The performance of the EKF algorithm depends on the values of the tuning parameters $\mathbf{Q}$ and $\mathbf{R}$, and these

TABLE 3.3: Delayed neutron parameters for a research reactor

Group Index	$\beta_i\,(\times 10^{-3})$	$\lambda_i\,(s^{-1})$
1	0.2487	0.0120
2	1.3800	0.0317
3	1.1990	0.1183
4	2.6270	0.3101
5	1.3790	0.9617
6	0.6799	2.8930

Prompt neutron generation time, $l = 9.2939 \times 10^{-4}$ s

need to be chosen carefully. Generally, ratio between **Q** and **R** matters [107], rather than their absolute values. Therefore, The value of **R** is chosen as 1. But selection of parameter **Q** is very important as it is associated with the modeling uncertainty of the system. As per the procedure given in [20], for the fixed value of **R**, value of **Q** is tuned in such a way that the covariance of innovation process at steady state achieves minimum value. Pattern of the **Q** matrix is selected as $diag.[0\ 0\ 0\ 0\ 0\ 0\ 0\ q]$. Figure 3.15 shows values of variance of the innovation process against q. Further, it has been noticed that with the increment in the value of q, noise level in the estimated quantities increases. On the contrary, with the decrement in q, variation of estimated quantities becomes sluggish. Thus, the value of q is selected as 1×10^{-3} which corresponds to the minimum covariance of innovation process as 1.7×10^{-8} as shown in Figure 3.15.

Similar to the case of the synthetic dataset, computation beyond the scale depth 5 encounters numerical ill-conditioning. Figure 3.16 through Figure 3.23 show the output of the estimation algorithm for the first case. It can be seen that MEKF-5 technique gives smoother variations of the state variables i.e., noise is removed more effectively.

In the second case, where the reactor undergoes a shutdown followed by a restart, the measured neutronic power varies as shown in Figure 3.24. It can be observed that the noise in the measurement decreases in the shutdown phase and subsequently increases after the restart. In this case, MEKF computations upto the scale depth 4 have been performed. For scale depth 5 and beyond, estimation results from MEKF diverge due to numerical ill-conditioning. Figure 3.25 through Figure 3.32 show the estimation results. Again, the estimation results are better with MEKF than those from EKF in the operating condition where the level of measurement noise is significant. This is expected because denoising is known to work better in the wavelet domain.

3.3.3 Validation of the results

In order to justify the performance of the estimation algorithm, two performance measures have been considered: (1) reactivity obtained from the physical experiments and (2) the error sequence between measured variable, i.e., power and its estimate. As regards the reactivity obtained from the physical experiments, it can be used as a reference. Estimated reactivity variations obtained from EKF and MEKF are compared with this reference reactivity as shown in Figure 3.33. While error sequence between reference reactivity and estimated reactivity are shown in Figure 3.34. It can be seen that estimation results from both the techniques are in agreement with the reference reactivity. However, the reactivity estimated by MEKF technique not only gives smoother response but also gives lesser error.

Performance of the estimation algorithm can also be justified by statistical properties of the error sequence obtained from the difference between the measured variable and estimate of the variable. In this case, neutronic power is being measured. So, the error sequence between measurement and estimation of neutronic power gives considerable information. Figures 3.39 and Figure 3.40 show difference between normalized measured power and estimated power by EKF and MEKF for the first and second case respectively.

The estimation results can be validated by analysing 'Whiteness' of the error between the measured signal and the estimated signal [42]. Whiteness can be analysed by evaluating the ACF (auto-correlation function). For the transients under consideration, i.e, a power rise followed by a fall, and a shutdown followed by a restart, the ACF considering 20 lags are plotted in Fig. 3.37 and Fig. 3.38 respectively. For the first transient, from Fig. 3.37, it can be observed that error sequence obtained for MEKF-5 is significantly less autocorrelated than that of the other estimation algorithms. Furthermore, for the second transient, Fig. 3.37 indicates overall rise in ACF coefficients for all the state estimation techniques. However, it can be also be noted that the error sequence obtained for EKF seems relatively less autocorrelated than its multi-scale counterparts. For sake of better understanding of these observations, it would be useful to have quantitative analysis for whiteness. Numerous statistical tests for quantification of whiteness have

been reported in the literature. Considering a criteria reported in [108], Ljung-Box Q test statistic is defined as follows

$$\mathbf{LBQ} = N(N+2)\sum_{l=1}^{L}\frac{\rho_l^2}{N-l} \tag{3.37}$$

where N is the number of samples, ρ_l is the autocorrelation coefficients at lag l, and L is the number of lags being tested. As discussed in [108], for the time-independent samples **LBQ** statistic approximately follows the χ^2 distribution with L degrees of freedom. For both the transients, i.e., a power rise followerd by a fall, and a shutdown followed by a restart, values of test statistic **LBQ** are tabulated in Table 3.4 and Table 3.5 respectively. From Table 3.4, it can be noted that, for a first transient values for **LBQ** statistic are significantly lower for MEKF-5 than that for other estimation algorithms. This establish that MEKF-5 performs better than with the the other estimation algorithm under investigation. Furthermore, Table 3.4 suggests overall rise in the autocorrelation for a second transient. This can be explained by the fact that for a severe transient such a reactor shutdown, noise in the measured power of the reactor does not have constant variance. Therefore, the values of the tuning parameters Q and R, selected at a steady state, before occurrence of shutdown are not optimal for estimation throughout the observation. Consequently, the estimated values derived from the EKF and MKEF are not optimal for entire observation which is resulted as rise in LBQ test statistic. Furthermore, this observation also indicates that estimation results obtained with multi-scale EKFs are relatively more susceptible to the sub-optimal tuning parameters.

TABLE 3.4: LBQ test statistic for a power rise followed by a fall

Estimator	EKF	MEKF-2	MEKF-3	MEKF-4	MEKF-5
LBQ($\times 10^2$)	9.2598	3.2849	2.9893	3.1286	**2.6353**

TABLE 3.5: LBQ test statistic for a shutdown followed by a restart

Estimator	EKF	MEKF-2	MEKF-3	MEKF-4
LBQ($\times 10^3$)	**2.4907**	4.2201	3.7599	3.6640

As the estimation algorithms are expected to remove the noise from the measured signal, the quality of the estimation can also be judged by the variance of the error between the measured signal and the estimated signal. If the variance of the error is high, then one can conclude that more noise-power has been removed. Further, one can expect this error to be of zero mean with the assumption that the noise in the measured signal is bias-free. Therefore, an error sequence is expected to be of zero mean and variance is expected to be high, i.e., better estimation algorithm rejects the Gaussian noise more effectively. In the steady state operation of the first case, the values for mean and variance of the error sequence for standard EKF technique are 7.4657×10^{-8} and 1.1766×10^{-8} respectively, while those for MEKF-5 technique are 2.8070×10^{-7} and 1.5859×10^{-8} respectively. Larger variance obtained using MEKF establishes that multiscale EKF technique gives better performance.

3.4 Summary

In this chapter, a multiscale EKF technique for estimation of reactivity and delayed neutron precursors' concentration is investigated. The proposed algorithm preserves the merits of EKF technique and at the same time, the use of wavelets provides an additional smoothing effect for the estimation. The multiscale analysis allows online identification of the frequency components of the signals. This helps in modeling widely varying dynamic modes of a multi-scale reactor system. The proposed algorithm handles the system uncertainties and measurement noise using system covariance matrices $\mathbf{Q}$ and $\mathbf{R}$ which are tuned to have the optimal performance. Although the proposed algorithm is computationally expensive, it does not impose severe limitation with the use of modern high-speed digital computers. Performance of the proposed algorithm is assessed by carrying out estimation from the completely known dataset as well as plant dataset of one of the Indian research reactors. It is found that the proposed algorithm outperforms the standard EKF algorithm. However, it is also noted that the performance of the proposed algorithm is more susceptible with the sub-optimal tuning parameters than that of the standard EKF.

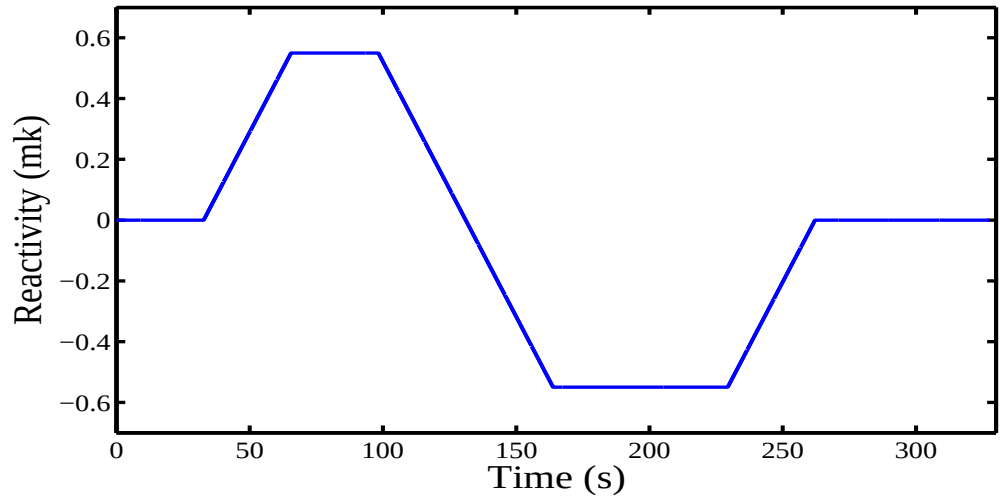

FIGURE 3.4: Reference reactivity variation

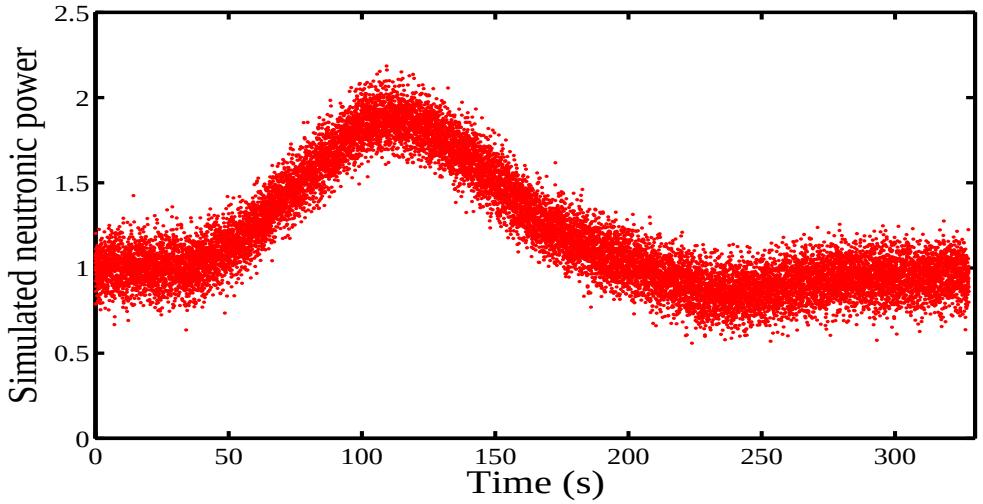

FIGURE 3.5: Simulated neutronic power

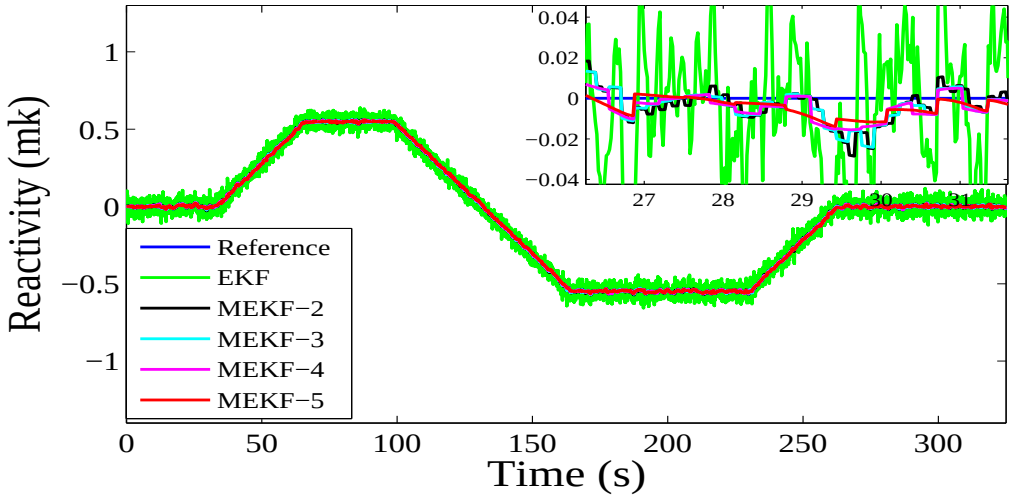

FIGURE 3.6: Reactivity

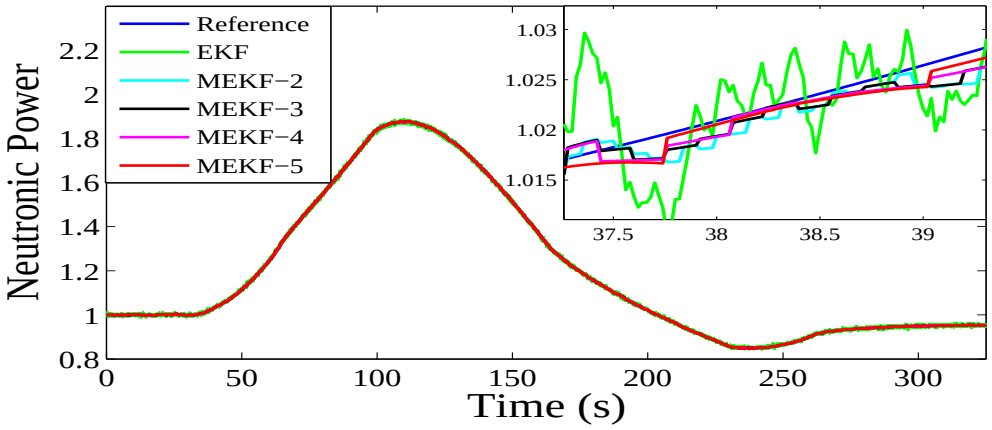

FIGURE 3.7: Neutrnoic Power

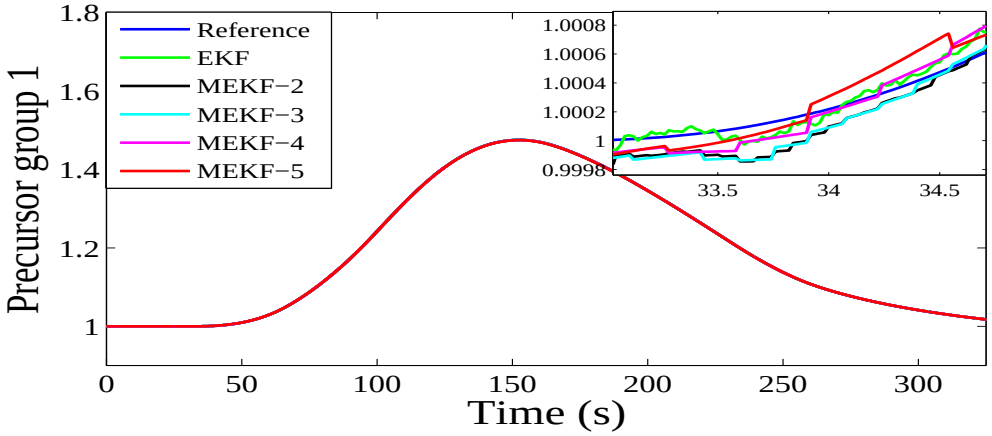

FIGURE 3.8: Concentration of a delayed neutron Precursor Group 1

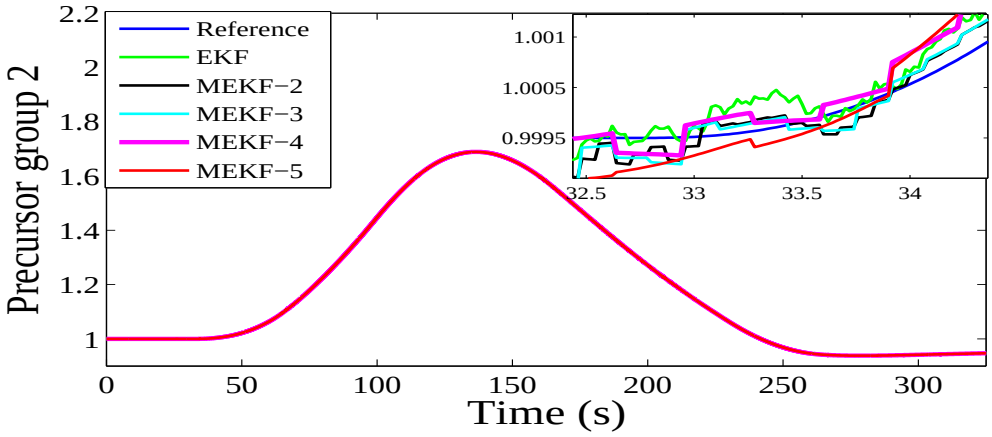

FIGURE 3.9: Concentration of a delayed neutron Precursor Group 2

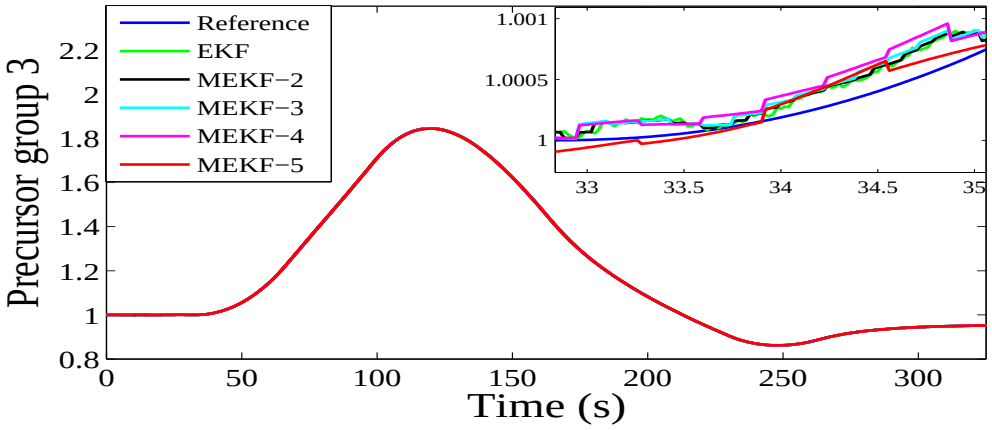

FIGURE 3.10: Concentration of a delayed neutron Precursor Group 3

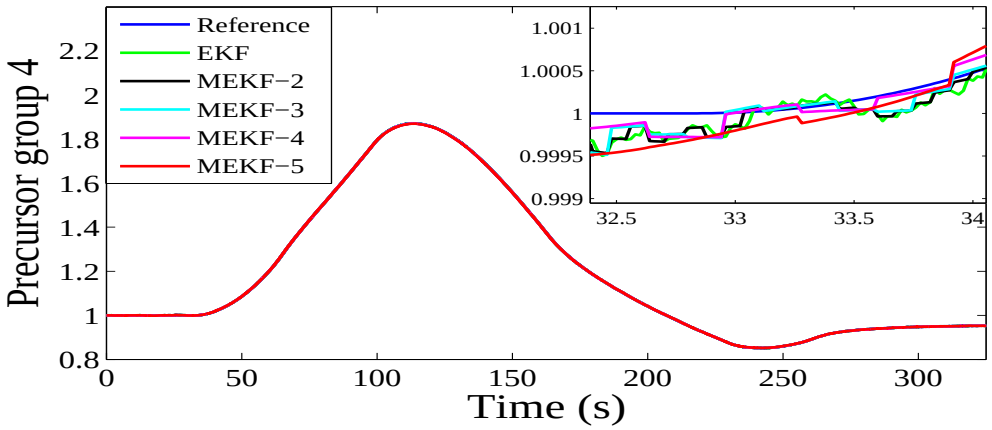

FIGURE 3.11: Concentration of a delayed neutron Precursor Group 4

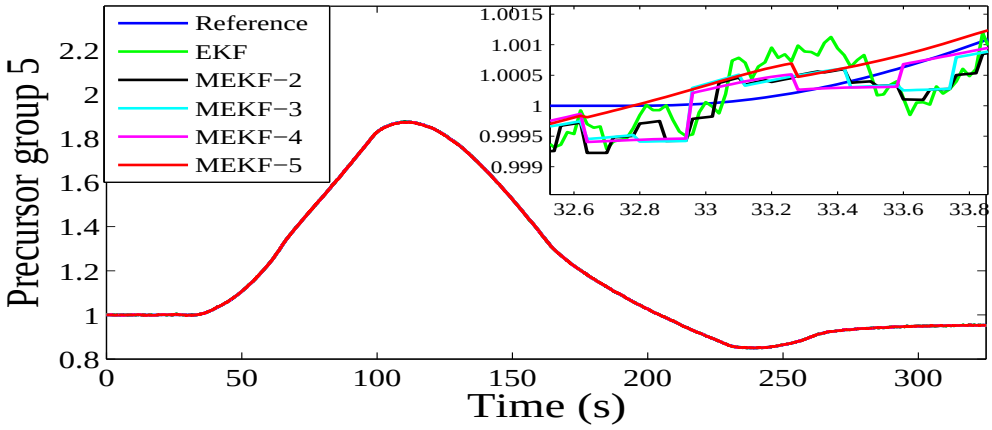

FIGURE 3.12: Concentration of a delayed neutron Precursor Group 5

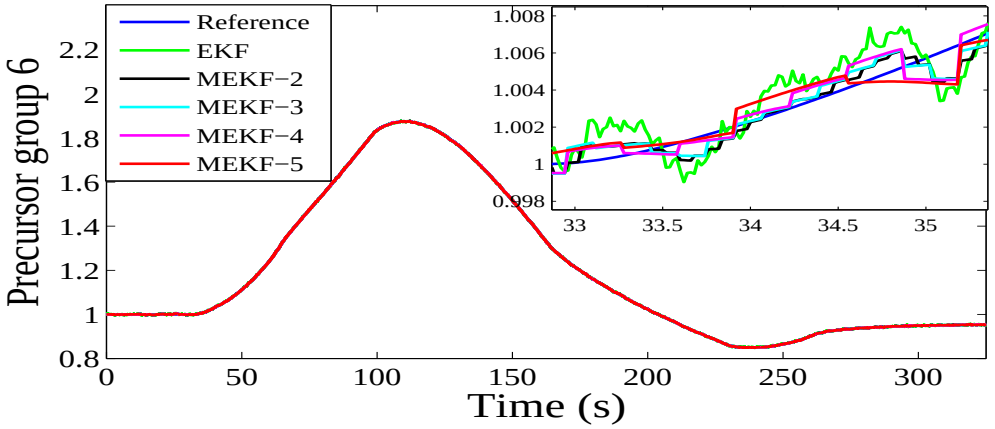

FIGURE 3.13: Concentration of a delayed neutron Precursor Group 6

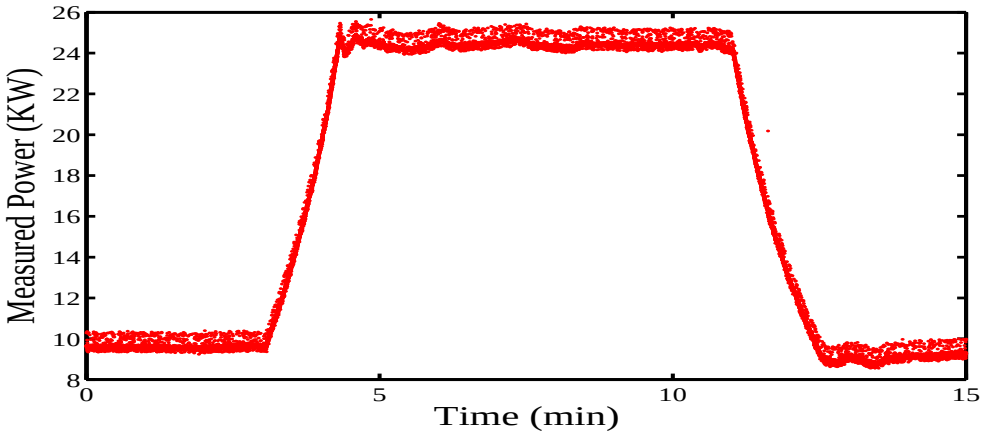

FIGURE 3.14: Measured neutronic Power of the research reactor

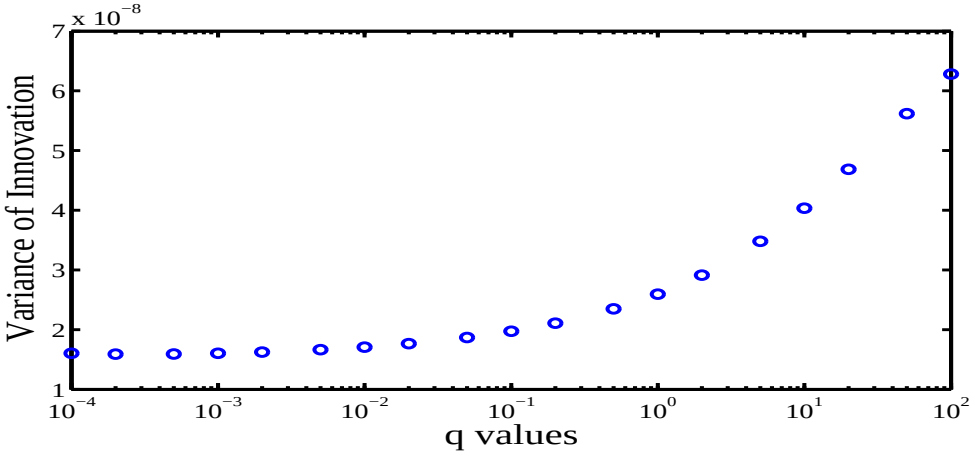

FIGURE 3.15: Variance of innovation process with tuning parameter q

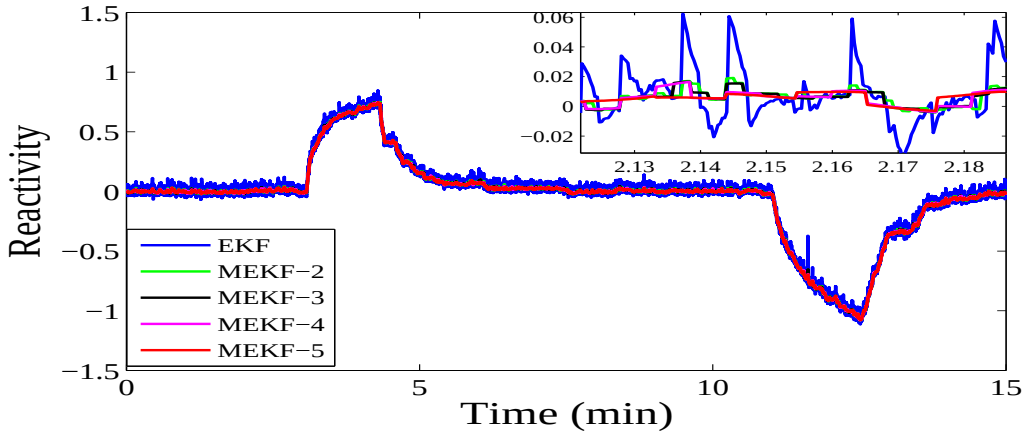

FIGURE 3.16: Reactivity variation for power rise followed by fall

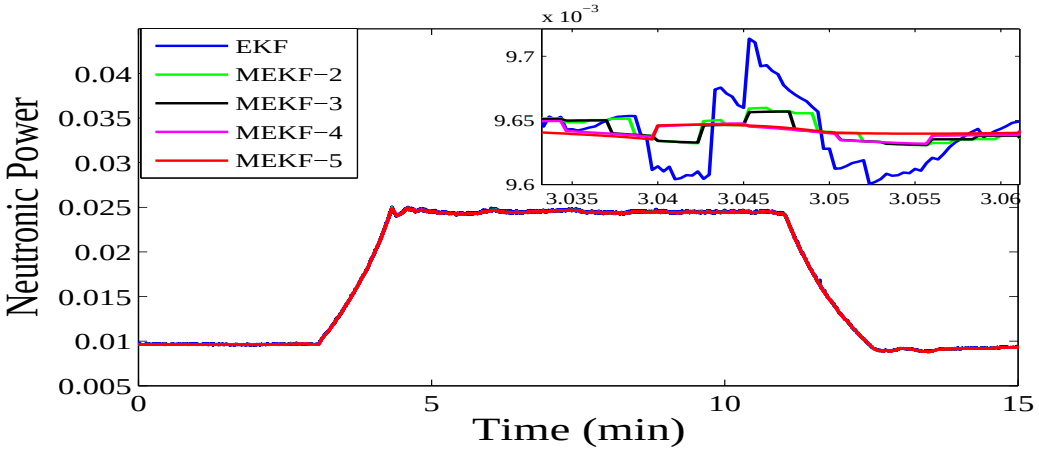

FIGURE 3.17: Estimated neutrnoic power variation for power rise followed by fall

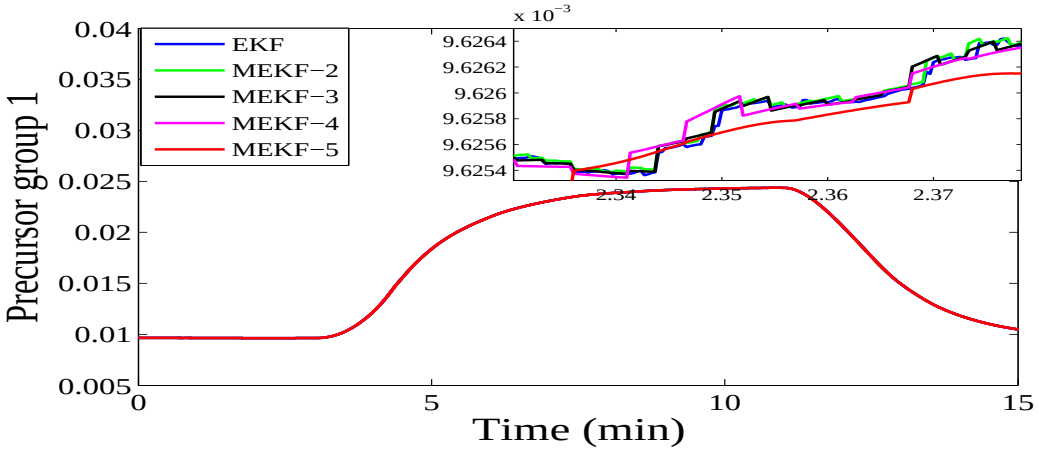

FIGURE 3.18: Concentration of a delayed neutron Precursor Group 1 for power rise followed by fall

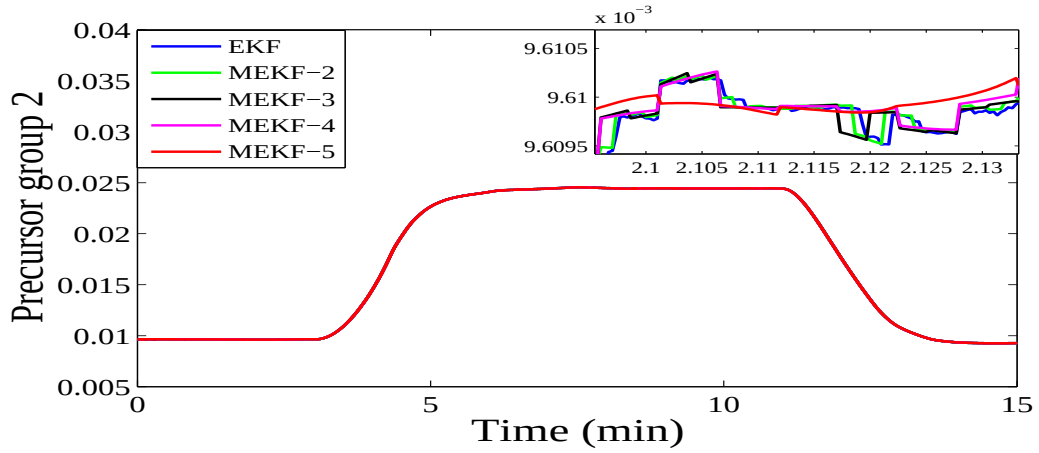

FIGURE 3.19: Concentration of a delayed neutron Precursor Group 2 for power rise followed by fall

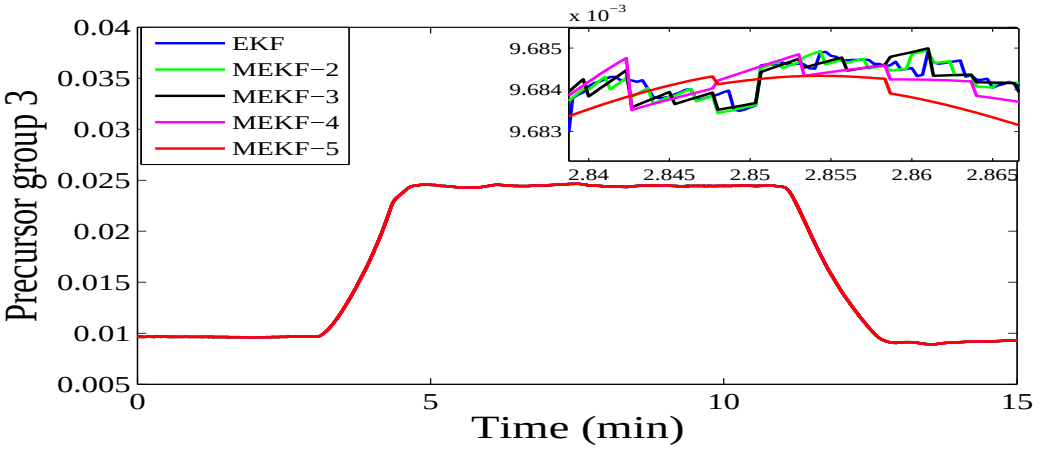

FIGURE 3.20: Concentration of a delayed neutron Precursor Group 3 for power rise followed by fall

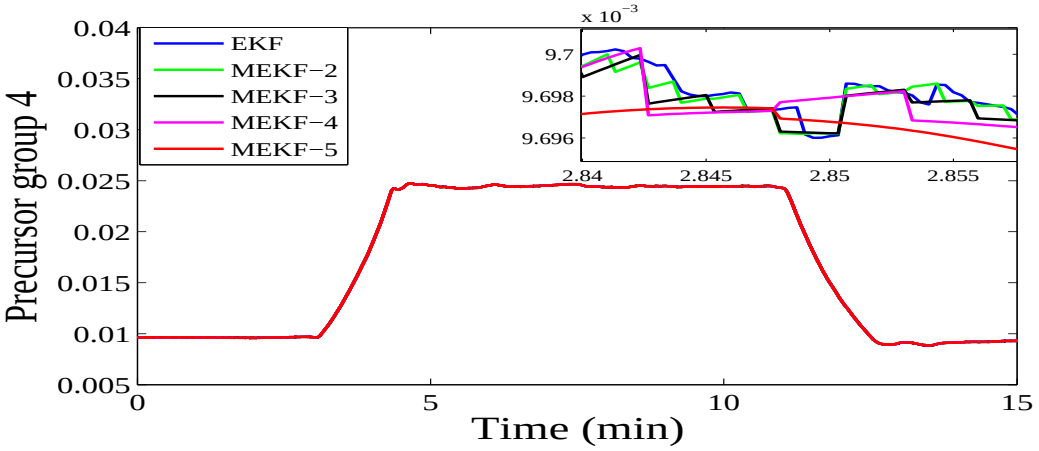

FIGURE 3.21: Concentration of a delayed neutron Precursor Group 4 for power rise followed by fall

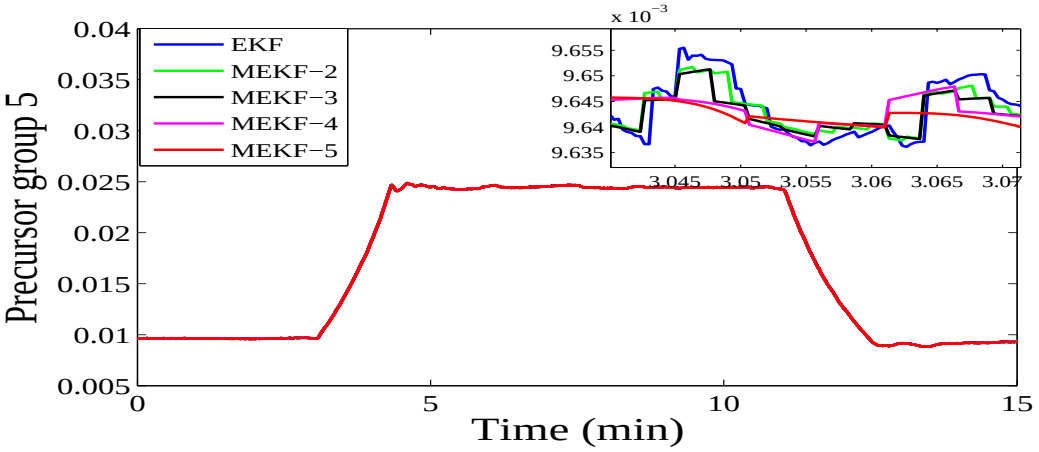

FIGURE 3.22: Concentration of a delayed neutron Precursor Group 5 for power rise followed by fall

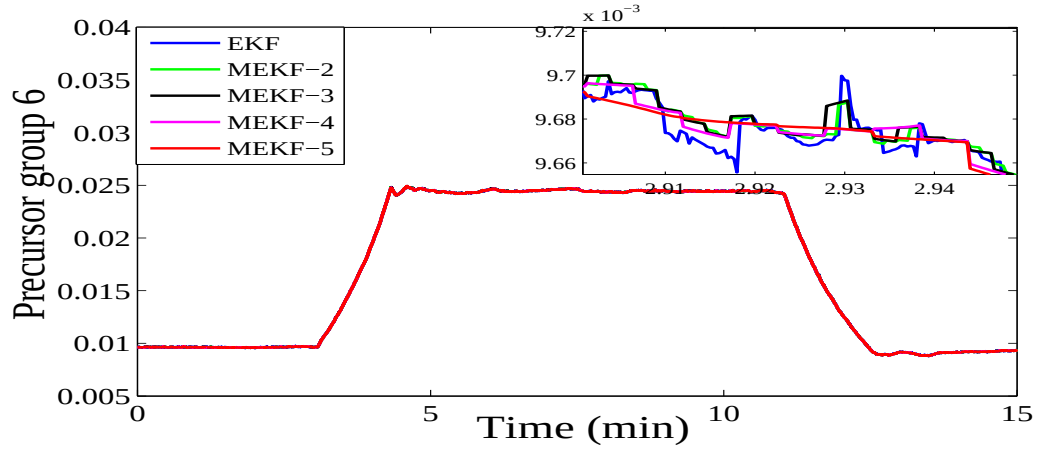

FIGURE 3.23: Concentration of a delayed neutron Precursor Group 6 for power rise followed by fall

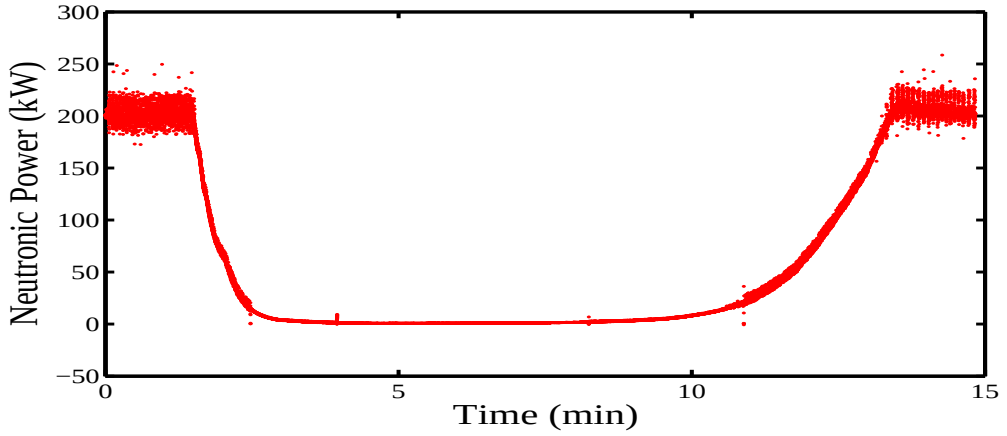

FIGURE 3.24: Measured neutronic power for shutdown followed by restart

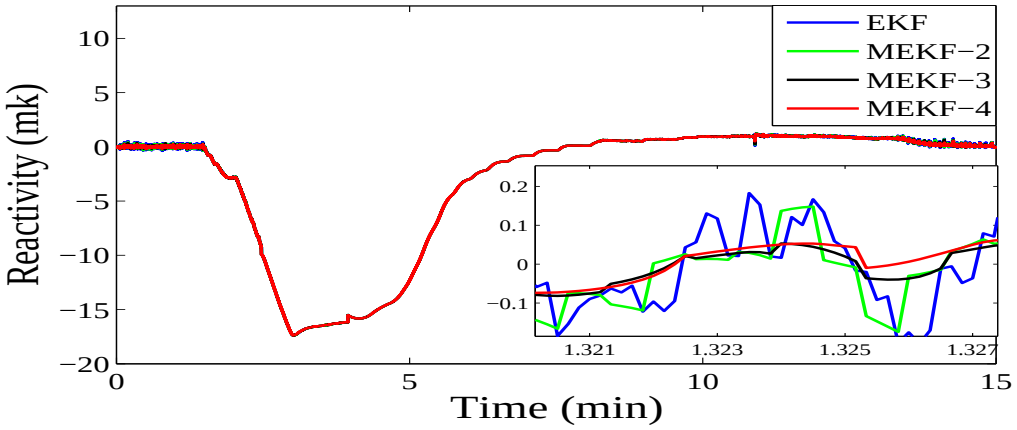

FIGURE 3.25: Reactivity variation for shutdown followed by restart

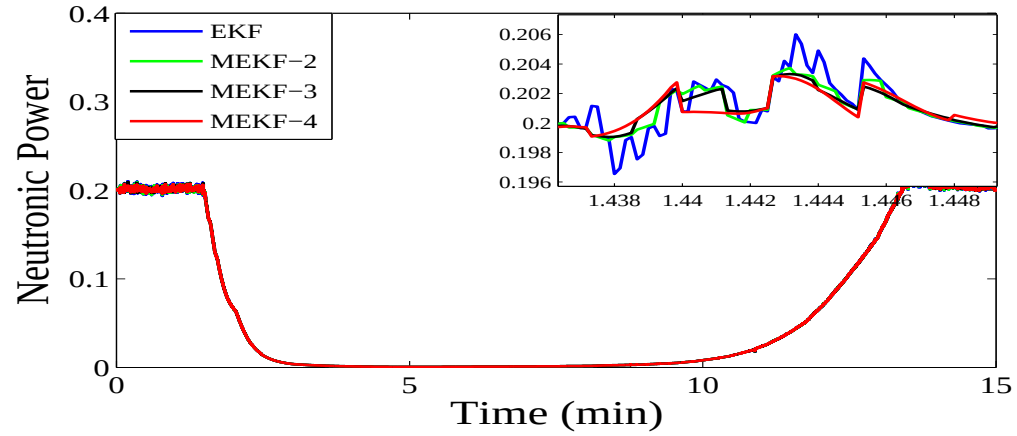

FIGURE 3.26: Neutronic power variation for shutdown followed by restart

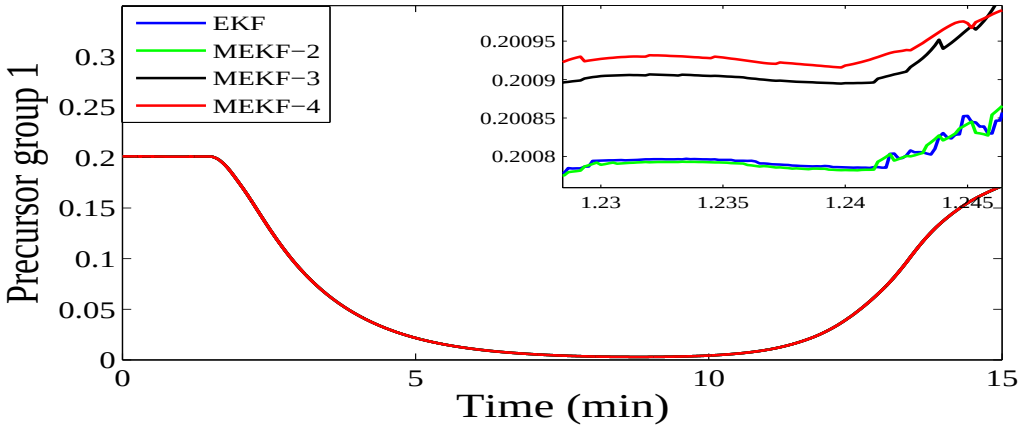

FIGURE 3.27: Delayed neutron precursors' concentration of group 1 for shutdown followed by restart

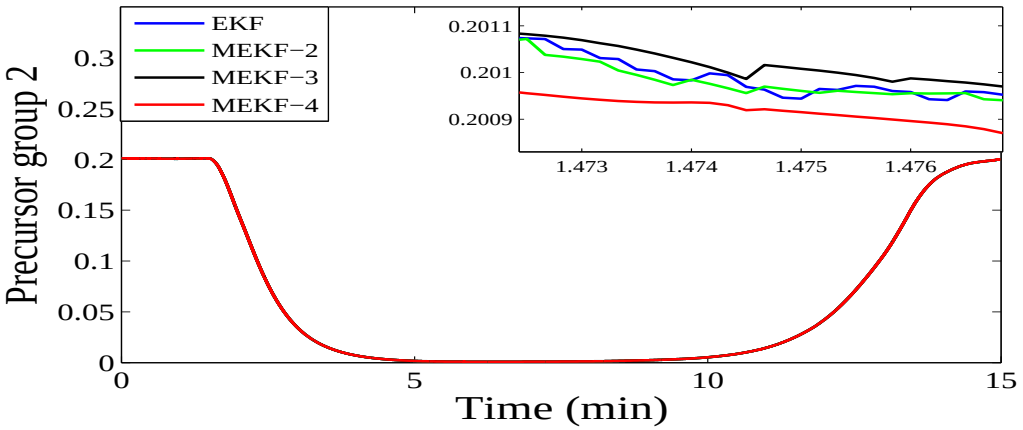

FIGURE 3.28: Delayed neutron precursors' concentration of group 2 for shutdown followed by restart

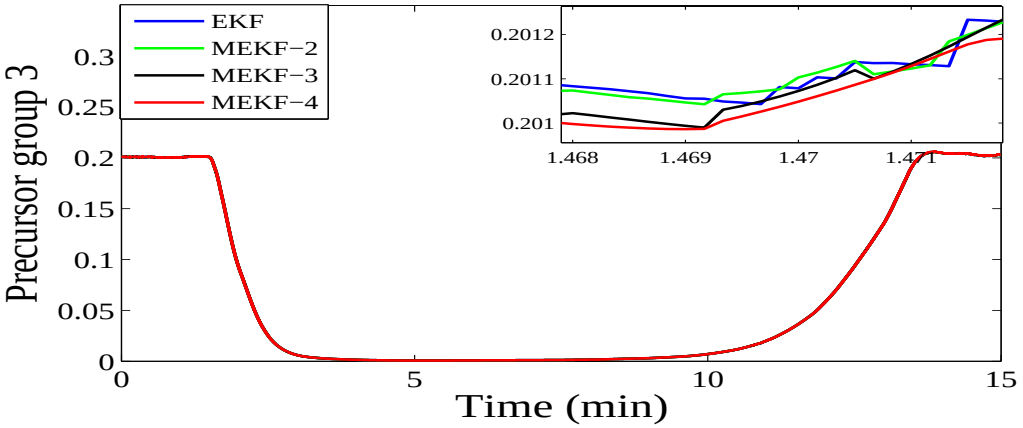

FIGURE 3.29: Delayed neutron precursors' concentration of group 3 for shutdown followed by restart

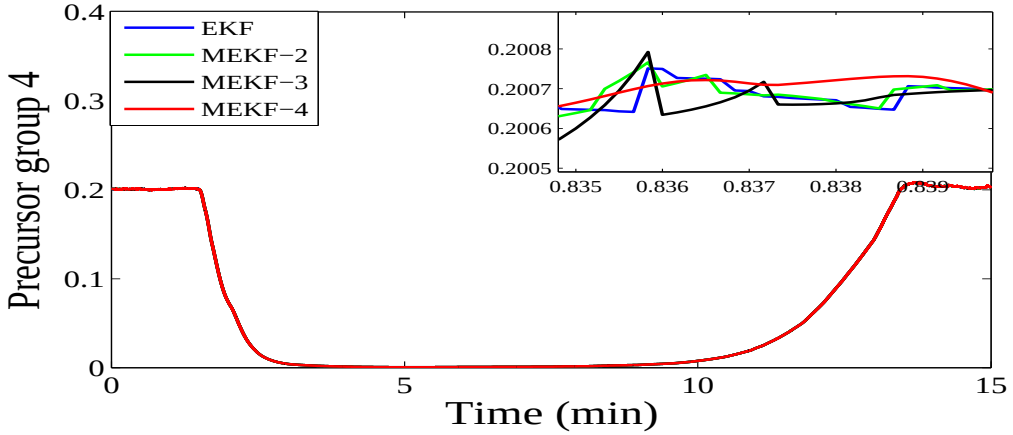

FIGURE 3.30: Delayed neutron precursors' concentration of group 4 for shutdown followed by restart

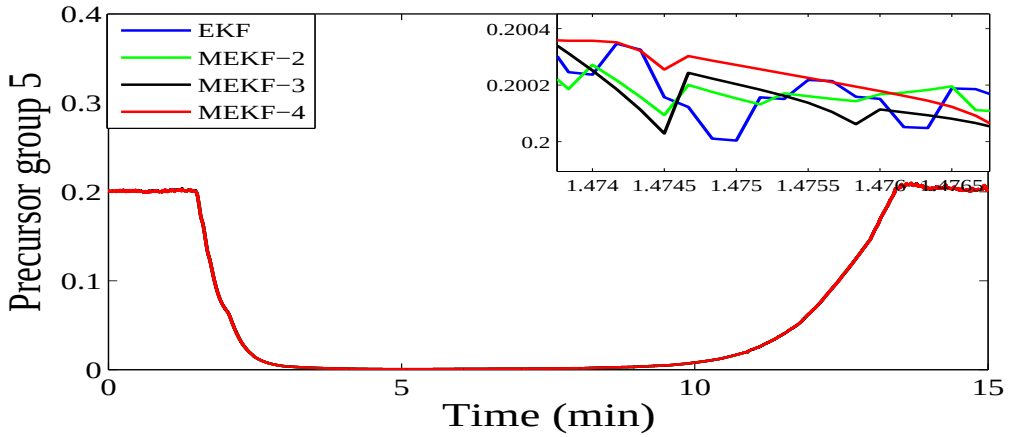

FIGURE 3.31: Delayed neutron precursors' concentration of group 5 for shutdown followed by restart

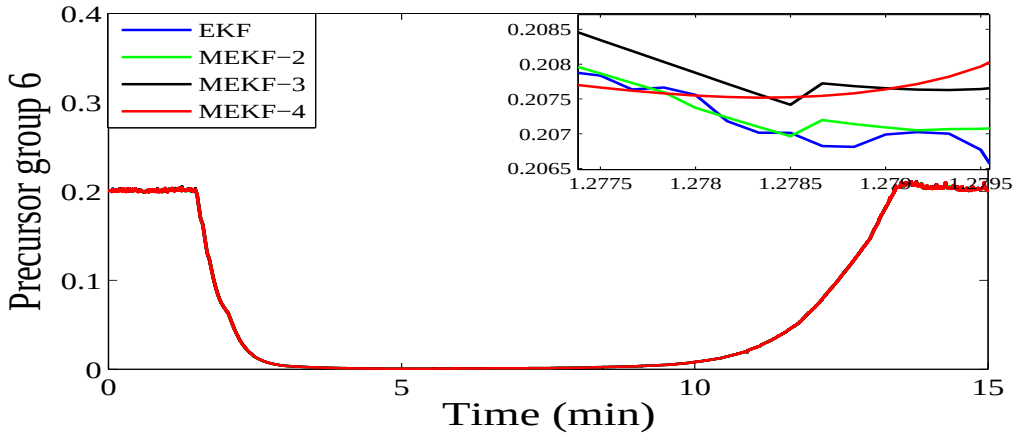

FIGURE 3.32: Delayed neutron precursors' concentration of group 6 for shutdown followed by restart

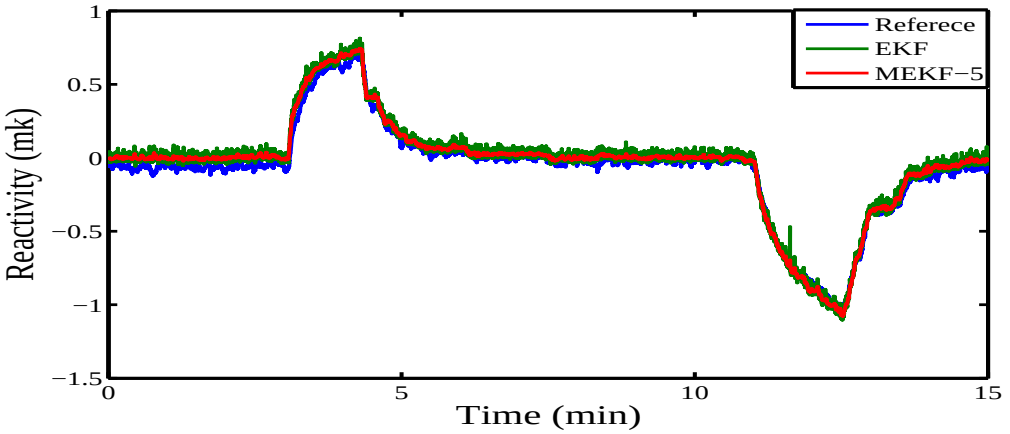

FIGURE 3.33: comparison with reference reactivity for power rise followed by fall

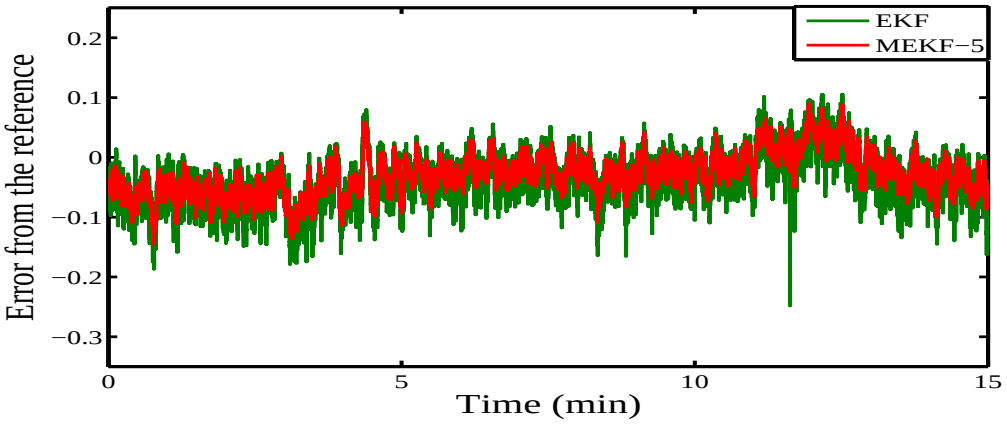

FIGURE 3.34: Error between reference and estimated reactivity for power rise followed by fall

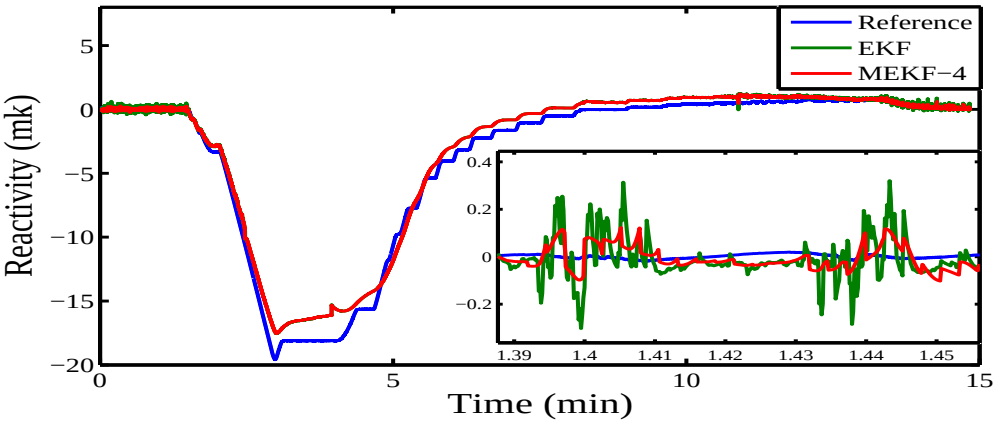

FIGURE 3.35: Comparison with reference reactivity for shutdown followed by restart

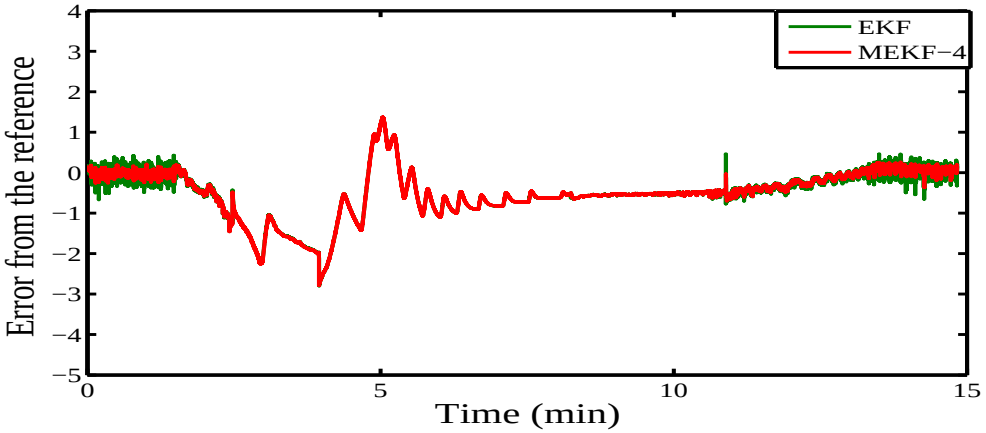

FIGURE 3.36: Error between reference and estimated reactivity for shutdown followed by restart

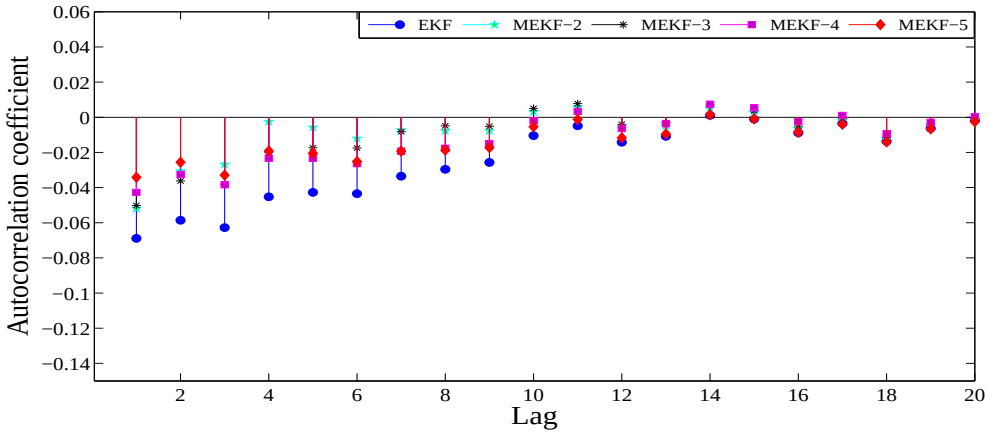

FIGURE 3.37: Auto-correlation function for power rise followed by fall

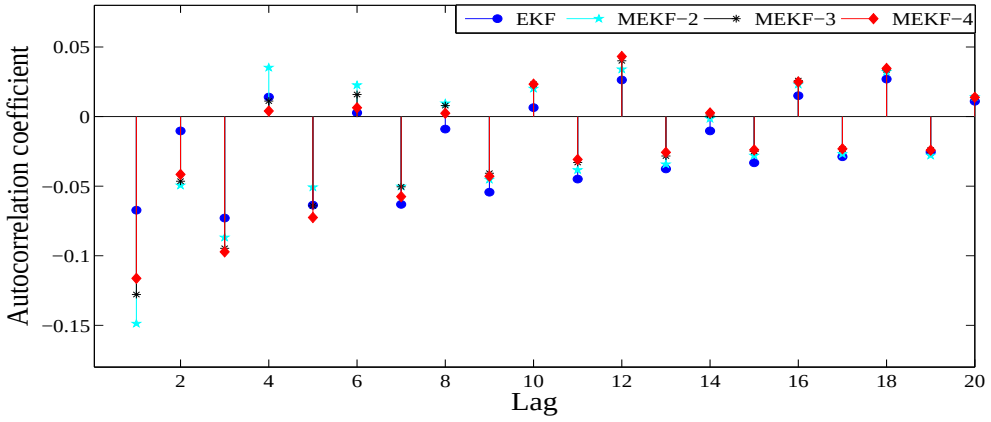

FIGURE 3.38: Auto-correlation function for shutdown followed by restart

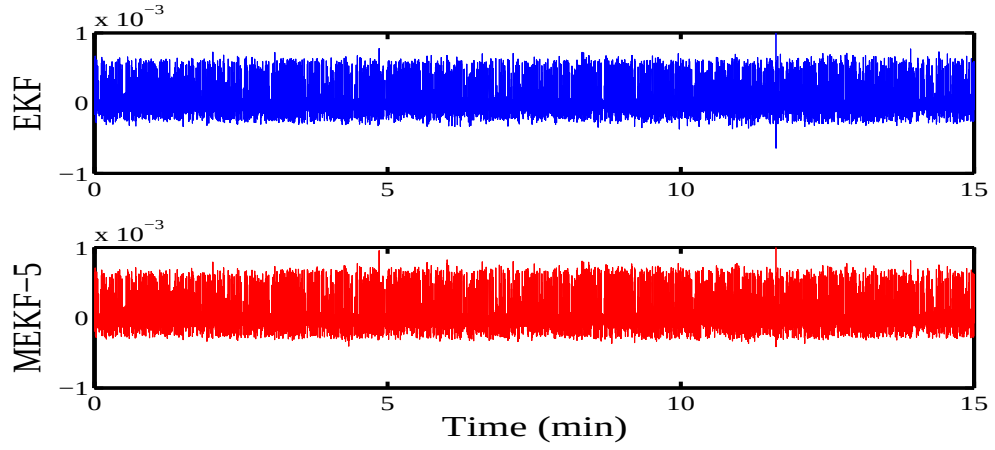

FIGURE 3.39: Error between normalized measured and estimated neutronic power

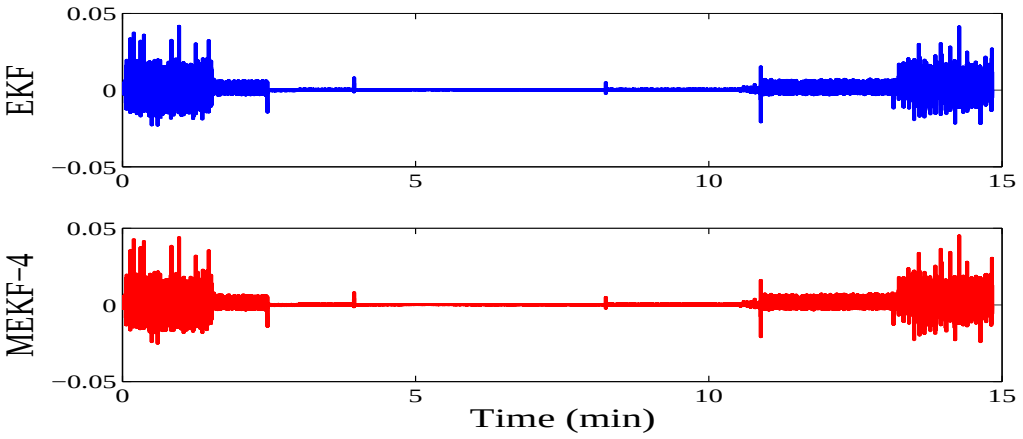

FIGURE 3.40: Error between normalized measured and estimated neutronic power for shutdown followed by restartup transient

Chapter 4

Reactivity and Delayed Neutron Precursors' Concentration Estimation based on Recursive Nonlinear Dynamic Data Reconciliation Technique

The KF and its variants such as EKF, Unscented Kalman Filter (UKF), particle filter, and MEKF reported in the previous Chapter are two step predictive-corrective algorithms. The strength of these algorithms lies in their recursive form, which is extremely important for online deployment. Also, it allows rapid estimation in real-time. The key assumption for employing these techniques is that the covariances of modelling uncertainties and measurement noise are known. Unfortunately, this is generally not satisfied for most of the physical systems.

In the case of the reactivity estimation problem, the covariance of the measurement noise can be taken as a variance of the measurement signal at the steady-state. The covariance of the modeling uncertainties is a critical quantity for the performance of the estimator. It may be estimated with reasonable accuracy by tuning the variance of the innovation sequence at the steady-state condition as per the procedure given in [20]. However, if the reactor power changes significantly from the

steady-state value, such as in the typical shutdown transient, the selected values of the measurement noise variance and covariance of the modeling uncertainties no longer represent the actual quantities. Consequently, estimation results with the EKF may lead to some infeasible values. This problem was observed with the estimation algorithms reported in Chapter 3, i.e., while dealing with the shutdown transients of the Apsara reactor, with suboptimal tuning parameters, **Q** and **R**, EKF, and MEFK rendered infeasible values, i.e., negative values of reactor power and delayed neutron precursors' concentrations. This problem may arise as KF and all its variants cannot take into account constraints on state variables systematically. The adhoc measures like clipping may produce sub-optimal estimates at the best. As these techniques may lead to the infeasible estimates, which is often a cause for the filter's instability [60], a state estimation algorithm which can account for the physical constraints may be expected to perform better than the standard techniques.

This chapter proposes the RNDDR technique to estimate reactivity and delayed neutron precursors' concentrations in the nuclear reactor. The feasibility of the RNDDR method has been validated through step test signal in the presence of measurement noise and experimental power variation data sets collected from a research reactor. In this technique, for each time instant, the prediction step is followed by an update step similar to the EKF. In RNDDR, the predicted state variables and error covariance matrix are obtained as in EKF, while the updated state variables are obtained as the solution of a constrained optimization problem. The RNDDR is identical to EKF if there are no bounds on variables or algebraic constraints. Hence, RNDDR can be viewed as one form of a constrained extended Kalman filter, which is easy for practical implementation.

4.1 Model Description

4.1.1 Neutronic Model

The point kinetics model was introduced in Chapter 3. The same model with an additional source term has been used in this chapter. The point kinetics equations

with source term are given as:

$$\dot{n} = \frac{\rho - \beta}{\ell} n + \sum_{i=1}^{m} \lambda_i C_i + S \tag{4.1}$$

$$\dot{C}_i = \frac{\beta_i}{\ell} n - \lambda_i C_i \quad , \quad i = 1, 2, \ldots, m \tag{4.2}$$

where the notations are same as those introduced in the previous chapters. The source term S, the effective strength of neutron source has been assumed as constant and expressed in term of the initial stable sub-criticality as [45]

$$S = \frac{-\rho_0 n_0}{\ell} \tag{4.3}$$

where n_0 denotes the neutronic power at any subcritical steady-state and ρ_0 denotes the corresponding subcriticality obtained from physics computations. In addition, in order to estimate the reactivity, a reactivity model must be formed which can be embedded into the reactor system as one of its state variables [109]. In order to capture the step and ramp reactivity transients more effectively, instead of using first order random walk model as in Chapter 3, a second order reactivity dynamics are considered as follows:

$$\frac{d\rho}{dt} = \alpha \tag{4.4}$$

$$\frac{d\alpha}{dt} = 0 \tag{4.5}$$

where α is a zero mean noise signal.

4.1.2 State Space Representation of Nonlinear Model

In order to employ EKF for the state estimation, it is necessary to transform the reference model given by the set of equations (4.1), (4.2), (4.4) and (4.5) to a standard state space form as

$$\begin{aligned} \dot{\mathbf{x}} &= f(\mathbf{x}) \\ &= \mathbf{F}_n \mathbf{x} + \mathbf{G}_n \end{aligned} \tag{4.6}$$

in which the state vector $\mathbf{x}$, matrix $\mathbf{F}_n$, and $\mathbf{G}_n$ are defined respectively as

$$\mathbf{x} = \begin{bmatrix} n & C_1 & C_2 & \cdots & C_6 & \rho & \alpha \end{bmatrix}^\top, \tag{4.7}$$

$$\mathbf{F}_n = \begin{bmatrix} \frac{-\beta}{\ell} & \lambda_1 & \lambda_2 & \cdots & \lambda_6 & 0 & 0 \\ \frac{\beta_1}{\ell} & -\lambda_1 & 0 & \cdots & 0 & 0 & 0 \\ \frac{\beta_2}{\ell} & 0 & -\lambda_2 & \cdots & 0 & 0 & 0 \\ \vdots & \vdots & \vdots & \ddots & \vdots & \vdots & \vdots \\ \frac{\beta_6}{\ell} & 0 & 0 & \cdots & -\lambda_6 & 0 & 0 \\ 0 & 0 & 0 & \cdots & 0 & 0 & 1 \\ 0 & 0 & 0 & \cdots & 0 & 0 & 0 \end{bmatrix}. \tag{4.8}$$

$$\mathbf{G}_n = \begin{bmatrix} \frac{\rho n}{\ell} + S & 0 & \cdots & 0 \end{bmatrix}^\top, \tag{4.9}$$

The system model given by (4.6) is nonlinear because of presence of nonlinear term $\frac{\rho n}{\ell} + S$ in $\mathbf{G}_n$.

The Jacobian matrix is given as

$$\mathbf{F} = \frac{\partial f}{\partial \mathbf{x}}(\mathbf{x}). \tag{4.10}$$

Except two elements, rest all the elements of matrix $\mathbf{F}$ are same as those of matrix $\mathbf{F}_n$. Those two elements of matrix $\mathbf{F}$ are

$$\mathbf{F}(1,1) = \frac{\rho - \beta}{\ell} \quad , \quad \mathbf{F}(1,8) = \frac{n}{\ell}. \tag{4.11}$$

By discretizing (4.6) for sampling time interval T_s, we obtain

$$\mathbf{x}[k+1] = \boldsymbol{\phi}_n[k]\mathbf{x}[k] + \boldsymbol{\Gamma}_n[k] + \mathbf{w}[k] \tag{4.12}$$

where $\mathbf{w}$ is the system noise, which is due to the random nature of fission process. It is assumed to be a zero mean white Gaussian noise which is independent of $\mathbf{x}[k]$, with covariance $\mathbf{Q}$. The matrices $\boldsymbol{\phi}_n$ and $\boldsymbol{\Gamma}_n$ are given by

$$\boldsymbol{\phi}_n = e^{\mathbf{F}_n T_s} \tag{4.13}$$

$$\boldsymbol{\Gamma}_n = \int_0^{T_s} e^{\mathbf{F}_n t} \mathbf{G}_n dt. \tag{4.14}$$

Similarly,

$$\boldsymbol{\phi} \;=\; e^{\mathbf{F}T_s}. \tag{4.15}$$

Taking into account an additive noise in the measurement channel, the measurement equation becomes:

$$z[k] \;=\; \mathbf{H}\ \mathbf{x}[k] + v[k] \tag{4.16}$$

where z is measurement variable, i.e. neutronic power, and v is a zero mean white Gaussian noise which is independent of $\mathbf{x}$ and $\mathbf{w}$. Its covariance is assumed to be R. $\mathbf{H}$ is the output matrix corresponding to reactor power n. it is given by

$$\mathbf{H} = \begin{bmatrix} 1 & 0 & 0 & 0 & 0 & 0 & 0 & 0 & 0 \end{bmatrix}^{\top}.$$

4.2 RNDDR algorithm for the state estimation

In this section, the RNDDR [64] algorithm is derived for the estimation of reactivity and delayed neutron precursors' concentration. To be able to apply RNDDR, following assumptions must be satisfied.

- The process is described by a continuous time state space model with discrete sampled measurements.
- The uncertainties in inputs, random fluctuations in unmeasured disturbances, and measurement errors are assumed to be white Gaussian noise processes with known covariance matrices.
- The unmeasured disturbances or parameters may undergo deterministic step changes or drifts. To track these deterministic changes and estimate them, it is assumed that the parameters and unmeasured variables that change are known or specified a priori.

All the above mentioned assumptions are valid for a nuclear reactor.

Similar to the standard EKF, the RNDDR is a two step recursive algorithm. The first step of the algorithm is the prediction step in which estimated states along with error covariance matrix are propagated from the previous time instant using process dynamical equations. This step is same as the prediction step of the standard EKF algorithm. The difference, however lies in the measurement-update step. In which the predicted estimates are corrected by solving a constrained optimization problem as follows.

$$\begin{aligned}\hat{\mathbf{x}}[k] \quad = \quad & \underset{\hat{\mathbf{x}}[k]}{min} \Big[\left(\hat{\mathbf{x}}[k] - \hat{\mathbf{x}}[k/k-1]\right)^{\top} \left(\mathbf{P}[k/k-1]\right)^{-1} \left(\hat{\mathbf{x}}[k] - \hat{\mathbf{x}}[k/k-1]\right) \\ & + \left(z[k] - \mathbf{H}\hat{\mathbf{x}}[k]\right)^{\top} \left(R[k]\right)^{-1} \left(z[k] - \mathbf{H}\hat{\mathbf{x}}[k]\right) \Big] \qquad (4.17) \\ & \text{subject to the constraint } \hat{\mathbf{x}}[k] > \mathbf{x}_L\end{aligned}$$

$\hat{\mathbf{x}}[k]$ is the updated state vector at instant k which is the solution of the constrained optimization problem (4.17). $\mathbf{P}[k]$ is obtained in the same manner as in the standard EKF. The estimates of state variables, namely, the reactor power and delayed neutron precursors' concentrations should be non-negative. Hence the lower bound values imposed on the state variables are $\mathbf{x}_L = \begin{bmatrix} 0 & 0 & 0 & 0 & 0 & 0 & 0 & -\infty & -\infty \end{bmatrix}^{\top}$.

The constrained optimization problem (4.17) can be reformulated as minimization of a quadratic objective function as follows:

$$\hat{x}[k] \quad = \quad \underset{\hat{\mathbf{x}}[k]}{min} \left(\frac{1}{2} \hat{\mathbf{x}}[k]^{\top} \Xi[k] \hat{\mathbf{x}}[k] + g_k^{\top} \hat{\mathbf{x}}[k] \right) \qquad (4.18)$$

subject to the constraint $\hat{\mathbf{x}}[k] > x_L$.

where

$$\Xi[k] = 2 \left[\left(\mathbf{P}[k]\right)^{-1} + \mathbf{H}^{\top} (R_k)^{-1} \mathbf{H} \right]$$

and

$$g[k] = -2 \left[\hat{\mathbf{x}}[k/k-1] (\mathbf{P}[k])^{-1} + z[k] (R[k])^{-1} \mathbf{H} \right].^{\top}$$

This quadratic objective function can be solved using interior-point method. Moreover, the computational efforts required for solving an optimization problem via

interior point method depends on the number of iterations required for convergence. This depends on two key factors, namely, the solver parameters, and a initial condition[110]. Considering the most expensive step of each iteration, the computation complexity would be of $O(n^3)$. However, it is noteworthy that the algorithm is prone to divergence in following cases, namely, (1) a badly conditioned matrix $\Xi[k]$ leading to the numerical ill-conditioning, and (2) a non-restrictive constraint for 4.18. As both of these cases were not applicable in this application, divergence was not observed. The detailed derivation for an optimization problem along with discussion on computational complexity as a function of solver parameters of the algorithm can be found in [111].

As in the standard EKF, for RNDDR algorithm, values of $\mathbf{R}$ and $\mathbf{Q}$ should be ideally selected as values of the variance of measurement noise and system uncertainties respectively. Choosing the right value of the $\mathbf{R}$ and $\mathbf{Q}$ is very important for successful application of RNDDR, however, the optimal selection is quite difficult. If the process-noise covariance matrix, $\mathbf{Q}$ is guessed low, the RNDDR will believe the model excessively and will not use the on-line measurements properly to correct the states. This can lead to poor performance. On the other hand, if the matrix $\mathbf{Q}$ is guessed higher than the actual value, the state estimates will be noisy and uncertain, as this would lead to increased values of the state covariance matrix. Usually, a good initial estimate for R can be obtained from the calibration of the measuring instrument and generally it is assumed to be constant over the data length. Here optimum value for R may be selected as a variance of the steady state measurement at operating power level. For this fixed value of $\mathbf{R}$, value of $\mathbf{Q}$ can be selected as per procedure given in [20].

4.3 Validation of proposed RNDDR technique

The RNDDR-based estimation approach proposed in Section 4.2 is validated in this section with the simulation results using the numerically simulated dataset and experimental data set collected from one of the Indian research reactors. In the first case, data-set is generated by exciting the point kinetics model of the reactor by a known reactivity variation and the power variation thus obtained is contaminated

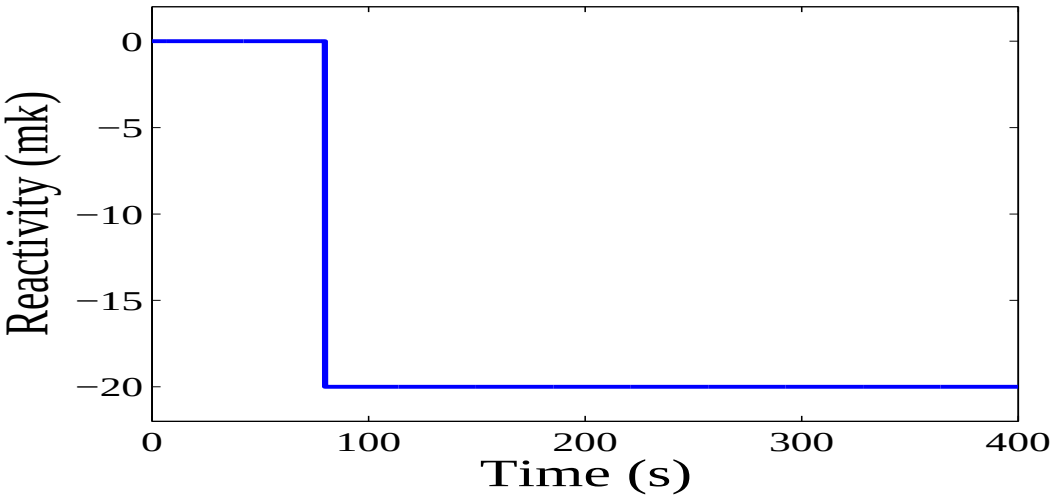

FIGURE 4.1: Assumed reactivity variation

with the noise. This is then used as a measurement signal for the estimation algorithms. In the second case, datasets collected during experiments with one of the Indian research reactors are used for estimation purpose. Details of the datasets followed by corresponding simulation results are presented in the following subsections. In order to assess the performance of the proposed algorithm, the simulation results are compared with the standard EKF technique for both the cases.

4.3.1 Numerical simulation

As mentioned earlier, this data set is generated by using the point kinetics model of the nuclear reactor given by (4.1) and (4.2) by subjecting it to reactivity variation shown in Fig. 4.1. The reactor is assumed to be operating at a full power level and the system is at steady state such that the reactivity is initially zero. Now at $t = 80s$, the reactivity is assumed to drop to $-20mk$ (shown in Fig. 4.1), as in an idealized shutdown transient. The delayed neutron parameters listed in Table 4.1 are used in the simulation.

For the most of the practical dataset, measurement signal is expected to be unbiased and variance of the measurement noise normalized to its nominal value is expected to increase as power level drops down. Therefore, to make the synthetic dataset more realistic, variance of the measurement noise denoted by Ω_k at k^{th}

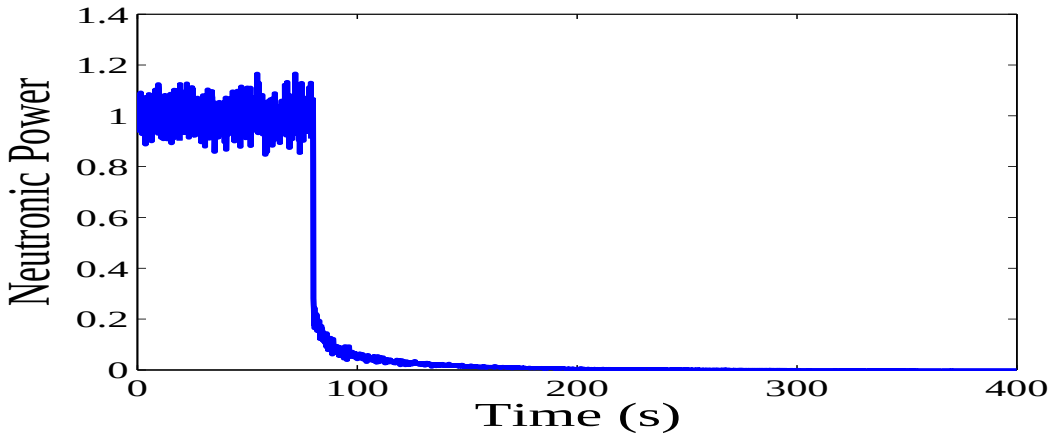

FIGURE 4.2: Neutronic power variation corresponding to reactivity variation shown in 4.1

sampling instant is assumed as a function of power as follows

$$\Omega_k = (a_2 - a_1)(1 - z_k/n_{max}) + a_1 \tag{4.19}$$

where $a_1 = 0.05$, $a_2 = 0.15$, z_k is the measured reactor power at k^{th} sampling instant and n_{max} is the maximum reactor power. Reactor power contaminated by such measurement noise is plotted in Fig. 4.2. As discussed already, this power variation is used as a measurement signal for the estimation algorithms. Estimated variations for neutronic power and reactivity by EKF and RNDDR algorithms with parameters $\mathbf{Q} = [10^{-1}\ 0\ 0\ 0\ 0\ 0\ 0\ 10^{-2}\ 0]$ and $\mathbf{R} = 10^{-2}$ are plotted in Fig. 4.3 and Fig. 4.4 respectively. Values selected for parameters $\mathbf{Q}$ and $\mathbf{R}$ are optimum for the operating point and no physical constraints are violated. Results obtained from both the techniques are overlapping.

For different operating points of the reactor system, the variance of system uncertainty, as well as the measurement noise variance may vary significantly. Hence time varying matrices $\mathbf{Q}$ and $\mathbf{R}$ are required which raise practical implementation concerns. The constant $\mathbf{Q}$ and $\mathbf{R}$ matrices approach are generally preferred for the implementation though not necessarily optimal. However, the selection of suboptimal values might result in the violation of the physical constraints of the system. Considering the suboptimum values of parameters $\mathbf{Q} = [10^{-3}\ 0\ 0\ 0\ 0\ 0\ 0\ 10^{-6}\ 0]$ and $\mathbf{R} = 10^{-1}$, simulation results are obtained to access the efficacy of the proposed techniques. Estimates of the state variables obtained by both the techniques

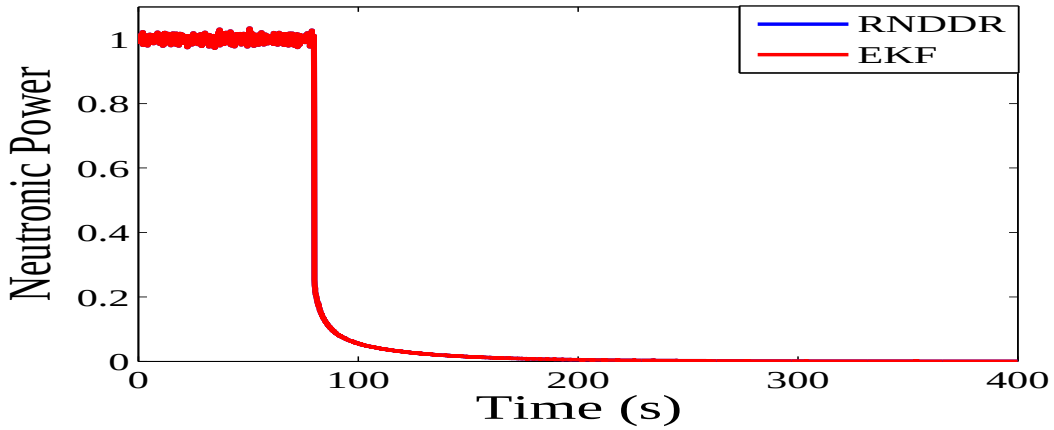

FIGURE 4.3: Estimated power during shutdown transient with optimum **Q** and **R**

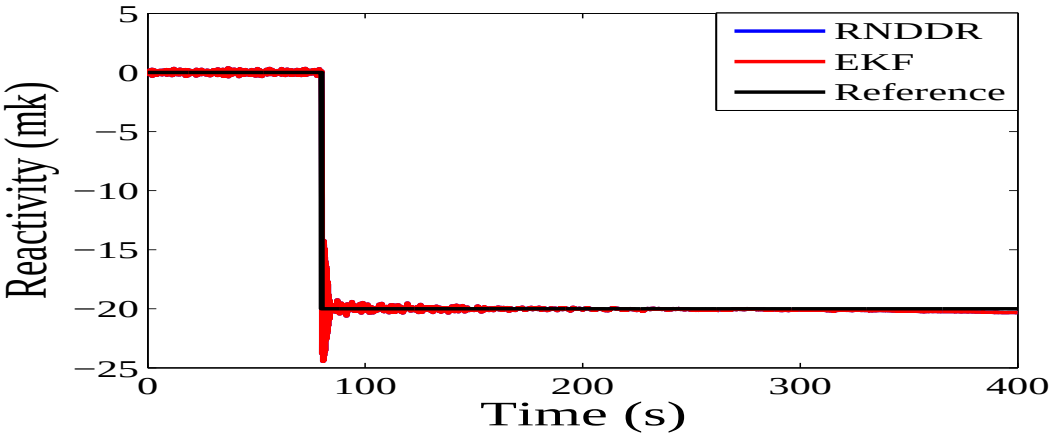

FIGURE 4.4: Estimated reactivity during shutdown transient with optimum **Q** and **R**

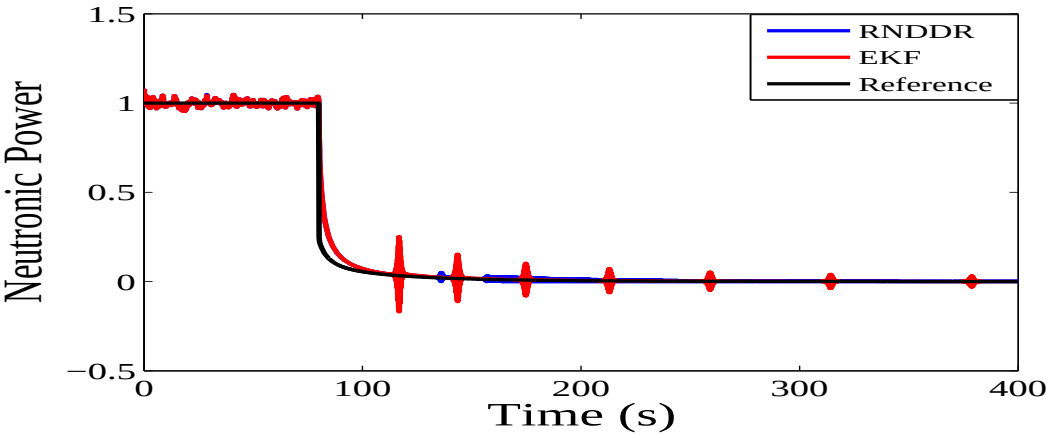

FIGURE 4.5: Estimated neutronic power during shutdown transient with sub-optimum **Q** and **R**

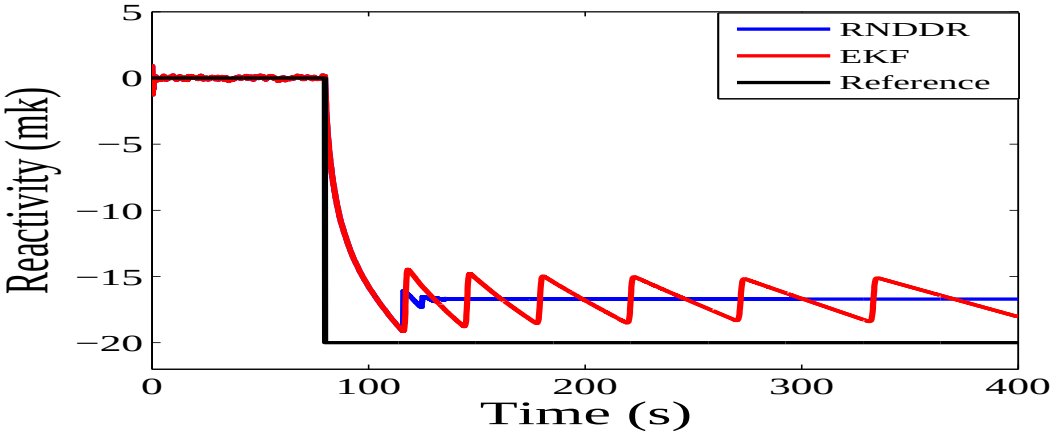

FIGURE 4.6: Estimated reactivity during shutdown transient with suboptimum **Q** and **R**

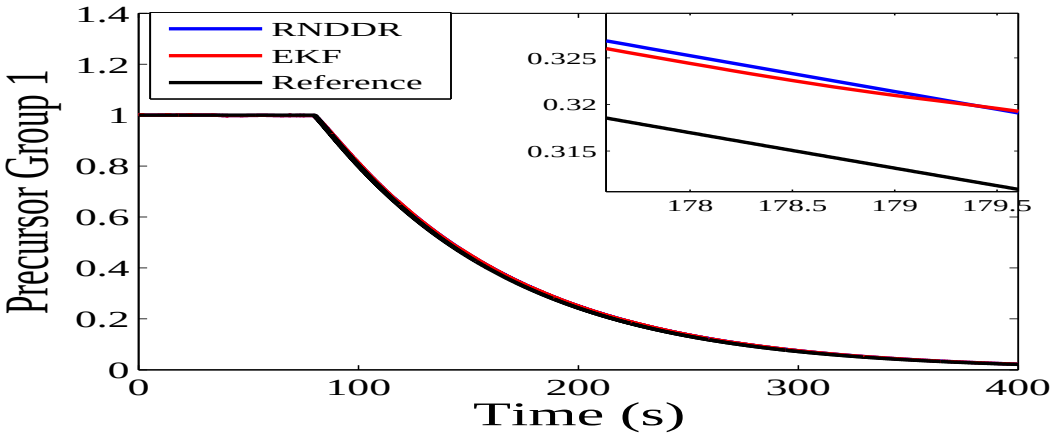

FIGURE 4.7: Estimated delayed neutron precursors' concentration of group 1 during shutdown transient with suboptimum **Q** and **R**

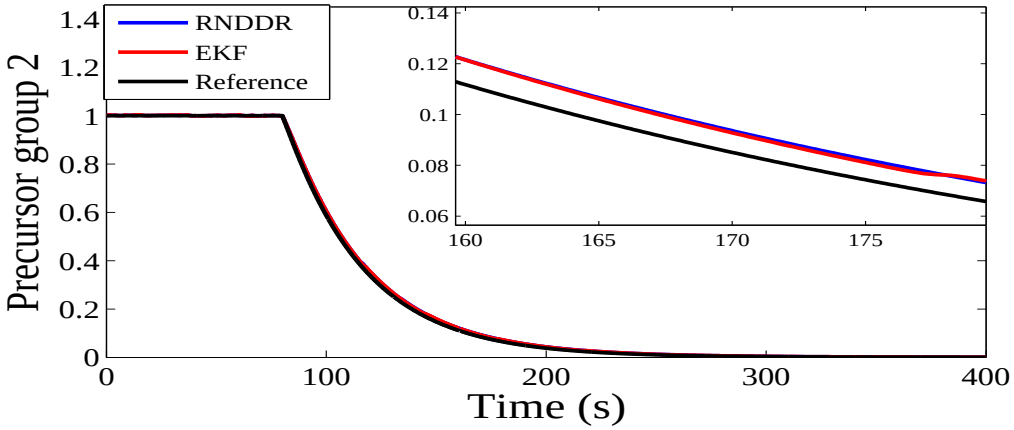

FIGURE 4.8: Estimated delayed neutron precursors' concentration of group 2 during shutdown transient with suboptimum **Q** and **R**

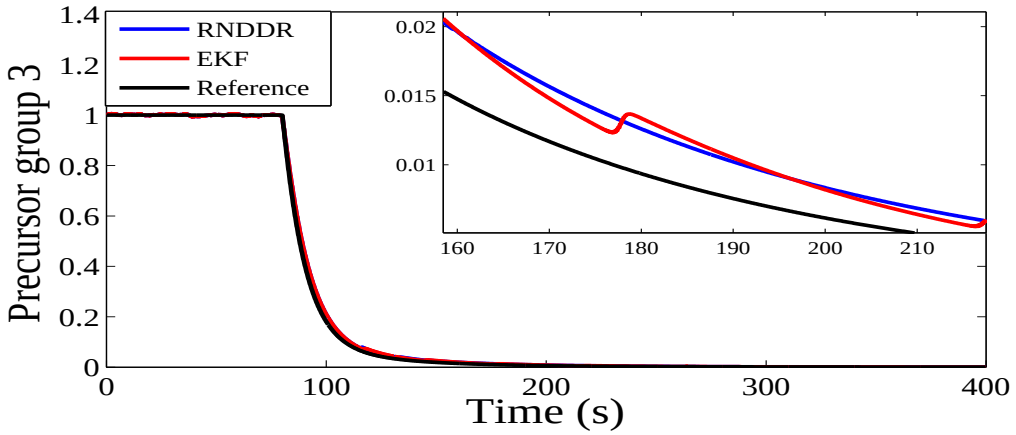

FIGURE 4.9: Estimated delayed neutron precursors' concentration of group 3 during shutdown transient with suboptimum **Q** and **R**

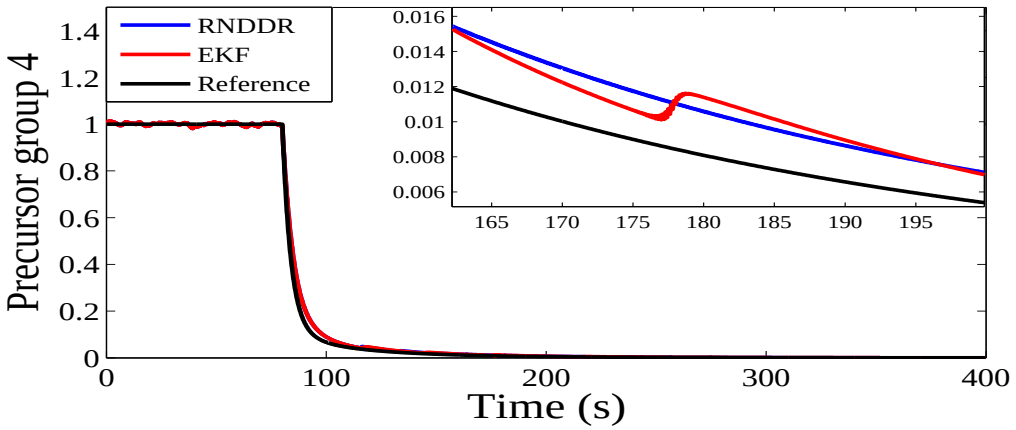

FIGURE 4.10: Estimated delayed neutron precursors' concentration of group 4 during shutdown transient with suboptimum **Q** and **R**

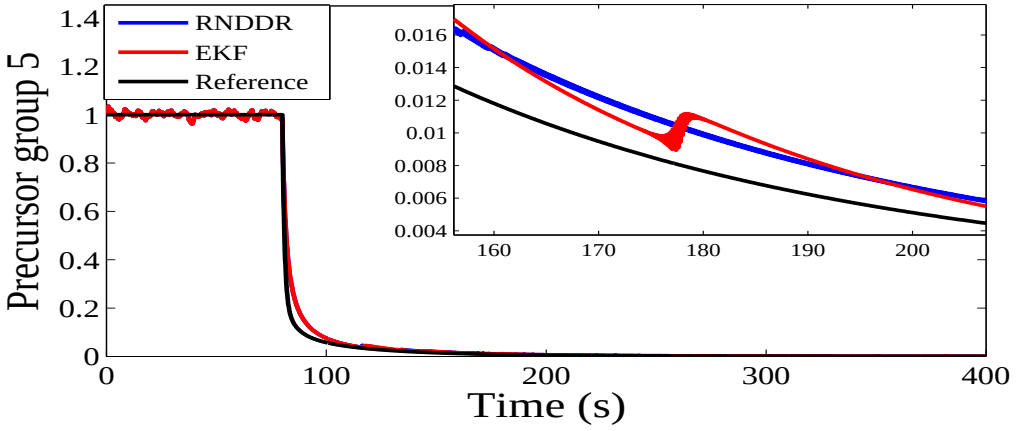

FIGURE 4.11: Estimated delayed neutron precursors' concentration of group 5 during shutdown transient with suboptimum **Q** and **R**

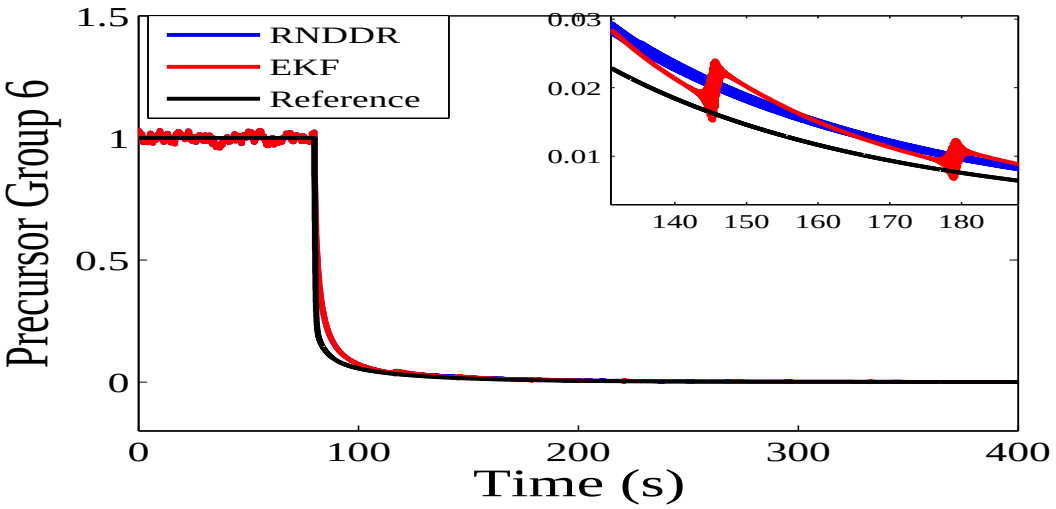

FIGURE 4.12: Estimated delayed neutron precursors' concentration of group 6 during shutdown transient with suboptimum **Q** and **R**

are plotted in Fig. 4.5 through 4.12. In Fig. 4.11 and 4.12, zoomed variation over a small interval is also shown in an inset box. From Fig. 4.5, it is evident that the estimated reactor power from the unconstrained EKF violates the constraints, i.e., the estimated reactor power undergoes a few oscillation around zero and attains negative values for few times. Consequently, the reactivity estimated by EKF as plotted in Fig. 4.6 is inaccurate and it does not converge to the steady state value. While in case of estimated power from the proposed RNDDR technique, constraint violation does not occur and estimated reactivity converges to the steady state value. From the simulation results, it is evident that estimated values for delayed neutron precursors' concentrations, reactor power, and reactivity obtained from EKF seem to fluctuate around the true value, as constraints on the estimated power are violated. In contrast to this, the estimated quantities obtained form RNDDR vary smoothly. Violation of physical constraints and bias in the steady state estimation of reactivity seems to happen with EKF essentially due to suboptimal values for parameters **Q** and **R** as they do not handle Signal to Noise Ratio (SNR) variations for the operating point.

4.3.2 Using experimental data set of FBTR

The efficacy of RNDDR technique for reactivity estimation is evaluated from the experimental data sets collected from a fast breeder test reactor (FBTR)

located at Indira Gandhi Centre for Atomic Research, Kalpakkam, India. The loop type breeder reactor is rated for 40 MW thermal power. Six control rods $(R_A, R_B, \cdots, R_F)$ are employed for power control and shutdown. A detailed specification of the FBTR can be found in [112].

Dataset collected during one of the experiments at FBTR has been considered for the estimation. The delayed neutron data are given in Table 4.2. The reactor is assumed to be in the steady state power level of 240 W and delayed neutron precursors' concentrations are in equilibrium with this power level. At time $t = 100s$, regulating rod R_E is dropped and consequently, reactor undergoes shutdown from its initial power level. The reactor power (normalized to its initial value) undergoes variation as depicted in Fig. 4.13. RNDDR technique derived in the previous section is employed for the state estimation and estimated quantities are compared

TABLE 4.1: Delayed neutron data and source for the reference dataset.

Group Index	$\beta_i\,(\times 10^{-3})$	$\lambda_i\,(s^{-1})$
1	0.248	0.012
2	1.380	0.031
3	1.990	0.118
4	2.627	0.3101
5	1.379	0.9617
6	0.679	2.8930

Prompt neutron generation time, $\ell = 9.2939 \times 10^{-4}$ s
Source term, $S = 6.6$ kW–s

TABLE 4.2: Delayed Neutron Data and Source for the FBTR

Group No.	$\beta_i\,(\times 10^{-4})$	$\lambda_i\,(s^{-1})$
1	0.919	0.0129
2	6.831	0.0311
3	5.469	0.1134
4	8.904	0.3311
5	3.197	1.2600
6	1.077	3.2100

Prompt neutron generation time, $\ell = 7.9 \times 10^{-4}$ s
Source term, $S = 1.5190$ kW–s

with those obtained from the unconstrained EKF technique. Estimated state variables are plotted in Fig. 4.14 through Fig. 4.21. From these plots, it is evident that the estimated reactor power from the unconstrained EKF violates the constraints, i.e., the estimated reactor power undergoes few oscillations around zero and attains negative values for few times. Consequently, the reactivity estimated by EKF as plotted in Fig. 4.14 is inaccurate and it does not converge to the steady state value. While in case of estimated power from the proposed RNDDR technique, no constraint violation is seen to occur and estimated reactivity converges to the steady state value. The estimated delayed neutron precursors' concentration does not violate the constraints with either of the state estimation algorithms but from Fig. 4.20 and Fig. 4.21, it is evident that estimated quantities with the EKF algorithm fluctuate as the constraints on the estimated power are violated. In contrast to this, the RNDDR algorithm renders a smooth variation of the quantities.

4.4 Summary

Reactivity is affected by many properties of a reactor core such as the composition, geometry, temperature, pressure and ability of producing fission neutrons, which is too difficult to be modelled and can be seen as an uncertainty. Therefore, the reactivity estimators must be robust in the presence of disturbances, modeling and parameter uncertainties. Moreover, simple and flexible design characteristics are the other significant properties that an estimator must have from a practical point of view. Reactivity estimation algorithm based on RNDDR technique has been investigated in this chapter. The RNDDR has a simple form, which can induce an easy engineering implementation due to its recursive form. It also handles algebraic constraints and bounds on states and parameters. Constraints can arise due to feasibility considerations i.e., non-negativity of reactor power or delayed neutron precursors' concentration for nuclear reactor system. The results demonstrate that the RNDDR provides reliable and accurate reactivity estimations while there exist constraints on states, parameter uncertainties and noisy measurements. Thus,

RNDDR will increase control flexibility and safety of nuclear reactors. An important aspect of RNDDR when considered for online application is its computational time, which should be carefully addressed, i.e., the platform for implementation should be selected so as to meet the computational time requirement.

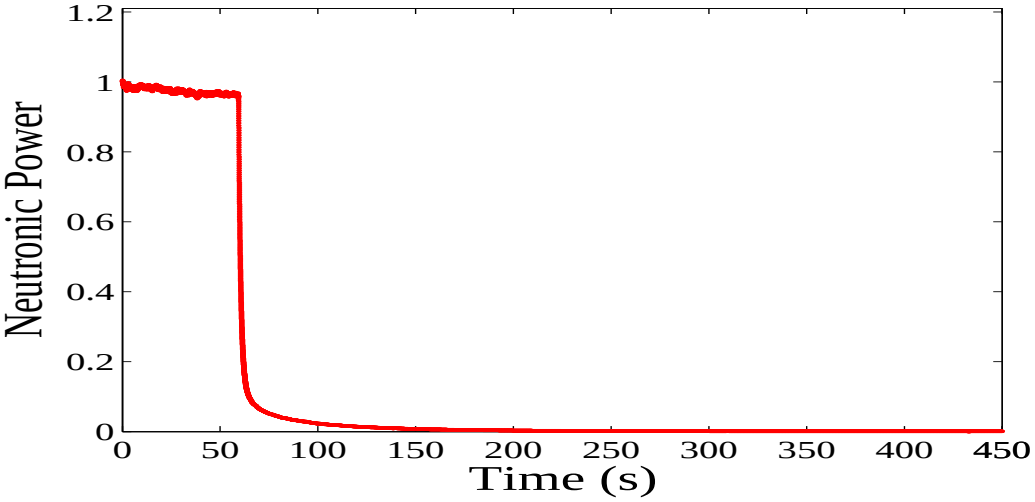

FIGURE 4.13: Power variation from the FBTR during a rod drop experiment

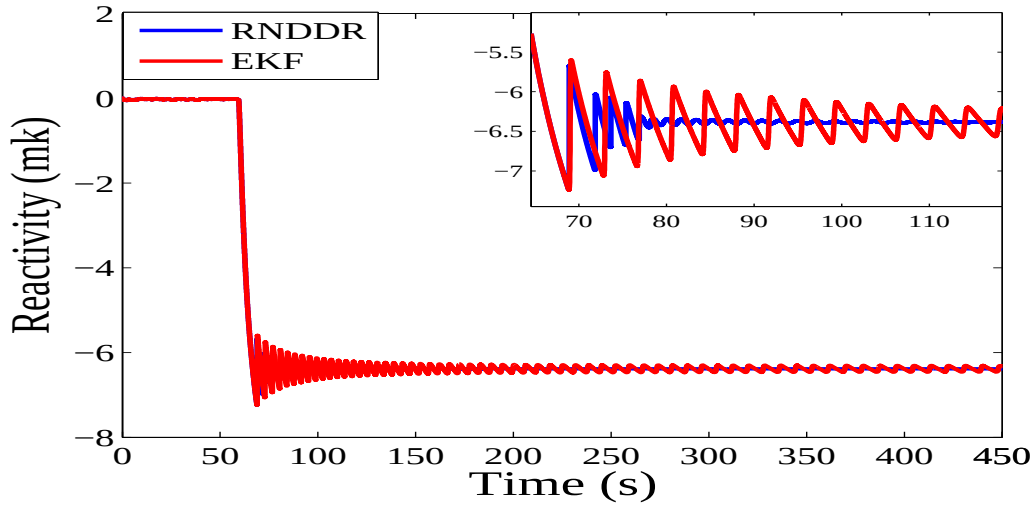

FIGURE 4.14: Estimated reactivity during a rod drop experiment

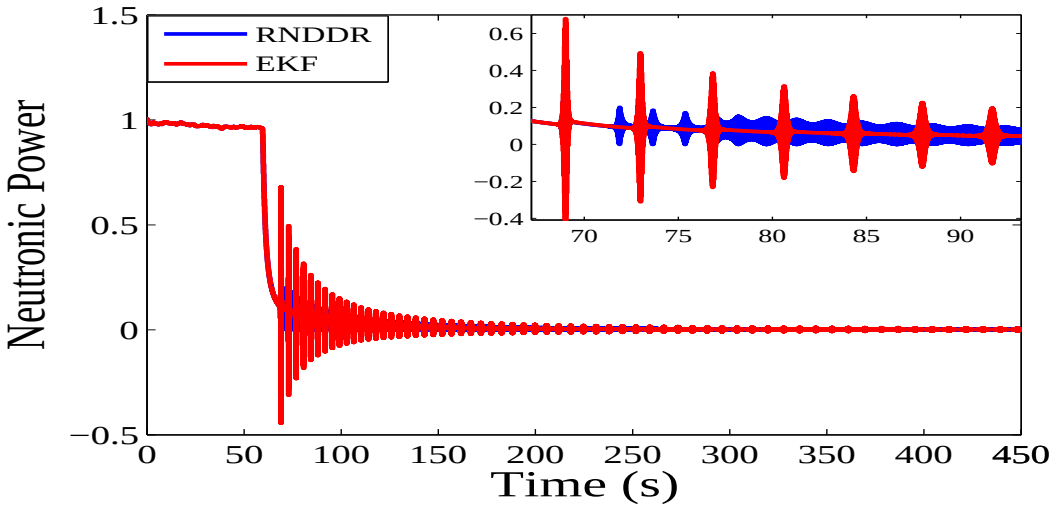

FIGURE 4.15: Estimated neutronic Power during a rod drop experiment

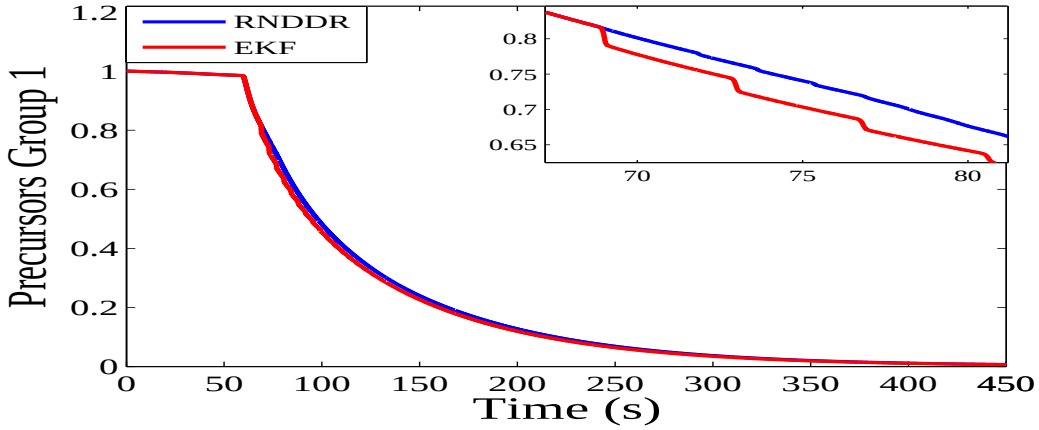

FIGURE 4.16: Estimated delayed neutron precursors' concentration of group 1 during a rod drop experiment

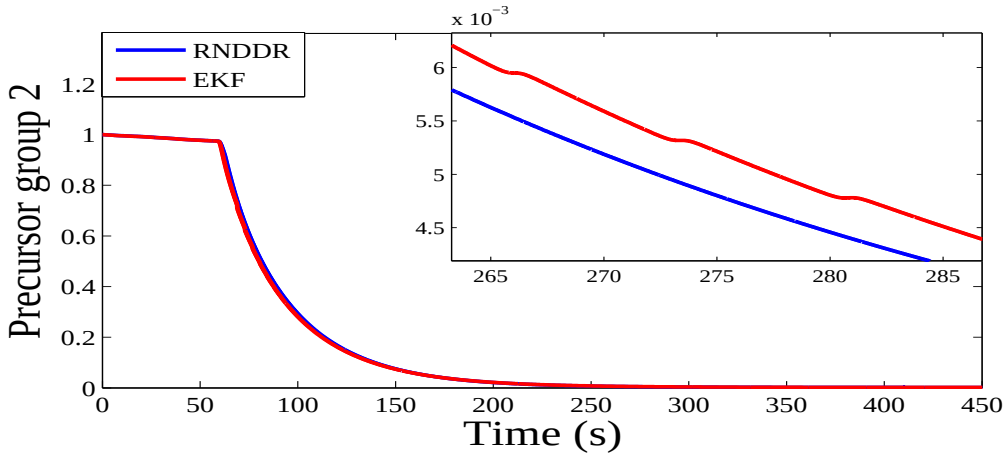

FIGURE 4.17: Estimated delayed neutron precursors' concentration of group 2 during a rod drop experiment

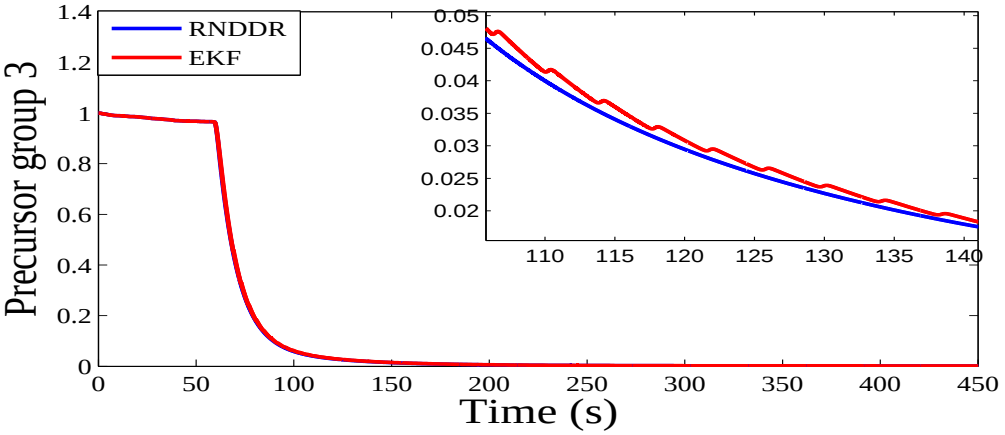

FIGURE 4.18: Estimated delayed neutron precursors' concentration of group 3 during a rod drop experiment

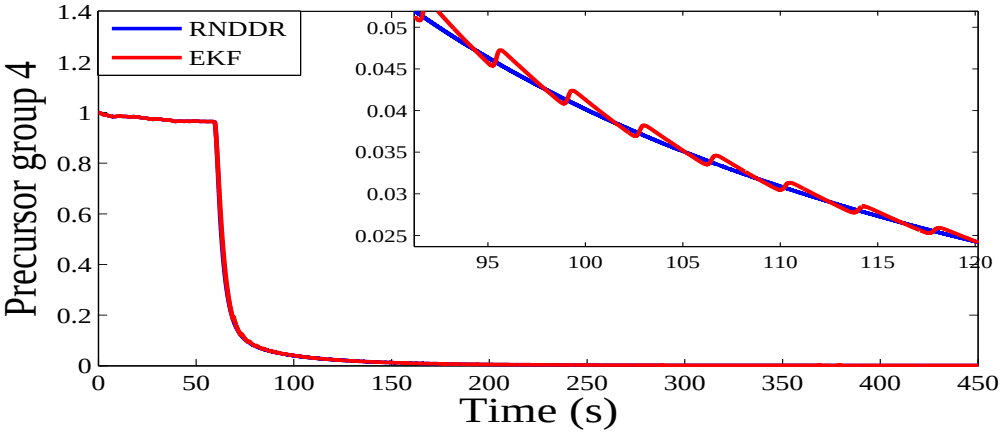

FIGURE 4.19: Estimated delayed neutron precursors' concentration of group 3 during a rod drop experiment

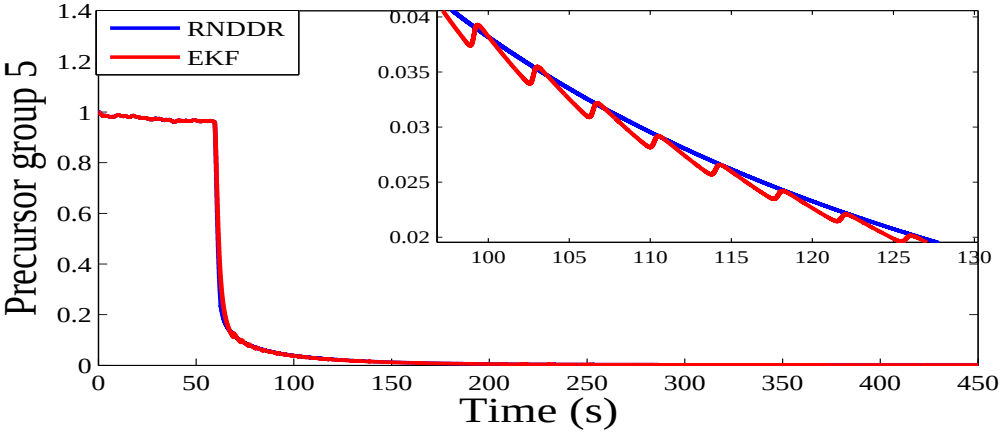

FIGURE 4.20: Estimated delayed neutron precursors' concentration of group 3 during a rod drop experiment

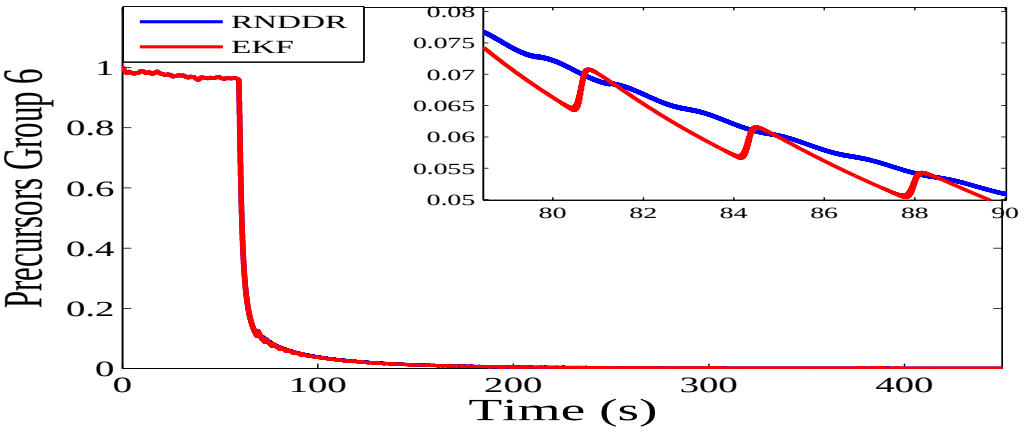

FIGURE 4.21: Estimated delayed neutron precursors' concentration of group 6 during a rod drop experiment

Chapter 5

Estimation of fuel and the coolant temperatures of the nuclear reactor using stationary wavelet transform based multi-scale EKF

In Chapter 3, a multi-scale EKF technique for a class of nonlinear autonomous systems was presented. There, a multi-scale model structure was formulated by projecting the system states on wavelet projection space by discrete wavelet transform (DWT). Although the proposed technique outperforms the standard EKF technique, there were two constraints in the formulation, as given below:

1. Estimation is feasible only for the class of autonomous systems.
2. The estimation is non-causal and has to be performed in a semi-online manner.

The above mentioned constraints do not pose any serious difficulty for the reactivity estimation problem as the reactivity, an input to the system is modeled as an unknown state. However, if the forced nonlinear model of the nuclear reactor is considered, the state estimation with the proposed technique will not be feasible. Hence, in this chapter a multi-scale EKF algorithm based on the stationary

wavelet transform is formulated that can handle both of these constraints. The technique proposed in this chapter is also based on and preserves the merits of the EKF and at the same time application of the stationary wavelet transform captures the multi-scale nature of the system. The description of the reactor model followed by the proposed techniques and simulation results are presented in the subsequent sections.

5.1 Simplified mathematical model of PHWR

In this section, reduced order dynamic model with internal reactivity feedback due to core temperature variations for 540 MWe Indian PHWR is presented [113]

5.1.1 Reactor core and thermal hydraulic model

As discussed in the previous chapters, the dynamic model for the nuclear reactor is usually represented by the point kinetics equations. It represents variations of neutronic power along with six groups of delayed neutron precursors' concentrations with respect to time.

In this chapter, however, reactivity feedbacks due to variation in fuel and coolant temperatures are also considered. Moreover, as dealing with higher order model involving the dynamics of the six group of delayed neutron precursors' concentrations along with the dynamics internal reactivity feedback could be very complicated, one equivalent group of the delayed neutron precursors' concentration has been considered. Such simplification is very commonly adopted in the reactor control literature [14]. The dynamics of the system under consideration are represented as follows:

$$\dot{n} = \left(\frac{\rho_T - \beta}{l}\right) n + \frac{\beta}{l} C, \tag{5.1}$$

$$\dot{C} = \lambda P - \lambda C, \tag{5.2}$$

$$\rho_T = \rho_U + \rho_F + \rho_C, \tag{5.3}$$

where n and C respectively denote the reactor power and the one effective group delayed neutron precursors' concentration normalized to the steady state values. β and λ denote fraction of delayed neutrons and decay constant of the delayed neutron precursors. l is prompt neutron lifetime. ρ_U is the external reactivity variation contributed by the control devices maneuvered by the reactor regulating system. ρ_F and ρ_C are internal reactivity feedbacks due to variation in fuel and coolant temperatures respectively. Net reactivity variation is denoted by ρ_T as a combined effect of ρ_U, ρ_F and ρ_C. The internal reactivity feedbacks i.e., ρ_F and ρ_C can be represented as follows [114]

$$\rho_F = \alpha_0^F + \alpha_1^F \theta_F + \alpha_2^F \theta_F^2 \tag{5.4}$$

$$\rho_C = \alpha_0^C + \alpha_1^C \theta_C. \tag{5.5}$$

where θ_F and θ_C denote average fuel temperature and average coolant temperatures respectively. α_i^F, $i = 0, 1, 2$ and α_j^C, $j = 0, 1$ denotes proportionality constants for reactivity feedback due to average fuel temperature and average coolant temperatures respectively.

5.1.2 Core Thermal Hydraulics

The fission heat produced in the reactor core is transferred to coolant by the means of conduction and convection. Heat transfer rates are usually modelled by Fourier's law of conduction and Newton's law of cooling. A lumped model describing the core-thermal hydraulic behaviour of the system can be described as follows.

$$\dot{\theta}_F = K_1 n - \frac{\theta_F - \theta_C}{\tau_F} \tag{5.6}$$

$$\dot{\theta}_C = K_2(\theta_F - \theta_C) - 2K_3(\theta_C - \theta_1) \tag{5.7}$$

where θ_1 is coolant inlet temperature, and τ_F is the time constant describing thermal lag in the fuel. K_1 is the proportionality constant with respect to reactor power. K_2 is the proportionality constant for the temperature difference between fuel and coolant. K_3 is the proportionality constant which characterizes the decrease in coolant temperature with respect to difference between average coolant temperature and coolant inlet temperature. The dynamics for variation of Xenon and Iodine concentrations are not considered as those are insignificant for the short duration transients involving total power variation.

5.1.3 State Space Representation of the System

The system model described by (5.1) - (5.7) can be written in the state space form as follows:

$$\begin{aligned} \dot{\mathbf{x}} &= f(\mathbf{x}, \mathbf{u}) \\ &= \mathbf{F}_n \mathbf{x} + \mathbf{G}_n \mathbf{u} \end{aligned} \tag{5.8}$$

where $\mathbf{x} = [n \ C \ \theta_F \ \theta_C]^\top$ is the state vector. The control input $\mathbf{u} = [\rho_U \ \theta_1]$ comprises of the external reactivity variation obtained from the reactivity devices and coolant inlet temperature. Elements of the matrices $\mathbf{F}_n$ and $\mathbf{G}_n$ can be given as follows

$$\mathbf{F}_n = \begin{bmatrix} \frac{\rho_F + \rho_C - \beta}{l} & \frac{\beta}{l} & 0 & 0 \\ \lambda & -\lambda & 0 & 0 \\ K_1 & 0 & \frac{-1}{\tau_F} & \frac{1}{\tau_F} \\ 0 & 0 & K_2 & -(K_2 + 2K_3) \end{bmatrix} \tag{5.9}$$

$$\mathbf{G}_n = \begin{bmatrix} P/l & 0 & 0 & 0 \\ 0 & 0 & 0 & 2K_3 \end{bmatrix}^\top . \tag{5.10}$$

The system described by (5.8) is a nonlinear system due to presence of the state variable P in a state vector as well as in the input distribution matrix G_n. The

Jacobian of the system can be given as follows

$$\mathbf{F} = \frac{\delta f(\mathbf{x}, \mathbf{u})}{\delta \mathbf{x}} \tag{5.11}$$

where the elements of $\mathbf{F}$ matrix would be same as those of $\mathbf{F}_n$ except the element $\mathbf{F}(1,1)$ which is given as $\mathbf{F}(1,1) = \frac{\rho_U + \rho_F + \rho_C - \beta}{l}$.

If sampling is carried out at uniform time-interval of T_s seconds, a set of difference equations corresponding to the system (5.8) will be obtained as given by

$$\mathbf{x}[k+1] = \mathbf{\Phi}_n[k]\mathbf{x}[k] + \mathbf{\Gamma}_n\mathbf{u}[k] + \mathbf{w}[k] \tag{5.12}$$

where $\mathbf{w}$ is the modeling uncertainty of the stochastic nuclear reactor system. It is assumed to be white and Gaussian distributed with zero mean and covariance $\mathbf{Q}$. Matrices $\mathbf{\Phi}_n$, $\mathbf{\Gamma}_n$, and $\mathbf{\Phi}$ in the discrete domain can be written as follows

$$\mathbf{\Phi}_n[k] = e^{\mathbf{F}_n(kT_s)} \tag{5.13}$$

$$\mathbf{\Gamma}_n = \int_0^{T_s} e^{\mathbf{F}_n T_s}\mathbf{G}_n dt \tag{5.14}$$

$$\mathbf{\Phi}[k] = e^{\mathbf{F}(kT_s)} \tag{5.15}$$

The measurement process is governed by the following equation

$$\mathbf{z}[k] = \mathbf{H}\mathbf{x}[k] + \mathbf{v}[k] \tag{5.16}$$

where $\mathbf{v}$ is an additive measurement noise. It is assumed to be white and uncorrelated to system uncertainty $\mathbf{w}$. Further, it is assumed to be white and Gaussian distributed with zero mean and covariance $\mathbf{R}$. The output matrix corresponding to measured reactor power is given by

$$\mathbf{H} = \begin{bmatrix} 1 & 0 & 0 & 0 \end{bmatrix}. \tag{5.17}$$

5.2 Brief introduction to Stationary wavelet transform

Stationary wavelet transform is a shift invariant wavelet transform. The shift invariance property of SWT makes it suitable for various applications like fault detection, denoising, and pattern recognition. In the following section, it is demonstrated that SWT can be employed to derive the standard EKF algorithm by using the same state space model at each scale. Like DWT, SWT algorithm can also be implemented by wavelet filter bank with two key differences, (1) The outputs of the high pass and low pass filter are not decimated, and (2) Filters are dialated at scale depth n by inserting $2^n - 1$ zeros between coefficients. Implementation of SWT with the filter bank is fairly simple as shown in Fig. 5.1. To illustrate SWT based multiscale analysis, consider the discrete time-series signal $S_j = [s_j(1)\ \ s_j(2)\ \ \cdots\ \ s_j(n)]$ at any arbitrary scale j. The signal is applied to the high pass filter (HPF) and low pass filter (LPF) branch of the analysis side. Assume that HPF and LPF of analysis side standard DWT has length r with respective coefficients given by $h_a = [h_a^1\ \ h_a^2\ \ \cdots\ \ h_a^r]$ and $g_a = [g_a^1\ \ g_a^2\ \ \cdots\ \ g_a^r]$. If the signal is required to be projected on scale $j+1$, the corresponding filters for SWT can be obtained by upsampling the standard filters by a factor of 2. Therefore, length of the filters would be $p = 2r$. The same can be written as follows

$$\begin{aligned} \bar{h}_a &= [0\ \ h_a^1\ \ 0\ \ \cdots\ \ h_a^r] \qquad (5.18)\\ &= [\bar{h}_a^1\ \ \bar{h}_a^2\ \ \cdots\ \ \bar{h}_a^p] \\ \bar{g}^a &= [0\ \ g_a^1\ \ 0\ \ \cdots\ \ g_a^r] \qquad (5.19)\\ &= [\bar{g}_a^1\ \ \bar{g}_a^2\ \ \cdots\ \ \bar{g}_a^p] \end{aligned}$$

where $\bar{h}_a$ and $\bar{g}_a$ respectively denote analysis HPF and LPF of SWT. The approximation and detail sequences at scale $j+1$ can be written as follows

$$s_{j+1}(k) = \bar{h}_a^1 s_j(k-p+1) + \bar{h}_a^2 s_j(k-p+2) + \cdots + \bar{h}_a^p s_j(k)$$

$$d_{j+1}(k) = \bar{g}_a^1 s_j(k-p+1) + \bar{g}_a^2 s_j(k-p+2) + \cdots + \bar{g}_a^p s_j(k)$$

It can be noted that the approximation and detail sequences obtained by SWT turn out to be of the same length as that of the input sequence. The analyzed signals at scale $j+1$ can be synthesized back at scale j as follows. Implementation of the synthesis filter can be done by the $\bar{h}^s$ and $\bar{g}^s$ of synthesis filter bank as shown in Fig. 5.1.

$$\begin{aligned} s_j(k) &= \bar{h}_s^1 s_{j+1}(k-p+1) + \cdots + \bar{h}_s^p s_{j+1}(k) + & (5.20)\\ &\quad \bar{g}_s^1 d_{j+1}(k-p+1) + \cdots + \bar{g}_s^p d_{j+1}(k). & (5.21) \end{aligned}$$

Choice for the wavelet filters usually depends on the time frequency localization property required for the particular application. In this application, the Haar wavelet is used for simplicity.

5.3 State space modeling and estimation in multiscale framework

In this section, state space model of the system relating the scaled approximation and details of the signals has been derived. The model so derived is then used for estimation purpose. Assume that the system and measurement process are at scale $j = 0$. The approximation of the state vector at scale $j = 1$ can be obtained by projecting the sequence of the state vector on to the SWT decomposition. Assume that the system model (5.12) is at scale $j = 0$ and it is rewritten as follows

$$\mathbf{x}_j[k+1] = \mathbf{\Phi}_n[k]\mathbf{x}_j[k] + \mathbf{\Gamma}_n\mathbf{u}_j[k] + \mathbf{w}_j[k]. \tag{5.22}$$

Using (5.20), approximation coefficient at the next scale can be written as follows

$$\mathbf{x}_{j+1}[k+1] = \bar{h}_a^1\mathbf{x}_j[k-p+2] + \bar{h}_a^2\mathbf{x}_j[k-p+3] + \cdots + \bar{h}_a^p\mathbf{x}_j[k+1] \tag{5.23}$$

Considering that $\mathbf{\Phi}_n$ and $\mathbf{\Gamma}_n$ remain constant for the interval-length of the wavelet moving window, using (5.12) the above equation can be rewritten as

$$\begin{aligned}
\mathbf{x}_{j+1}[k+1] &= \bar{h}_a^1(\mathbf{\Phi}_n\mathbf{x}_j[k-p+1] + \Gamma_n\mathbf{u}_j[k-p+1] + \mathbf{w}_j[k-p+1]) + \\
&\quad \bar{h}_a^2(\mathbf{\Phi}_n\mathbf{x}_j[k-p+2] + \mathbf{\Gamma}_n\mathbf{u}_j[k-p+2] + \mathbf{w}_j[k-p+2]) \\
&\quad + \cdots + \bar{h}_a^p(\Phi_n\mathbf{x}_j[k] + \ \Gamma_n\mathbf{u}_j[k] + \mathbf{w}_j[k]) \\
&= \mathbf{\Phi}_n(\bar{h}_a^1\mathbf{x}_j[k-p+1] + \bar{h}_a^2\mathbf{x}_j[k-p+2] + \cdots + \bar{h}_a^p\mathbf{x}_j[k]) \\
&\quad + \mathbf{\Gamma}(\bar{h}_a^1\mathbf{u}_j[k-p+1] + \bar{h}_a^2\mathbf{u}_j[k-p+2] + \cdots + \bar{h}_a^p\mathbf{u}_j[k]) \\
&\quad + (\bar{h}_a^1\mathbf{w}_j[k-p+1] + \bar{h}_a^2\mathbf{w}_j[k-p+2] + \cdots + \bar{h}_a^p\mathbf{w}_j[k]) \\
&= \mathbf{\Phi}_n\mathbf{x}_{j+1}[k] + \mathbf{\Gamma}_{\boldsymbol{n}}\mathbf{u}_{j+1}[k] + \mathbf{w}_{j+1}[k] \qquad (5.24)
\end{aligned}$$

Similarly, the measurement model at scale $j+1$ can be obtained as

$$\mathbf{z}_{j+1}[k] = \mathbf{H}\mathbf{x}_{j+1}[k] + \mathbf{v}_{j+1}[k]. \qquad (5.25)$$

It can be noted that the state space model and measurement model given by (5.24) and (5.25) are derived by approximation coefficients at arbitrary scale j. However, a similar model structure can also be formed by using detail coefficients at any arbitrary scale. Further, it can be noted that the system derived at scale $j+1$ has the same form as that of the system in time domain i.e., at scale $j=0$. Therefore, models derived at any scales can be subjected to the standard EKF algorithm [20]. Therefore, the EKF algorithm described in Appendix B, can be applied to the models derived at any scale. The method of application of EKF does not change with scale. The EKF estimates are simultaneously calculated with the detail coefficients upto the scale j. In this way, the approximation and detail coefficients for the sequence of state variables are estimated upto arbitrary scale.

5.3.1 Multiscale Extended Kalman Filtering

In this subsection, the EKF algorithm is derived for the system model derived upto the arbitrary scale depth m and the algorithm is denoted as MEKF-m for the subsequent sections. It consists of the two recursive steps, i.e., state prediction and state correction. In the prediction step, the current estimate of the state vector is used alongwith the system model to estimate the next state vector. While in the correction step, the measurement data are fused with the predicted estimate of the state vector such that the covariance of the error becomes minimum. At any scale j, the wavelet transformed coefficients are used as the state vectors of the standard EKF algorithm and estimates of the coefficients at each scale are derived by using the EKF algorithm described in Appendix B. Subsequently, the estimated detail coefficients are soft thresholded. For this purpose, the universal threshold is considered as follows [115]

$$T = \sigma\sqrt{2\log n} \tag{5.26}$$

where σ is the absolute median deviation of the detail coefficients and n is the size of the data length. Sequence of state variables thus obtained are subjected to corresponding wavelet synthesis filters. Further, thresholded detail coefficients along with the approximation coefficients are synthesized with the synthesis filter bank. In this way, the estimated sequence of the state variable is reconstructed back into the original space. The block diagram representation for state estimation with MEKF-2 is shown in Fig. 5.1.

5.4 Simulation Results

The efficacy of proposed MEKF algorithm is now evaluated using simulations. The proposed technique is applied to the nuclear reactor system given by (5.1)-(5.7). The delayed neutrons parameters for PHWR are mentioned in Table 5.1. The system has been subjected to the external reactivity variation as shown in Fig. 5.2. It has been chosen such that the net reactivity, i.e. the reactivity after considering

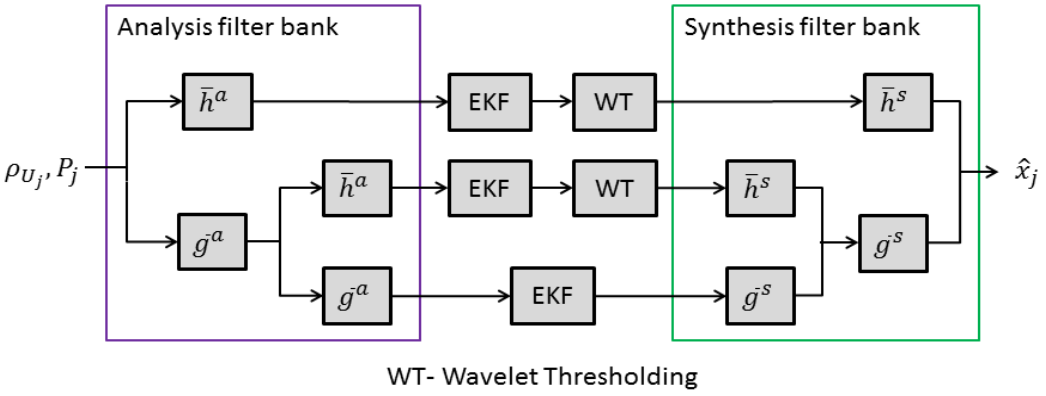

FIGURE 5.1: Block diagram representation for MEKF-2

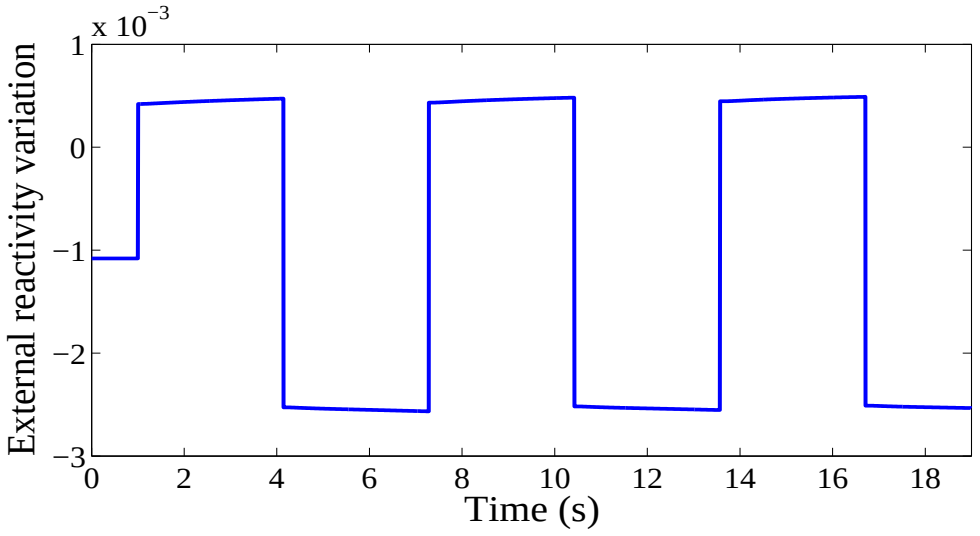

FIGURE 5.2: Reactivity variation by regulating devices

thermal feedbacks varies as shown in Fig. 5.3. The coolant inlet temperature is considered to be at 260^0C and is assumed to remain constant throughout the observation. The corresponding power variation is plotted in Fig. 5.4. Random noise with zero mean and variance equivalent to 5% of nominal value has been added to reactor power. The power variation thus obtained has been considered as a measurement signal and it plotted in a Fig. 5.5. The sampling interval of $5ms$ has been considered throughout the simulations. Initially, the reactor is assumed to be in a steady-state at 1 unit power and delayed neutron precursors' concentrations are in equilibrium corresponding to this power level.

Estimation of the state variables using EKF and MEFK is performed considering the external reactivity variation and measured power signal as the only inputs. As

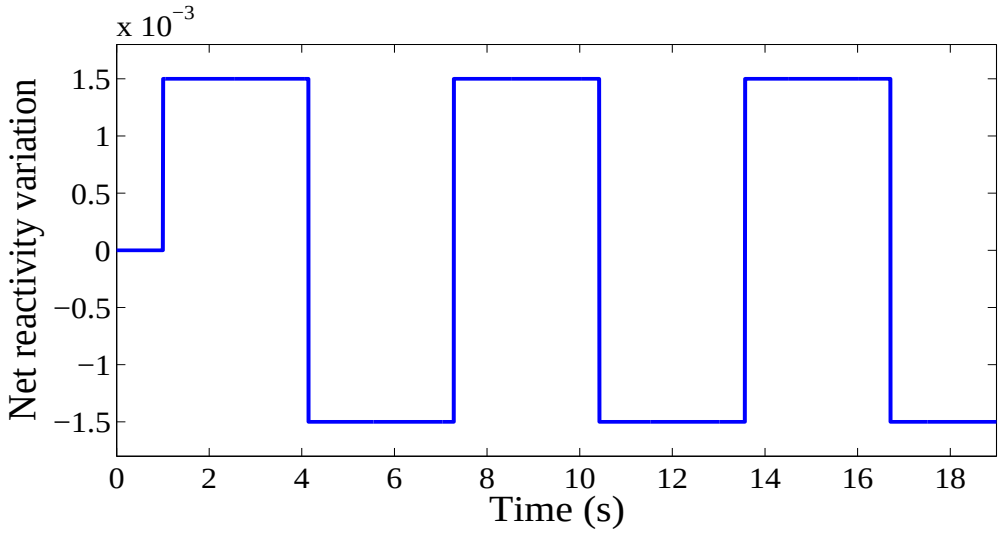

FIGURE 5.3: Net reactivity variation

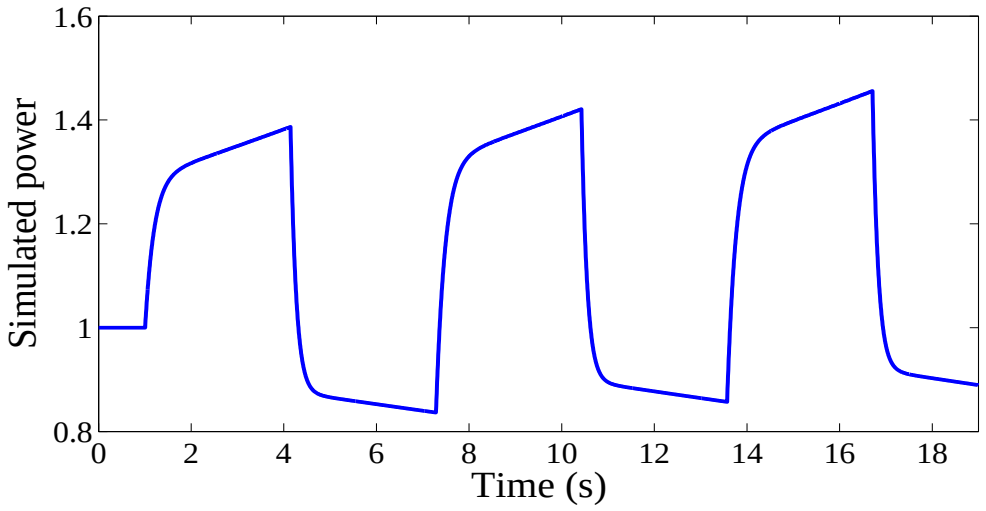

FIGURE 5.4: Simulated power

regards the application of the estimation algorithms, the values of matrices related to the covariance of uncertainty in the system and measurement noise are taken as $Q = 1 \times 10^{-6} I_4$ and $R = 1 \times 10^{-4}$, where I_4 is a unity matrix of the order 4. The time variation of the estimated state variables are shown in Fig. 5.6 through Fig. 5.9.

TABLE 5.1: Delayed neutron parameters

Group	1	2	3	4	5	6
$\beta_i\ (\times 10^{-3})$	0.2112	1.4016	1.2544	2.5280	0.7360	0.2688
$\lambda_i\ (s^{-1})$	0.0124	0.0305	0.111	0.301	1.140	3.010

prompt neutron generation time, $l = 10^{-3} s$

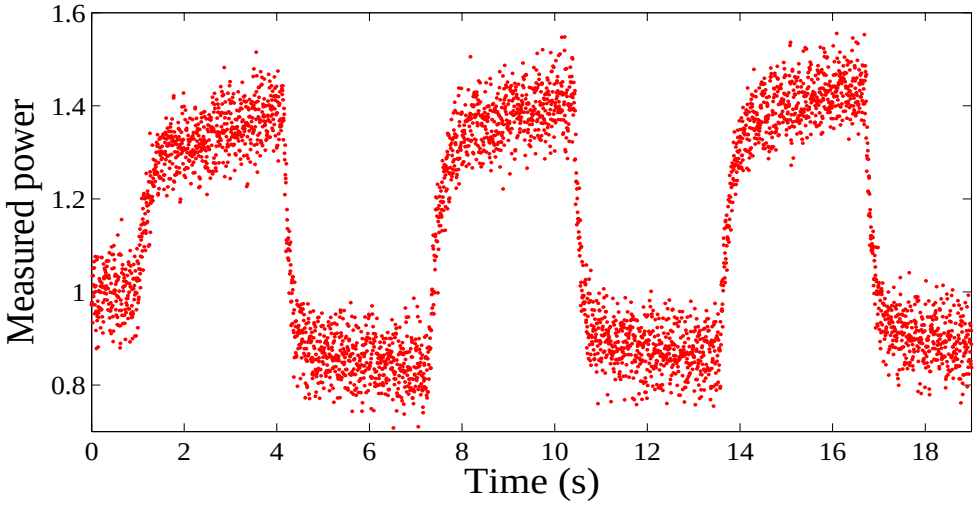

FIGURE 5.5: Simulated power with Noise

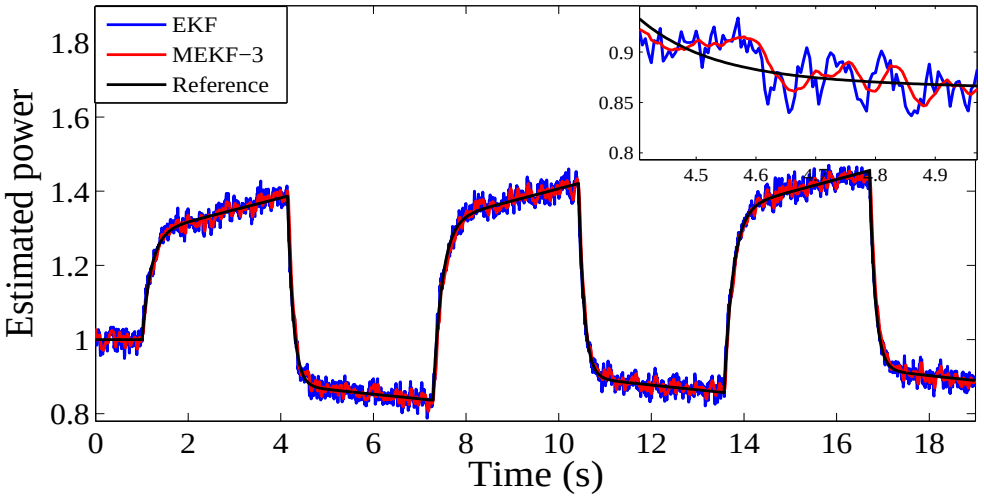

FIGURE 5.6: Estimated reactor Power

TABLE 5.2: Mean Squared Error

Quantity	MSE			
	P($\times 10^{-4}$)	C($\times 10^{-5}$)	θ_F($\times 10^{-3}$)	θ_C($\times 10^{-4}$)
EKF	2.5559	3.5796	3.9217	2.5039
MEKF-1	2.3689	3.4707	3.8165	2.4367
MEKF-2	2.1757	3.0784	**2.2867**	**1.3578**
MEKF-3	**2.1411**	**2.7974**	5.0878	3.3204
MEKF-4	2.9202	4.0440	15.0331	9.9755
MEKF-5	5.1567	8.9027	35.6921	23.7221

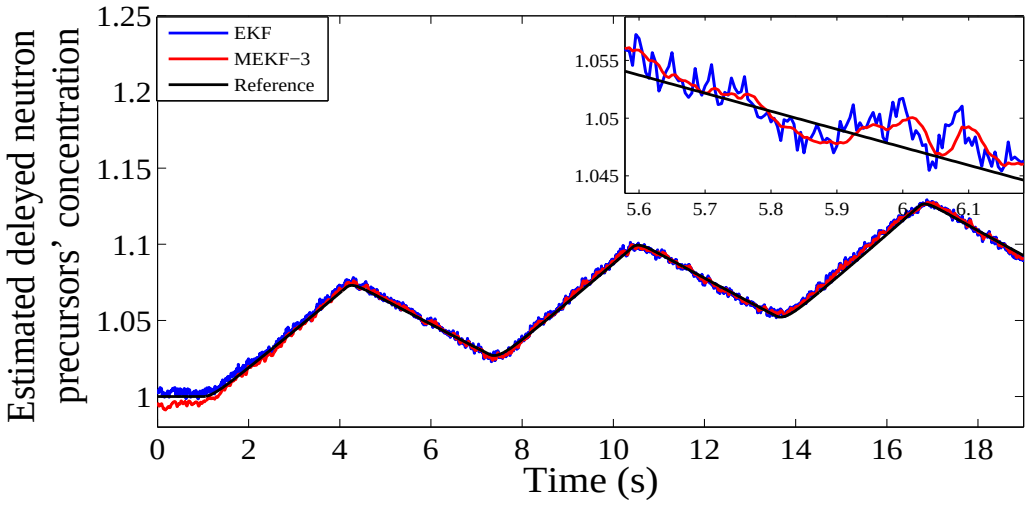

FIGURE 5.7: Estimated delayed neutron precursors' concentration

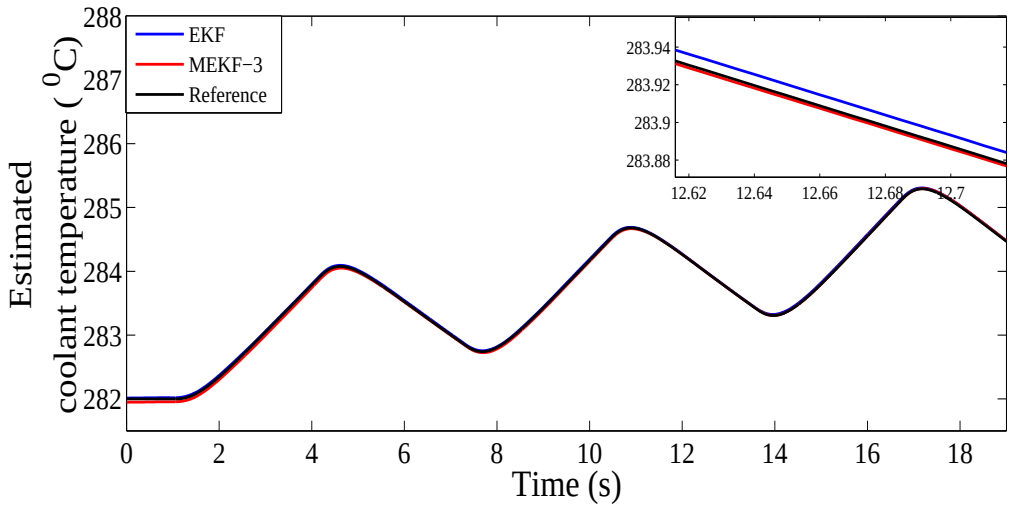

FIGURE 5.8: Estimated average coolant temperature variation

From the simulation results, it is evident that the estimated values from MEKF and EKF techniques are in good agreement with the true values. However, the results obtained from the MEKF technique effectively reduces the noise than that from the EKF technique. In order to compare the performance of the algorithms quantitatively, the Mean Squared Errors (MSE) of the estimated quantities are shown in Table 5.2. From the results, it is evident that the MSE of the results obtained from the MEKF algorithm is significantly smaller than that from the standard EKF technique. Moreover, it is evident that MSE for the estimated quantities reduces with the increment in the scale, achieves minimum value at a certain scale then increases due to the over-smoothing and delay in the estimation.

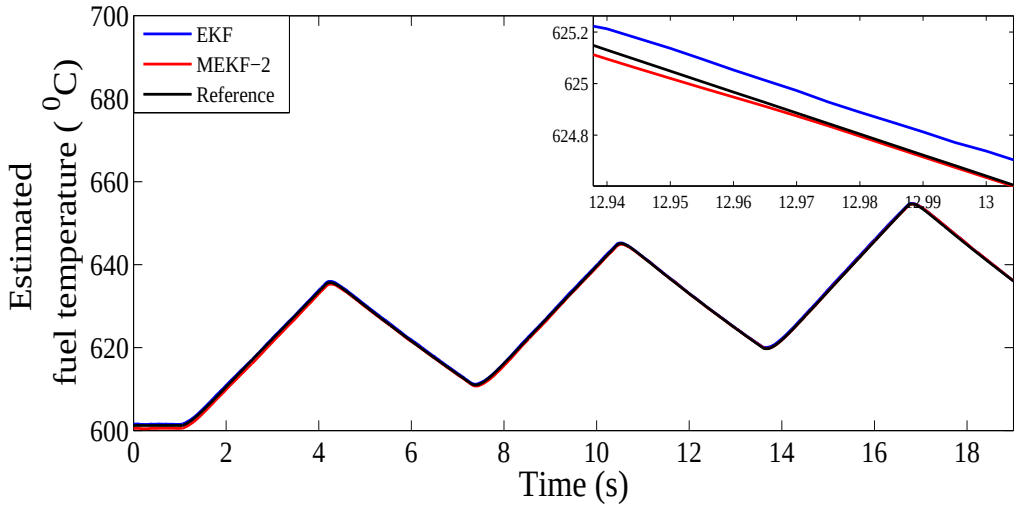

FIGURE 5.9: Estimated average fuel temperature variation

With the increment in the wavelet scale, the length of the wavelet window increases which allows more data points to pass through the filter. Therefore, over-filtering, in turn, results in over-smoothing and delay in the estimation.

5.5 Summary

In this chapter, the stationary wavelet transform based multi-scale EKF technique has been investigated for online estimation of state variables of the nuclear reactor system. The proposed algorithm preserves merits of the EKF technique and effectively estimates the state variable of the stochastic nuclear reactor system. Stationary wavelet transform effectively captures the multi-scale state variables and provides additional smoothing effect in the estimation. Simulation results show that the proposed algorithm outperforms the standard EKF algorithm. Moreover, in order to estimate the temperate variation in each fuel bundle of a large nuclear reactor, proper flux mapping technique may be integrated with the proposed state estimation algorithm.

Chapter 6

Multi-scale PCA for Fault Detection and Isolation

The subject matter of the previous Chapters was state estimation using EKF, MEKF or RNDDR. Another important aspect of process monitoring procedures is fault detection and Isolation (FDI). The estimation techniques reported in the previous Chapters have some strong applications in the context of first principle model based FDI techniques. However, for a complex large-scale industrial processes, first principle model based FDI techniques are generally undesirable. This because development and calibration of a process model based on the first principle is a difficult task and the model development exercise may result in a too complicated model to be useful. Consequently, the data driven FDI methods are extensively investigated to serve the purpose. Moreover, in this context, PCA based FDI techniques have found a prominent place. For the multi-scale systems, multi-scale variants of such techniques have also been reported. However, enough attention has not been paid to analyse the reliability of such techniques and effective isolation of the faulty variables remains underexplored.

In this chapter, a fault detection and isolation technique based on multi-scale PCA framework is presented. It is shown here that the multi-scale PCA based MSMP technique overcomes some of the shortcomings of conventional PCA by retaining the statistical basis for the monitoring charts. Moreover, since each event occurs over a certain frequency band, MSPCA possesses greater sensitivity in fault

detection and process changes. The basic concepts relevant to the conventional PCA based fault detection and isolation technique is described in Appendix A. A new reconstruction based fault isolation procedure, the multiscale PCA algorithm, reliability analysis of the proposed technique followed by the simulation results are described as follows.

6.1 Fault isolation based on reconstruction

Dunia et al. [92] proposed a fault isolation procedure based on variable reconstruction approach. Assuming that the faults are additive, the isolation procedure suspects each of the measured variables for the fault and the magnitude of the fault is estimated to reconstruct the sampled vector. Considering that the variable x_j of the sampled vector $\mathbf{x}$ is suspected for the fault, the reconstructed fault free vector denoted as $\hat{\mathbf{x}}_j$ is calculated as

$$\hat{\mathbf{x}}_j = \mathbf{x} - \hat{f}_j \boldsymbol{\zeta}_j \qquad j = 1, 2, \cdots, m \tag{6.1}$$

where $\hat{f}_j$ is the estimated fault magnitude, and $\boldsymbol{\zeta}_j$ is a column vector representing the faulty variable. It is of length equal to the number of sensors and its j^{th} element is one and the rest of its elements are zero. The detection index for the reconstructed vector $\mathbf{x}_j$ is calculated as

$$\text{Index}(\hat{\mathbf{x}}_j) = \hat{\mathbf{x}}_j^\top \mathbf{M} \hat{\mathbf{x}}_j. \tag{6.2}$$

Substituting the value of $\hat{\mathbf{x}}_j$ from (6.1) into (6.2) yields

$$\text{Index}(\hat{\mathbf{x}}_j) = \text{Index}(\mathbf{x}) - 2\hat{f}_j \boldsymbol{\zeta}_j^\top \mathbf{M}\mathbf{x} + \hat{f}_j^2 \boldsymbol{\zeta}_j^\top \mathbf{M} \boldsymbol{\zeta}_j \tag{6.3}$$

Equating the derivative of $\text{Index}(\hat{\mathbf{x}}_j)$ to zero and solving it for $\hat{f}_j$ yields

$$\hat{f}_j = \frac{\boldsymbol{\zeta}_j^\top \mathbf{M}\mathbf{x}}{\boldsymbol{\zeta}_j^\top \mathbf{M} \boldsymbol{\zeta}_j}. \tag{6.4}$$

Substituting $\hat{f}_j$ from (6.4) into (6.3) yields

$$\begin{aligned} \text{Index}(\hat{\mathbf{x}}_j) &= \text{Index}(\mathbf{x}) - \kappa_j \\ \kappa_j &= \frac{(\boldsymbol{\zeta}_j^\top \mathbf{M}\mathbf{x})^2}{\boldsymbol{\zeta}_i^\top \mathbf{M}\boldsymbol{\zeta}_j} \end{aligned} \tag{6.5}$$

making, $\text{Index}(\mathbf{x}) - \text{Index}(\hat{\mathbf{x}}_j) = \kappa_j$, which is the amount of reduction obtained from $\text{Index}(\mathbf{x})$ by reconstructed variable. As M is positive definite matrix, $\kappa_j \geq 0$. If the suspected variable is the same as the faulty variable, the largest reduction in $\text{Index}(\mathbf{x})$ is expected which can be assessed with the sensor validation index (SVI) [92] defined as

$$\text{SVI}_j = \frac{\text{Index}(\hat{\mathbf{x}}_j)}{\text{Index}(\mathbf{x})}. \tag{6.6}$$

Consider that, after suspecting each of the variables, in the first iteration of the isolation procedure, the variable x_{p1} yields minimum SVI hence identified as faulty. The fault detection index for the reconstructed vector is

$$\text{Index}(\hat{\mathbf{x}}_{p_1}) = \text{Index}(\mathbf{x}) - \kappa_{p_1} \tag{6.7}$$

In the case of multiple faulty variables, the detection index for the first reconstructed variable could be expected to exceed the control limits. Therefore, if $\text{Index}(\hat{\mathbf{x}}_{p_1}) > \gamma_\alpha$, in order to isolate other faulty variables, the isolation process is repeated by replacing the sampled vector $\mathbf{x}$ with the reconstructed vector $\hat{\mathbf{x}}_{p_1}$. The fault isolation process is iteratively repeated until the detection index for the reconstructed vector is within the control limits. Assume that t variables are found faulty i.e., total t iterations were required to bring the detection index of the reconstructed vector within the control limits. The fault detection index after t^{th} iteration, $\text{Index}(\hat{\mathbf{x}}_{p_t})$ could be calculated using relation (6.7) as

$$\begin{aligned} \text{Index}(\hat{\mathbf{x}}_{p_t}) &= \text{Index}(\hat{\mathbf{x}}_{p_{t-1}}) - \kappa_{p_t} \\ &= \text{Index}(\hat{\mathbf{x}}_{p_{t-2}}) - \kappa_{p_{t-1}} - \kappa_{p_t} \\ &\vdots \\ &= \text{Index}(\mathbf{x}) - \sum_{k=1}^{t} \kappa_{p_k} \end{aligned} \tag{6.8}$$

where $\sum_{k=1}^{t} \kappa_{p_k}$ is the amount of reduction from Index($\mathbf{x}$) contributed by the set of faulty variable such that Index($\hat{\mathbf{x}}_{p_t}$) $\leq \gamma_\alpha$. In order to assess contribution of each faulty variable, the contribution index is defined as

$$\mathbf{CI}^i = \frac{\kappa_i}{\sum_{k=1}^{t} \kappa_k} \qquad i = 1, 2, \cdots, t \tag{6.9}$$

where $\mathbf{CI}^i$ is the contribution of i^{th} faulty variable in the total fault.

6.2 Reliability analysis

Before application of the fault detection and isolation scheme, it is advantageous to assess the likelihood for the successful fault detection and isolation. In this section, a statistical test to measure autocorrelation in the time-series data followed by the derivation for estimating the variance of the reconstruction error is presented.

6.2.1 Autocorrelation-test:Ljung-Box Q statistic

In order to assess the time-dependence of the measured variables, it is intuitive to calculate the autocorrelation coefficients at different lags. Although coefficients plotted over different lags provide a reliable measure for randomness, it is difficult to compare the amount of randomness between two datasets containing a large number of variables. This happens because a large number of plots has to be compared which may raise concern over characterizing a better plot. Therefore, instead of analyzing autocorrelation coefficients plotted at each lag, the overall randomness is assessed by calculating the Ljung-Box Q statistic. It measures the cumulative effect of the coefficients at first L lags which is defined as follows

$$Q = N(N+2) \sum_{l=1}^{L} \frac{\rho_l^2}{N-l} \tag{6.10}$$

where N is the number of samples, ρ_l is the autocorrelation coefficients at lag l, and L is the number of lags being tested. As discussed in [108], for the time-independent samples Q statistic approximately follows the χ^2 distribution with L degrees of freedom.

6.2.2 Variance of Reconstruction Error

The reliability of the reconstruction procedure for the fault isolation derived in section 6.1 can be assessed by estimating the variance of reconstruction error (VRE) [92]. In the process to reconstruct the fault-free variation of the suspected variable using all the measured variables, there is always a fraction of the variation that cannot be reconstructed by the other variables leading to the reconstruction error. In this subsection, the procedure to estimate the variance of reconstruction error is presented.

Considering that the variable x_i is faulty, the sampled vector $\mathbf{x}$ is denoted as

$$\mathbf{x} = \mathbf{x}^* + f_i\boldsymbol{\zeta}_i \tag{6.11}$$

where $\mathbf{x}^*$ is the vector free from the fault in variable x_i, $\boldsymbol{\zeta}_i$ is the column vector representing the index of the faulty variable and, scalar f_i is the magnitude of actual fault which would be zero if x_i is fault-free. In the fault isolation procedure, if the suspected variable is the same as the faulty variable (e.g. $j = i$), substituting (6.11) into (6.1), the reconstruction error can be obtained as

$$\hat{\mathbf{x}}_i - \mathbf{x}^* = \left(f_i - \hat{f}_i\right)\boldsymbol{\zeta}_i. \tag{6.12}$$

Using (6.11) in (6.4) yields

$$\hat{f}_i = \frac{\boldsymbol{\zeta}_i^\top \mathbf{M}(\mathbf{x}^* + f_i\boldsymbol{\zeta}_i)}{\boldsymbol{\zeta}_i^\top \mathbf{M}\boldsymbol{\zeta}_i} \tag{6.13}$$

making,

$$f_i - \hat{f}_i = \frac{\boldsymbol{\zeta}_i^\top \mathbf{M}\mathbf{x}^*}{\boldsymbol{\zeta}_i^\top \mathbf{M}\boldsymbol{\zeta}_i}. \tag{6.14}$$

Therefore, the reconstruction error is

$$\hat{\mathbf{x}}_i - \mathbf{x}^* = \frac{\boldsymbol{\zeta}_i^\top \mathbf{M}\mathbf{x}^*}{\boldsymbol{\zeta}_i^\top \mathbf{M}\boldsymbol{\zeta}_i}\boldsymbol{\zeta}_i, \tag{6.15}$$

and

$$\|\hat{\mathbf{x}}_i - \mathbf{x}^*\|^2 = (f_i - \hat{f}_i)^2 = \left(\frac{\boldsymbol{\zeta}_i^\top \mathbf{M}\mathbf{x}^*}{\boldsymbol{\zeta}_i^\top \mathbf{M}\boldsymbol{\zeta}_i}\right)^2. \tag{6.16}$$

It can be observed that the reconstruction error is independent of the fault magnitude and depends only on the individual variable. The VRE for variable x_i, denoted as u_i is defined as the variance of the i^{th} element of error vector $\hat{\mathbf{x}}_i - \mathbf{x}^*$.

$$\begin{aligned} u_i &= var\left[\boldsymbol{\zeta}_i^\top(\hat{\mathbf{x}}_i - \mathbf{x}^*)\right] = \varepsilon\left(\|\hat{\mathbf{x}}_i - \mathbf{x}^*\|^2\right) && (6.17)\\ &= \frac{\boldsymbol{\zeta}_i^\top \varepsilon\left(\tilde{\mathbf{x}}^*\tilde{\mathbf{x}}^{*\top}\right)\zeta_i}{(\boldsymbol{\zeta}_i^\top \mathbf{M}\boldsymbol{\zeta}_i)^2} && (6.18)\\ &= \frac{\boldsymbol{\zeta}_i^\top \mathbf{R}\boldsymbol{\zeta}_i}{(\boldsymbol{\zeta}_i^\top \mathbf{M}\boldsymbol{\zeta}_i)^2} && (6.19) \end{aligned}$$

where $\tilde{\mathbf{x}}^* = \mathbf{M}\mathbf{x}^*$, and $\mathbf{R} = \varepsilon[\tilde{\mathbf{x}}^*\tilde{\mathbf{x}}^{*\top}]$ is the covariance matrix which can be estimated from the data collected during normal operation. Alternatively, VRE can also be expressed in terms of variance of estimated fault magnitude,

$$u_i = \varepsilon\|\hat{\mathbf{x}}_i - \mathbf{x}^*\|^2 = \varepsilon(\hat{f}_i - f_i)^2 \tag{6.20}$$

In the case of fault-free condition, $u_i = \varepsilon(\hat{f}_i^2)$ which means VRE represents the variance of estimated fault magnitude calculated from data for normal operating condition. Moreover, in order to assess the overall effect of VRE, the weighted average value of VRE can be calculated as

$$\mathbf{u} = \frac{1}{m}\sum_{i=1}^{m} q_i u_i \tag{6.21}$$

where q_i denotes the weight assigned to the sensor i.

6.3 Multiscale Principal Component Analysis

Measured variables of the industrial processes may have contributions of several events like measurement noise, instrument failure, parameter drifts, process dynamics, and operator induced events. Each of these events may have features with significant contribution over a certain time and frequency. Therefore, it is important to analyze the variable in time as well as in the frequency domain simultaneously. Moreover, ignorance of the autocorrelated features of the measured variables may influence the descriptive ability of PCA model which may lead to incorrect control limits and higher PCs for given CVP [116]. As wavelets possess the ability to de-correlate the certain signals along with the ability to extract multi-scale feature of the signals, the PCA models built over wavelet transformed data could be expected to have some advantages i.e., each PCA model employed at certain scale would be more sensitive to the abnormal events whose spectrum is most significant at selected scale and, control limits calculated over such models could be expected to be more reliable as wavelet transformed data are less autocorrelated. Steps of the proposed multi-scale PCA algorithm for the fault detection and isolation are summarized in the flowchart shown in Fig. 6.1.

6.4 Simulation Results

In this section, the performance of the proposed multi-scale technique is compared with that of the single scale counterpart. Process description followed by simulation results are explained in the following.

6.4.1 TE Process

The TE process is well known industrial chemical process. It consists of five operational units; namely reactor, condenser, liquid − vapor separator, stripper, and compressor. The process produces two liquid products from the four gaseous reactants by irreversible and exothermic reactions. The flow diagram of the process is shown in Fig. 6.2. Table 6.1 lists the process variables. The manipulated

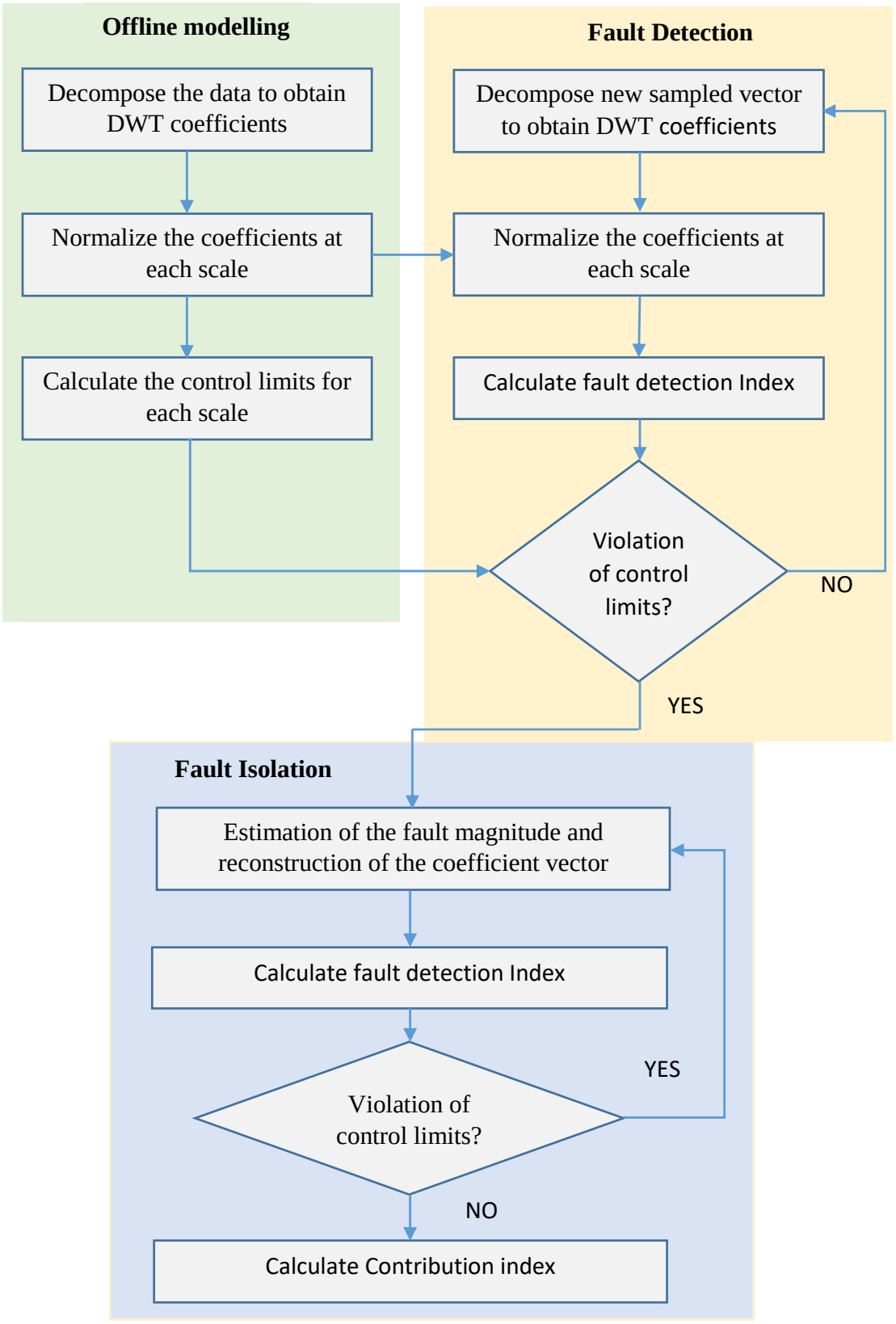

FIGURE 6.1: flowchart for multi-scale PCA

variables associated with process are x_1 to x_{22}, and x_{42} to x_{52}. These variables are sampled at every 3 minutes. Variables associated with composition measurements are x_{23} to x_{41}. Among them, variables associated with stream 6 and 9, i.e., x_{23} to x_{36} are sampled every 6 minutes, and variables associated with stream 11, i.e., x_{37} to x_{41} are sampled every 15 minutes. The detail description about the process can be found in [1] and [117].

Russell et al. [1] generated the simulation data-set for the process which is widely used as a benchmark for testing fault detection and isolation techniques. The data-set can be downloaded from http://web.mit.edu/braatzgroup/links.html. The training data contain 480 samples of 52 variables under normal operating condition which is used to build the PCA model. Same data are transformed into wavelet coefficients upto scale depth 3 to derive multi-scale PCA models. For all the PCA models, the number of PCs are selected to retain 90% of cumulative variance.

For each of the process variables, reliability parameters i.e., LBQ statistic and VRE are calculated for the PCA model as well as for multi-scale PCA models. Values of these statistics for the PCA model and multi-scale PCA at the finest and the coarsest scale of decomposition denoted as MSPCA-1d and MSPCA-3a respectively are plotted in plotted in Fig. 6.3 and 6.4. It can be observed that the values for the variables in the multi-scale PCA models are significantly lower than those for the single scale PCA model. Moreover, for the different PCA models, the number of PCs along with equally weighted LBQ statistic and VRE are shown in Table 6.2. It can be observed that the values of all these parameters for the multi-scale PCA models are significantly smaller than the single scale PCA model suggesting the superior quality of multi-scale PCA models. This is obvious because in the wavelet projection space, the deterministic and stochastic part of the measured variables are well separated and coefficients are decorrelated.

The testing dataset contains 960 samples of 21 faulty operations. In this work, benchmark fault 5 and fault 17 are analyzed. A scenario of the benchmark fault 5 was that the condenser cooling water inlet temperature undergoes step disturbance after 160^{th} sample. As analyzed in [1], the significant effect of the disturbance is

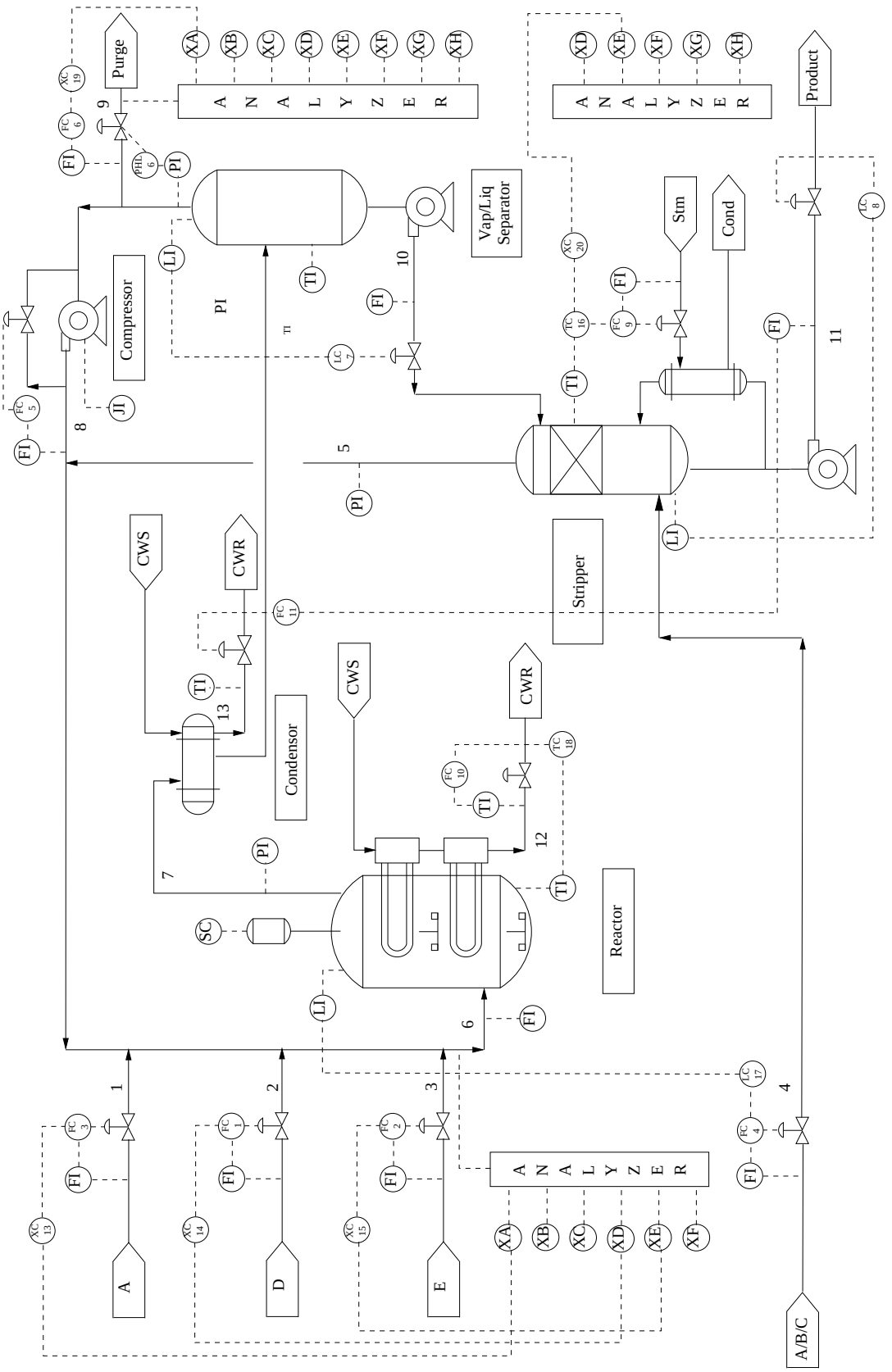

FIGURE 6.2: Flow-diagram of Tennessee Eastman process

TABLE 6.1: Monitored process variables [1]

ID	Variable Description	ID	Variable Description
x1	A feed (stream 1)	x27	Component E (stream 6)
x2	D feed (stream 2)	x28	Component F (stream 6)
x3	E feed (stream 3)	x29	Component A (stream 9)
x4	A and C feed (stream 4)	x30	Component B (stream 9)
x5	Recycle flow (stream 8)	x31	Component C (stream 9)
x6	Reactor feed rate (stream 6)	x32	Component D (stream 9)
x7	Reactor pressure	x33	Component E (stream 9)
x8	Reactor level	x34	Component F (stream 9)
x9	Reactor temperature	x35	Component G (stream 9)
x10	Purge rate (stream 9)	x36	Component H (stream 9)
x11	Product separator temperature	x37	Component D (stream 11)
x12	Product separator level	x38	Component E (stream 11)
x13	Product separator pressure	x39	Component F (stream 11)
x14	Product separator underflow (stream 10)	x40	Component G (stream 11)
x15	Stripper level	x41	Component H (stream 11)
x16	Stripper pressure	x42	MV to D feed flow (stream 2)
x17	Stripper underflow (stream 11)	x43	MV to E feed flow (stream 3)
x18	Stripper temperature	x44	MV to A feed flow (stream 1)
x19	Stripper steam flow	x45	MV to total feed flow (stream 4)
x20	Compressor work	x46	Compressor recycle valve
x21	Reactor cooling water outlet temperature	x47	Purge valve (stream 9)
x22	Separator cooling water outlet temperature	x48	Separator pot liquid flow
x23	Component A (stream 6)	x49	Stripper liquid product flow
x24	Component B (stream 6)	x50	Stripper steam valve
x25	Component C (stream 6)	x51	Reactor cooling water flow
x26	Component D (stream 6)	x52	Condenser cooling water flow

TABLE 6.2: Number of principal components, VRE and LBQ values of PCA and MSPCA

Method	Number of principal components	VRE	LBQ-test value
PCA	32	0.5967	723.57
MSPCA-1d	30	0.5756	66.51
MSPCA-2d	28	0.4794	22.81
MSPCA-3d	25	0.3455	12.33
MSPCA-3a	20	0.2981	80.63

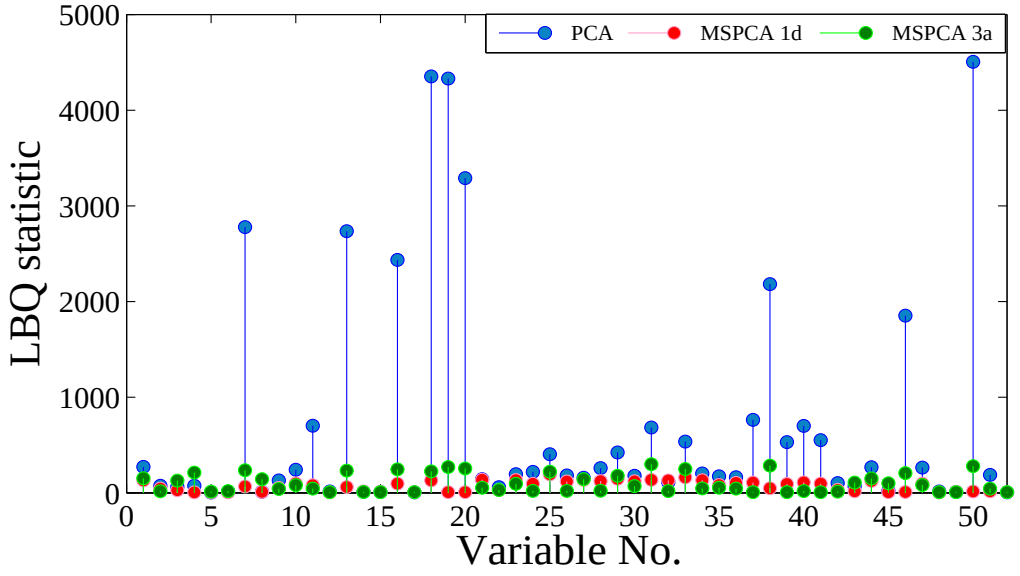

FIGURE 6.3: LBQ statistic

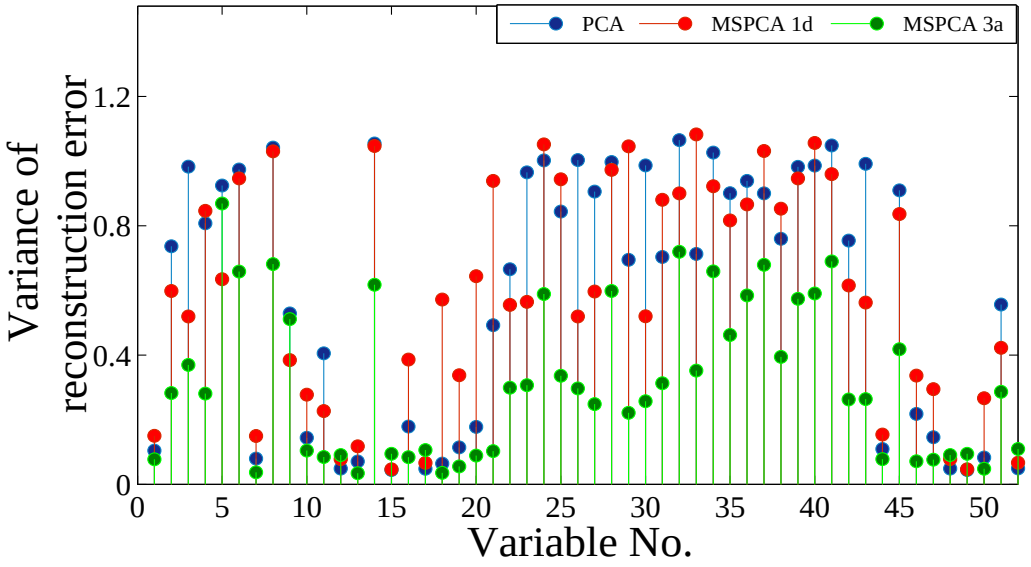

FIGURE 6.4: Variance of reconstruction error

to induce step change in variable x_{52} (condenser cooling water flow-rate) which is plotted in Fig. 6.5. The spectral range of the fault in a variable x_{52} has predominantly low frequency features, i.e., in a range matching with wavelet approximation level at scale 3, which is 0 to $0.125 f_s$. Moreover, due to the actions of various controllers employed in the process, 32 process variables undergo transient variations that settle in about 200 samples.

The combined fault detection index based on PCA with the corresponding control

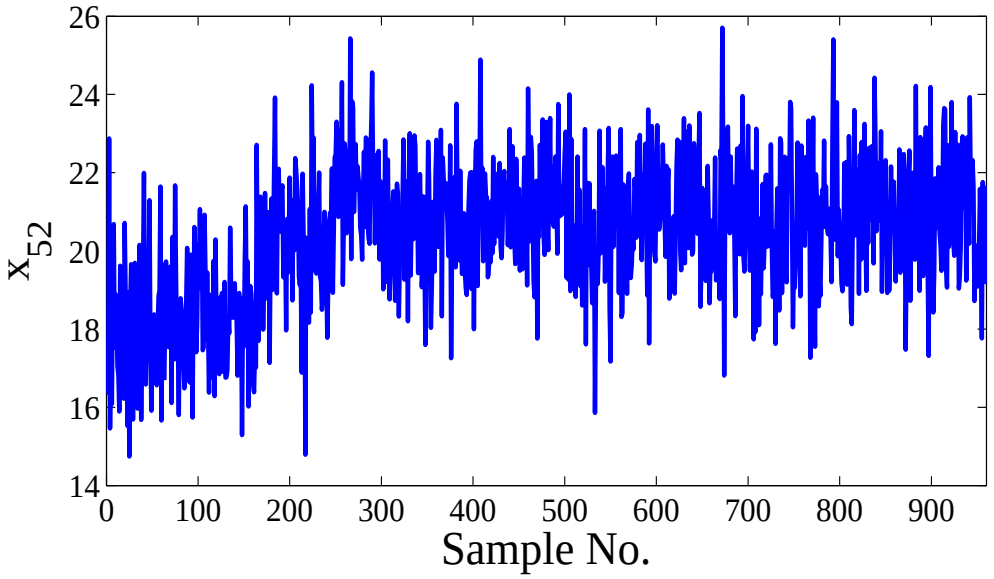

FIGURE 6.5: faulty variable for fault 5: x_{52}

limits is plotted in Fig. 6.6(a). It can be observed that the fault detection procedure fails to detect the fault after 200 samples of its occurrence. This also confirms the observation of the PCA based fault detection indices in [1]. Consequently, the fault isolation statistic cannot isolate the faulty variables continuously as shown in Fig. 6.7(a). From these observations, the operator may conclude that the fault has 'disappeared'within 200 samples of its occurrence. However, the detection index with MSPCA-3a model statistics continuously informs the operator about the presence of the fault as shown in Fig. 6.6(b). Moreover, from the fault isolation indices with MSPCA-3a model are plotted in 6.7(b), it can be observed that variable x_{52} is continuously separated and other variables have settled to normal operating condition within 200 samples of fault occurrence. The detection index with MSPCA-3a model, i.e, with the coarsest PCA model continuously detect the fault due to the fact the deterministic and stochastic portion of the variable is effectively separated and the model effectively captures the coarse variation of the variable x_{52}.

A scenario of the benchmark fault 17 is classified as unknown [117]. However, the variables with abnormal trends are x_9, x_{21} and x_{51} which are plotted in Fig. 6.8. The spectral range of the faulty variables, i.e., x_9, x_{21} and x_{51} has a combination of features dominant in the spectral range matching with the wavelet approximation at scale-3 and with the detail at level-1. This means a range of frequencies is in the

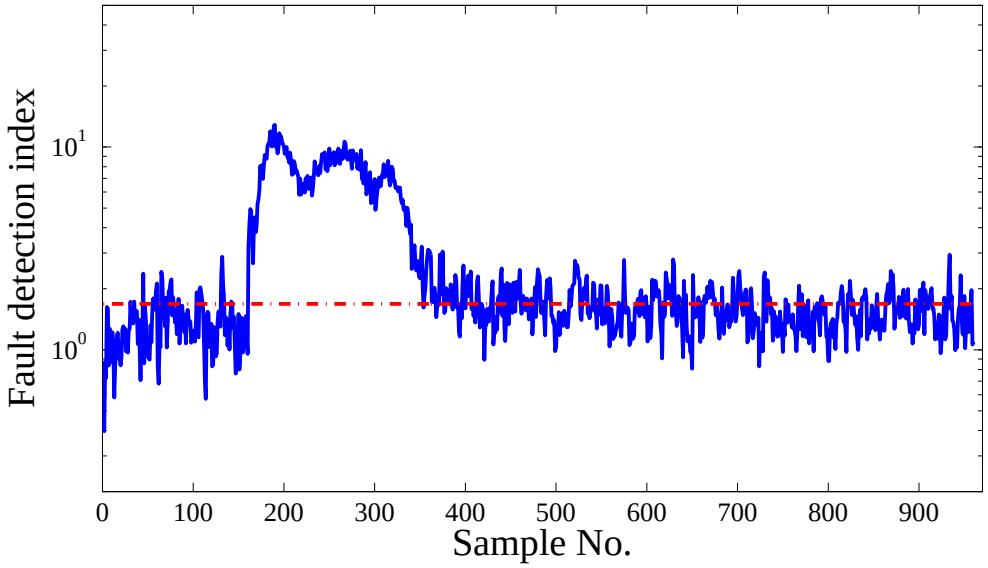

(a)

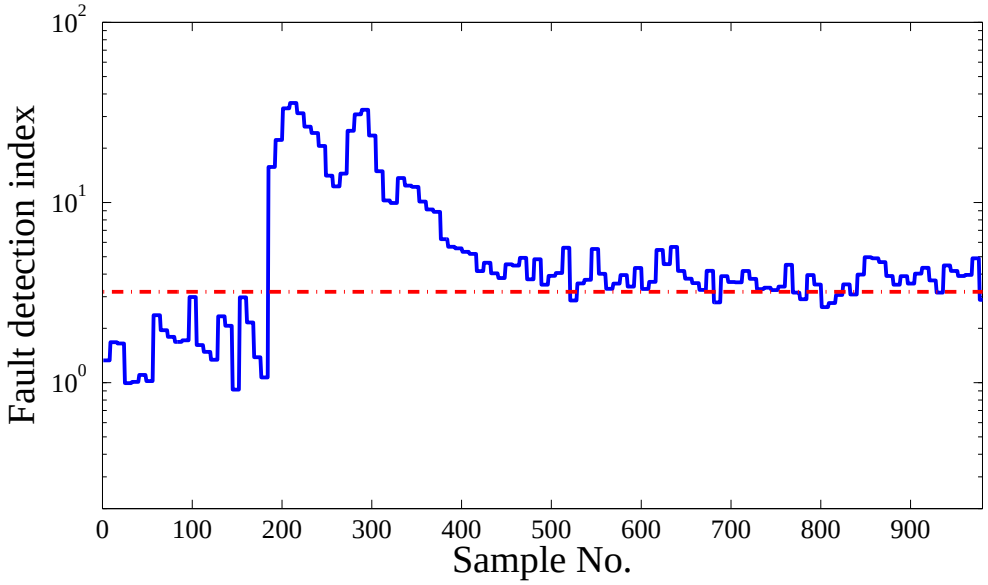

(b)

FIGURE 6.6: Fault detection index for fault 5 with (a) PCA (b) MSPCA-3a

a band of 0 to $0.125f_s$, and in a band of $0.5f_s$ f_s where $f_s = 2.8mHz$ is the Nyquist frequency of samples. The fault detection index with PCA based model detects the fault after the 160th sample as plotted in Fig. 6.9(a). The combined fault detection index with coarsest model i.e, MSPCA-3a and finest model i.e, MSPCA-1d also detects as plotted in Fig. 6.9(b) and 6.9(c) respectively. The coarsest model captures the abnormal coarse variation of disturbance and finest model captures abnormal high frequency variations of the disturbance. The information from these two models suggests the operator for the possibility of different disturbances.

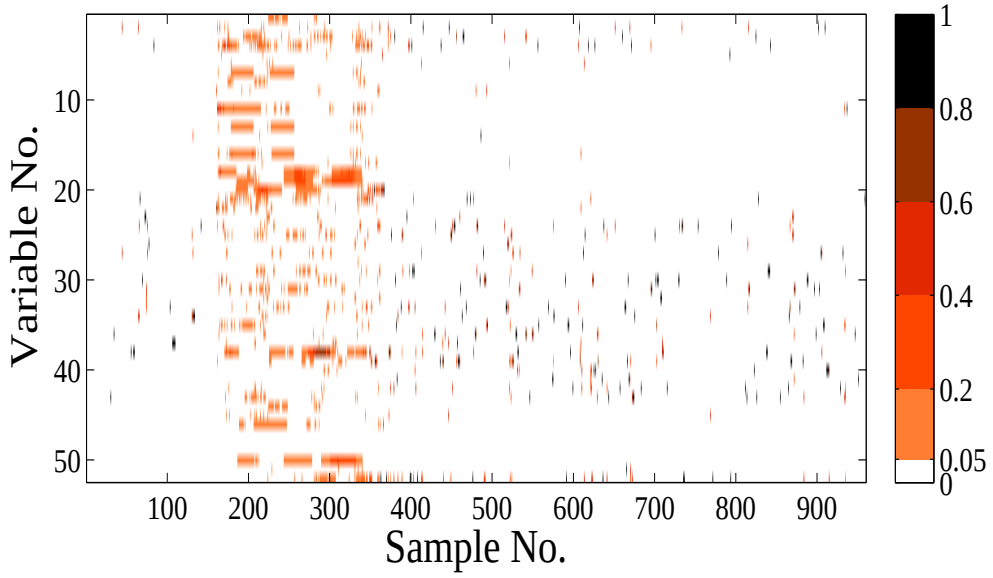

(a)

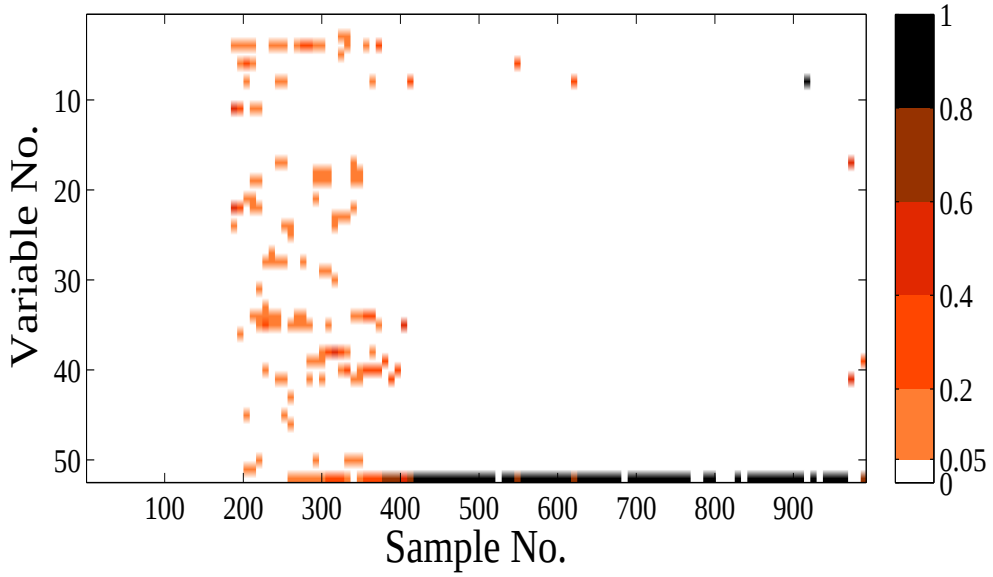

(b)

FIGURE 6.7: Fault isolation index for fault 5 with (a) PCA (b) MSPCA-3a

Moreover, the isolation index with PCA model for the faulty variables are plotted in Fig. 6.10(a). It can be observed that variable x_{51} is not isolated by the PCA model which might be attributed to the high value of VRE for the selected model. Furthermore, the isolation indices with MSPCA-3a and MSPCA-1d models are plotted in Fig. 6.10(b) and 6.9(c) respectively. It can be observed that variables with abnormal coarse and fine variations are effectively isolated by MSPCA-3a and MSPCA-1d models respectively.

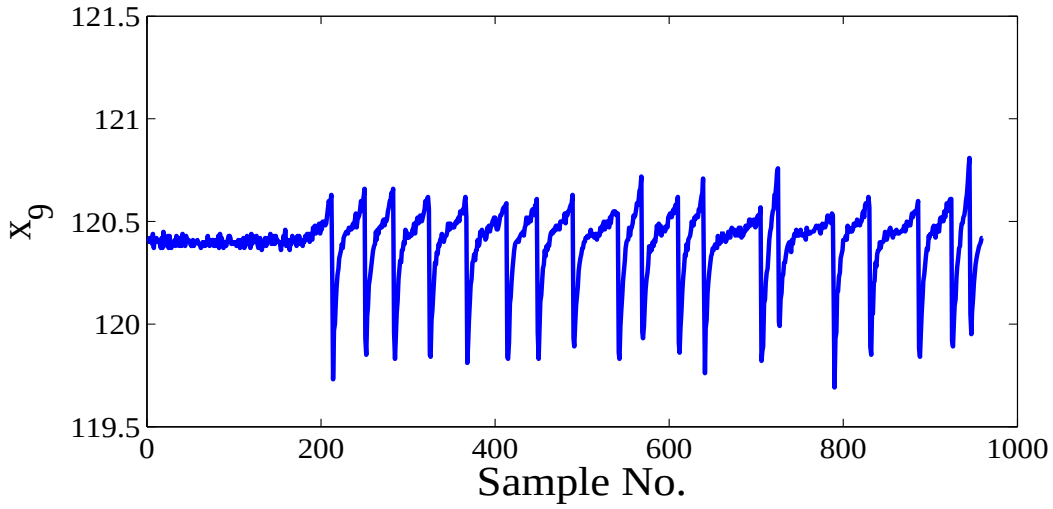

(a)

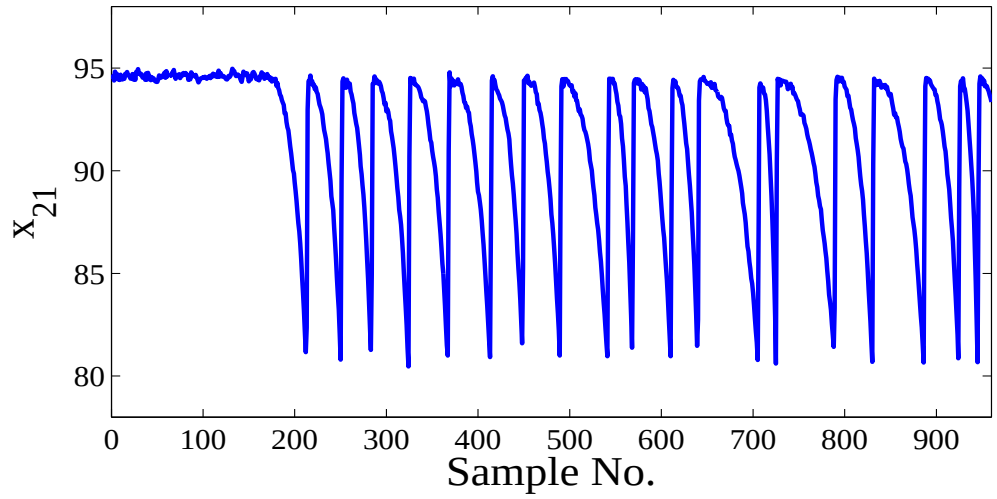

(b)

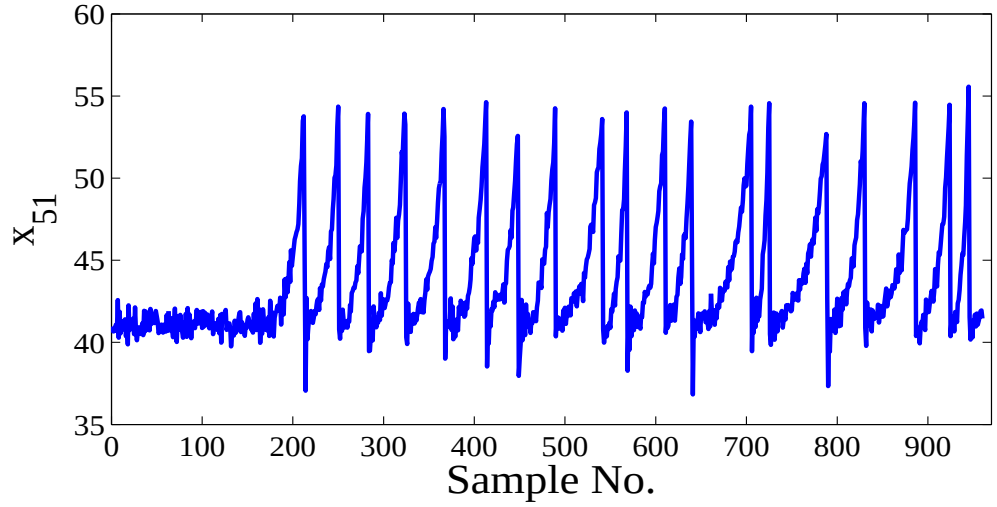

(c)

FIGURE 6.8: Faulty variables for fault 17 (a) x_9 (b) x_{21} (c) x_{51}

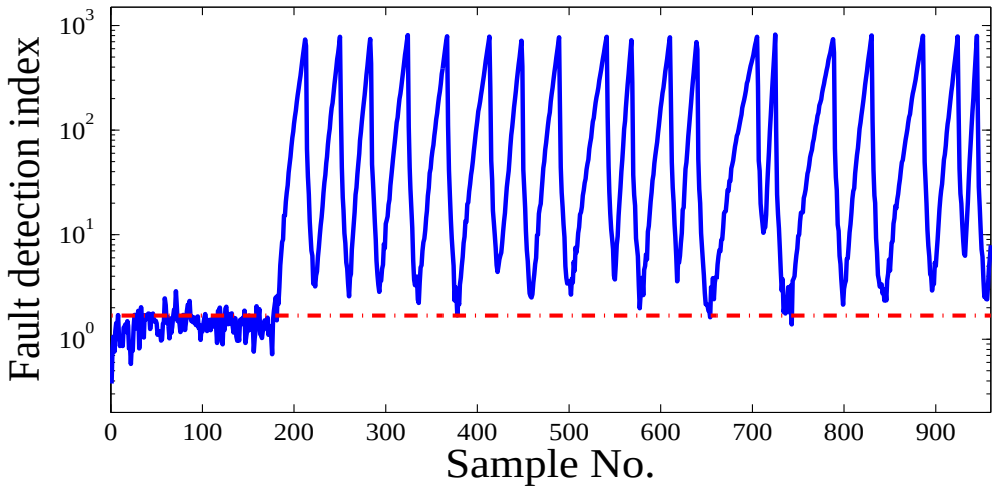

(a)

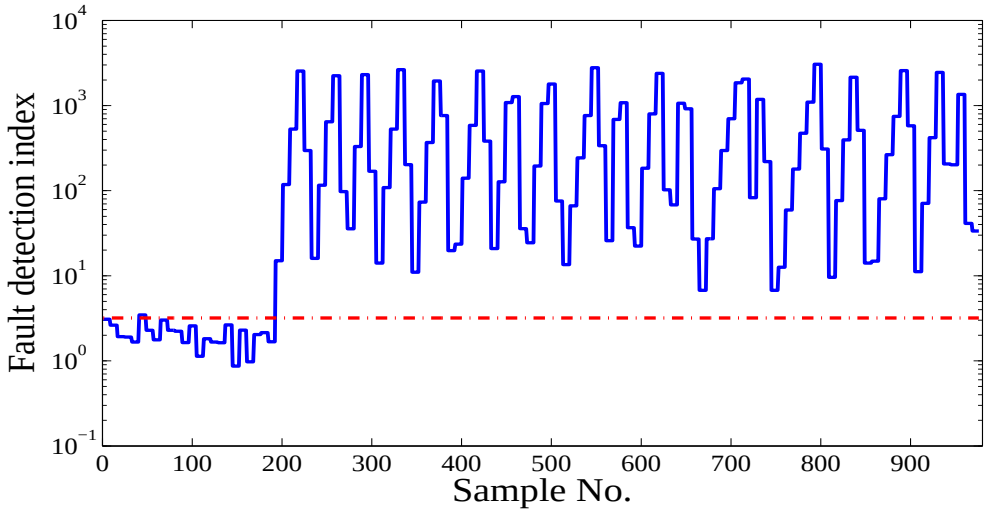

(b)

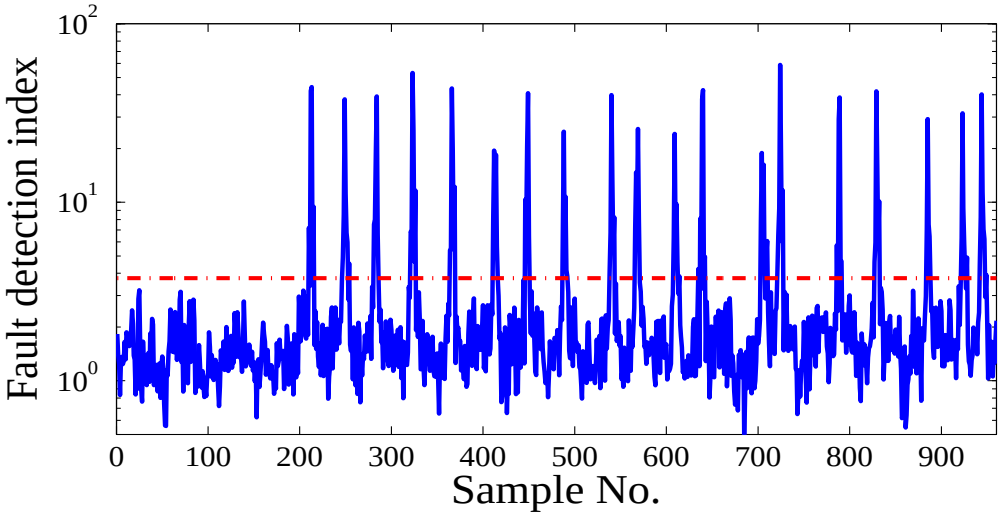

(c)

FIGURE 6.9: Combined detection index for fault 17 with (a) PCA (b) MSPCA-3a (c) MSPCA-1d

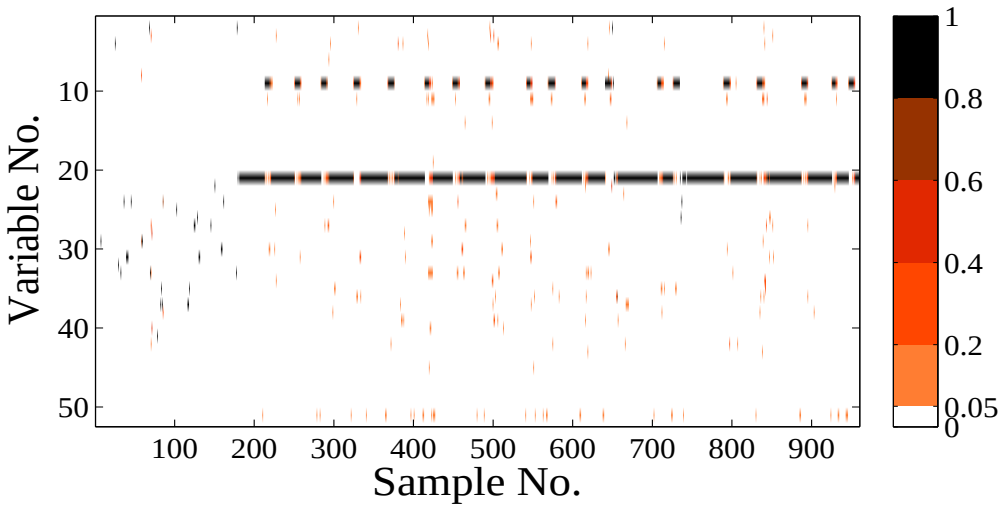

(a)

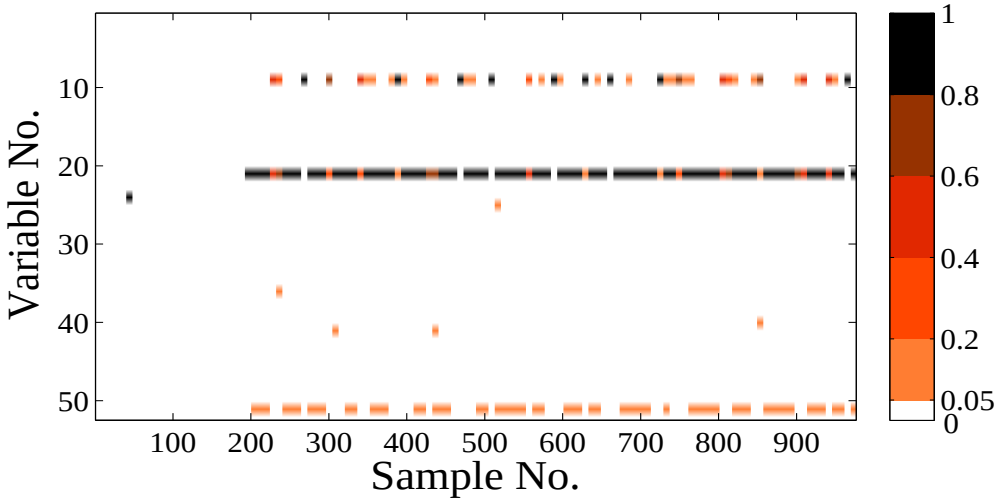

(b)

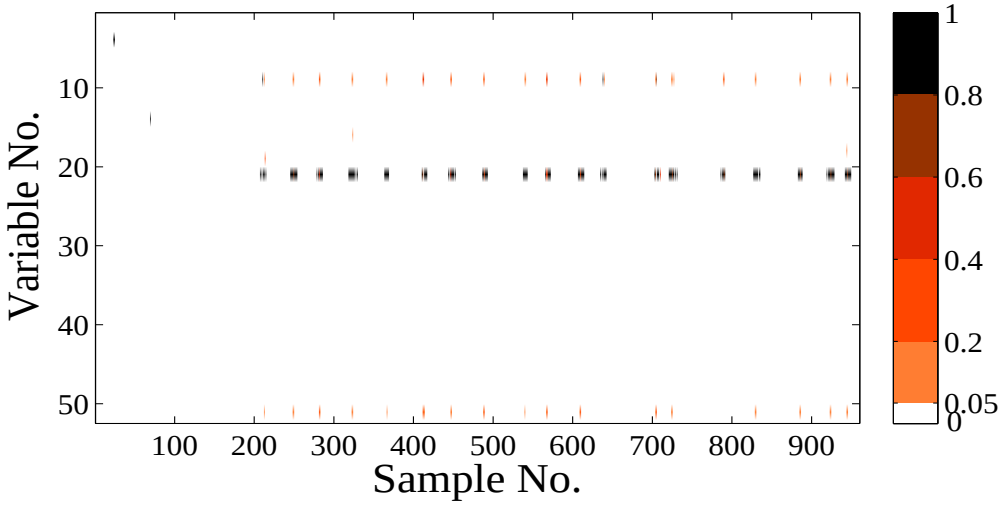

(c)

FIGURE 6.10: Fault isolation index for fault 17 with (a) PCA (b) MSPCA-3a (c) MSPCA-1d

6.5 Summary

A new reconstruction based fault isolation technique in multiscale PCA framework is presented. Although reconstruction based isolation technique eliminates the fault smearing effect, the reliability of the reconstruction procedure depends on the VRE. Results of statistical test for autocorrelation obtained with wavelet transformed coefficients indicate a significant reduction in auto-correlated features in wavelet projection space as compared with the same for the raw measurement space. Therefore, control limits for the PCA model derived over wavelet projection space could be more reliable than the same for the single scale PCA model. Moreover, for the benchmark TE process, the detection and the isolation indices obtained with the multi-scale PCA models effectively monitor some of the faulty variables which are missed out by the single-scale PCA based indices. To find the root cause of the fault, the domain knowledge of the operator is required to do investigation based on the isolated faulty variables. The PCA models derived in the projection space can give extra information about the frequency range of the fault which is potentially useful for the operator to investigate the cause of the fault.

Appendix A

Wavelets

Although there could be many ways to introduce wavelets, an intuitive way is to start with the frequency domain representation of the signals by virtue of the Fourier transform. The fundamental idea of the Fourier transform is to represent the signal as a weighted combination of sinusoidal waves. These sinusoidal waves are perfectly localized in frequency domain and possess some nice properties [121]. The major drawback, however, is that they are required to last forever, i.e., they range from time $t = -\infty$ to $t = \infty$ in time domain. Due the representation of the signal as a combination of everlasting waves, the Fourier transform fails to give information about the localized time-dependent features of the signal.

In order to overcome this drawback, Gabor introduced the *Gabor transform* which is also known as the short time fourier transform (STFT). The procedure of STFT begins with a selection of an appropriate window function preferably having finite time and frequency variances. For the signal $x(t) \in L_2(\mathbb{R})$, using window function $v(t) \in L_2(\mathbb{R})$, the STFT is defined as an inner product of the input signal with the window function located in the neighbourhood of time τ_0 and modulated with frequency Ω_0

$$\text{STFT}(\tau_0, \Omega_0) = \int_{-\infty}^{\infty} x(t)\overline{v(t-\tau_0)e^{j\Omega_0 t}}dt \tag{A.1}$$

The bar represents complex conjugate. Using Parseval's theorem, STFT can also be defined in terms of Fourier transform of the signal and window function as

$$\mathrm{STFT}(\tau_0, \Omega_0) = \frac{1}{2\pi} \int_{-\infty}^{\infty} X(\Omega) \overline{V(\Omega - \Omega_0) e^{j(\Omega_0 - \Omega)\tau_0}} d\Omega \tag{A.2}$$

where $X(\cdot)$ and $V(\cdot)$ are Fourier transforms of $x(\cdot)$ and $v(\dot{})$ respectively. The arguments τ_0 and Ω_0 indicate the movement of the STFT along with the time and frequency respectively. The resolution of STFT in time and frequency is determined by the time and frequency variances of a window function. With this representation, STFT can also be thought as slicing operator which picks the portion of the signal in the neighbourhood of the time τ_0 and frequency Ω_0. By offering some time resolution, STFT provides a major improvement over the Fourier transform. However, the time resolution is achieved only at the cost of loosing some frequency resolution. A window function having a larger time variance can offer better frequency resolution but poorer time resolution than the same with a smaller time variance. However, arbitrarily small resolution in the time as well as in the frequency is restricted by *Heisenbergs uncertainty principle* that states that the product of the time variance and the frequency variance of the signal is lower bounded.

Although STFT offers significant improvement over the Fourier transform, its applicability is severely limited due to two shortcomings. First, for most of the real-time signals, higher resolution in time is desirable for the long lived low frequency features and higher frequency resolution is desirable for the short lived high-frequency features. However with STFT, once a window function is selected, entire signal has to be analyzed with the same time and frequency resolution. Moreover, as the selection for the optimal window function length is not possible, it could involve a fair amount of compromise between the localization in time and frequency.

In order to overcome these shortcomings, a transform that can provide flexibility for the time and frequency resolution could be desirable. More precisely, a transform that can resolve low frequency features of the signal with a longer window function and high frequency feature with shorter window function could be preferred over STFT. In order to obtain a such flexible time-frequency resolutions, a

wavelet transforms are developed based on the idea of using a scaling parameter which depends on the frequency of the signal.

The wavelets meaning a 'little waves'are derived by translation and dilation of a finite energy mother wavelet function $\Psi(t)$. In order to qualify as a wavelet, function $\Psi(t)$ has to satisfy some restrictive conditions [32]. A family of wavelet functions can then be defined as

$$\Psi_{\tau_0,s_0} = \frac{1}{\sqrt{s}}\Psi\left(\frac{t-\tau_0}{s}\right), \qquad s \neq 0 \tag{A.3}$$

where τ_0 is the translation parameter used to traverse along the length of the signal, and s_0 are scale parameter which determines compression or dilation of the mother wavelet. The continuous wavelet transform (CWT) is computed as an inner product of $x(t)$ with Ψ_{τ_0,s_0}, i.e.,

$$\mathrm{CWT}(\tau, s) = \int_{-\infty}^{\infty} \frac{x(t)}{\sqrt{s}}\overline{\Psi_{\tau,s}} \tag{A.4}$$

The wavelet coefficient in the above equation reflects the amount of correlation of the signal with the wavelet function with scale s in the neighbourhood of time τ. The time-frequency tiling with the wavelet transform as compared with the same of STFT in the time-frequency plane is shown in Fig. A.1. Using the CWT coefficients, the original signal $x(t)$ can be reconstructed back as

$$x(t) = \frac{1}{C_\Psi}\int_0^{\infty}\int_{-\infty}^{\infty} \mathrm{CWT}(\tau_0, s_0)\Psi_{\tau_0,s_0}\frac{1}{s^2}ds_0 d\tau_0 \tag{A.5}$$

where the constant

$$C_\Psi = \int_0^{\infty} \frac{|\hat{\Psi}(\Omega)|^2}{\Omega}d\Omega. \tag{A.6}$$

This integral must be finite for perfect reconstruction. This condition is known as 'admissibility condition'of a wavelet function. This condition also implies that $\hat{\Psi}(0) = 0$ meaning $\int_{-\infty}^{\infty}\Psi(t)dt = 0$. Another way to interpretation is that the wavelet function must be a band pass filter.

Although CWT can provide improvement over STFT, it possess following properties which could raise implementation concerns for many practical applications.

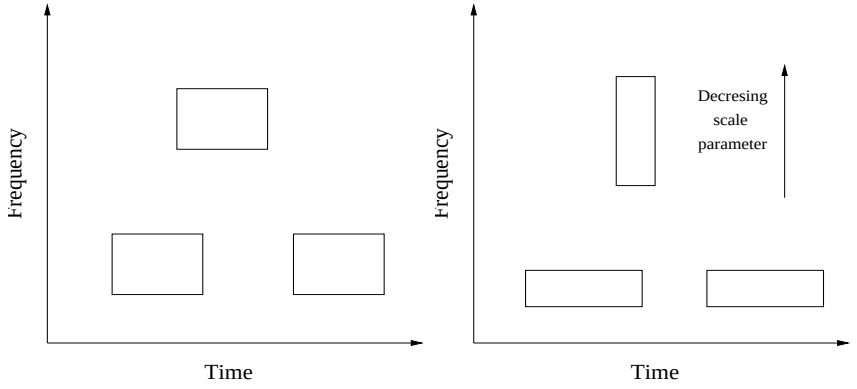

(a) STFT (b) Wavelet transform

FIGURE A.1: Time Frequency tiling with STFT and CWT

First, the CWT coefficients are obtained as a continuum of the inner product between the signal and the wavelet functions with continuous shifting and scaling parameters. As these functions do not form an orthogonal basis, CWT coefficients are highly redundant. For most of the practical applications, this redundancy is unnecessary. Second, even without redundancy, infinite number of wavelet functions are required to decompose the signal and recover it without loss of information.

In order to overcome the first difficulty, the discrete wavelet transform (DWT) has been proposed which evaluates the CWT coefficients at selected scales and translations. A family of discrete wavelets with dyadic translations and dilations is derived by choosing a scale parameter as $s = 2^m, m \in \mathbb{Z}$ and translation parameter as $\tau_0 = n2^m, n \in \mathbb{Z}$. The family of DWT can then be obtained as

$$\Psi_{m,n} = \frac{1}{2^m}\Psi\left(\frac{t - n2^m}{2^m}\right), \qquad s \neq 0 \tag{A.7}$$

By imposing the dyadic scaling and translations proportional to the length of the wavelet, DWT ensures of the orthogonal wavelet functions. Moreover, stretching in time domain by a factor of 2 will compress and shift the frequency spectrum downward by the same factor. Assuming that the wavelet function corresponding to scale parameter $m = 0(s = 1)$ is an ideal band pass filter with pass band of π to 2π. The spectrums for the wavelet functions for different scaling parameter $s = 2^m$, would be non-overlapping as shown in Fig. A.2. It is evident that the ratio between the center frequency of the pass band of the wavelet function and

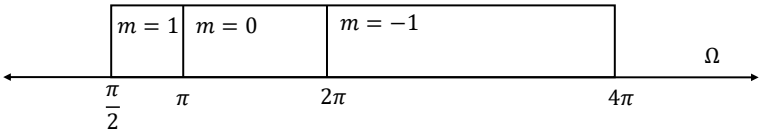

FIGURE A.2: Non-overlapping bands of ideal wavelet filter

the width of this pass band is constant. This ratio is referred to as Q factor of a filter which is constant for each wavelet function.

Every incremental time-stretch of the wavelet function, it can cover only half the uncovered portion of the spectrum. Therefore, in order to cover entire spectrum, infinite number of wavelet functions would be needed. To eliminate this requirement, a scaling function is conceptualized to replace infinite set of wavelet functions by a single function with low pass filter characteristics. Consider that the frequency axis is divided into two parts i.e., low frequency part $\Omega < \Omega_0$ and high frequency part $\Omega > \Omega_0$ where Ω_0 is centre frequency of the mother wavelet. The wavelet decomposition of the signal is performed only for the spectrum with $\Omega > \Omega_0$. In order to recover the signal, the information corresponding to the spectrum range $\Omega < \Omega_0$ must be complemented. Therefore, a scaling function or a father wavelet function $\Phi(t)$ that aggregates wavelet functions corresponding to the spectrum range $0 < \Omega_0$ equivalently with the scales larger than 1 with modulus of its Fourier transform defined as [32]

$$|\hat{\Phi}(\Omega)|^2 = \int_1^\infty |\hat{\Phi}(s\Omega)|^2 \frac{ds}{s} = \int_\Omega^\infty |\hat{\Phi}(\lambda)|^2 \frac{d\lambda}{\lambda}. \tag{A.8}$$

From the above equation and admissibility condition of the wavelet function in (A.6), it is can be derived that

$$\lim_{\Omega \to 0} |\hat{\Phi}(\Omega)|^2 = C_\Psi.$$

This ensures that the scaling function possess the characteristics of a low pass filter. Moreover, just like the wavelet functions, a scaling function can also be scaled and translated to generate family of functions. Therefore, with the introduction of the scaling function, the signal $x(t)$ can be expressed as combination of finite number of wavelet and scaling functions.

Multi-resolution analysis and filtering

The discretization of the scaling parameters also renders important attributes of multiresolution analysis. Consider a signal $x(t)$ approximated by a scaling function with a scale depth m i.e.,$\Phi_{m,n}, n \in \mathbb{Z}$, and vector space spanned by this scaling function is V_m. The coarseness of the estimation depends on the width of the scaling function, i.e, scaling function at scale depth $m+1$ would yield coarser estimation than that with the function at scale depth m. The multiresolution analysis (MRA) of the signal is a family of the approximations of the signal that follow following axioms.

Axioms of MRA

There exists a ladder of subspaces, i.e., $\cdots \subset V_{-2} \subset V_{-1} \subset V_{-0} \subset V_1 \subset V_2 \subset \cdots$ such that

1. $\overline{\{\cup V_m\}}_{m\in\mathbb{Z}} = L_2(\mathbb{R})$
2. $\{\cap V_m\}_{m\in\mathbb{Z}} = \{0\}$
3. There exists $\Phi(t)$ such that, $V_0 = span\Phi(tn), n \in \mathbb{Z}$
4. $\{\Phi(t-n)\}_{n\in\mathbb{Z}}$ is an orthogonal set
5. If $f(t) \in V_m$, then $f(2^m t) \in V_0, \forall m \in \mathbb{Z}$
6. If $f(t) \in V_0$, then $f(t-n) \in V_0, \forall n \in \mathbb{Z}$

Theorem of MRA: *Given the axioms, there exists a function* $\Psi(\cdot) \in L_2(\mathbb{R})$ *such that* $\Psi(2^m t - n)_{m,n\in\mathbb{Z}}$ *spans* $L_2(\mathbb{R})$.

The proof of this theorem can be found in [122]. The space spanned by $\Psi(2^m t - n)$ is denoted by $W_m \subset V_{m-1}$. which contains incremental detail while moving from scale depth m to $m-1$. Specifically,

$$V_{m-1} = V_m \oplus W_m \tag{A.9}$$

Fulfilling above requirements, the familiar dilation relations between the wavelet and scaling functions is given as follows [31]

$$\frac{1}{\sqrt{2}}\Phi(2^{-m}t) = \sum_{n=-\infty}^{\infty} h_a[n]\Phi(2^{(-m-1)}t - n) \tag{A.10}$$

$$\frac{1}{\sqrt{2}}\Psi(2^{-m}t) = \sum_{n=-\infty}^{\infty} g_a[n]\Phi(2^{(-m-1)}t - n) \tag{A.11}$$

$$\tag{A.12}$$

where $h_a[n]$ and $g_a[n], n \in \mathbb{Z}$ can be thought of as the impulse response coefficients of the analysis the filters that produce the coarser approximation and corresponding details for the given approximation. Some important design requirements, namely, vanishing moments, compact support, and regularity can be translated to the conditions on the filters $h_a[n]$ and $g_a[n]$[27]. In order to reconstruct the given approximation from the coarser approximation and corresponding details, a pair of synthesis filters can be designed provided that requirements on alias cancellation and distortion elimination are satisfied [28].

Appendix B

EKF Algorithm

Consider a general discrete time nonlinear stochastic system represented as,

$$\mathbf{x}[k] = f(\mathbf{x}[k-1], \mathbf{u}[k-1]) + \mathbf{w}[k] \tag{B.1}$$

$$\mathbf{z}[k] = h(\mathbf{x}[k]) + \mathbf{w}[k] \tag{B.2}$$

where $\mathbf{x} \in \mathbb{R}^n$ is the state vector, $\mathbf{u} \in \mathbb{R}^m$ is the input vector, $f : \mathbb{R}^{n \times m} \rightarrow \mathbb{R}^n$, $h : \mathbb{R}^n \rightarrow \mathbb{R}^p$, $\mathbf{z}$ is measured vector. k is the sampling instant. $\mathbf{w}[k]$ and $\mathbf{v}[k]$ are random vectors characterizing the uncertainties associated with the process model and measurement noise respectively. They are assumed to be mutually independent, white and normally distributed with zero mean and known variance, i.e., $\mathbf{w} \backsim \mathcal{N}(\mathbf{0}, \mathbf{Q})$, $\mathbf{v} \backsim \mathcal{N}(\mathbf{0}, \mathbf{R})$ where $\mathbf{Q}$ and $\mathbf{R}$ are process covariance matrices for process uncertainties and measurement noise respectively. Moreover, the initial state vector $\mathbf{x}_0$ is assumed to be gaussian distributed random vector with $\mathbf{x}_0 = \mathcal{N}(\hat{\boldsymbol{x}}_0, \mathbf{P}_0)$. $\mathbf{P}$ is covariance of error in the state estimate. The two step discrete time EKF algorithm proceeds as follows.

Step 1: Prediction

$$\hat{\mathbf{x}}[k/k-1] = f(\hat{\mathbf{x}}[k-1], \mathbf{u}[k-1]) \tag{B.3}$$

$$\mathbf{P}[k/k-1] = \mathbf{\Phi}[k]\mathbf{P}[k-1]\mathbf{\Phi}^\top[k] + \mathbf{Q}[k] \tag{B.4}$$

where $\hat{\mathbf{x}}[k+1/k]$ is the *a priori* estimate of the state vector at instant k given the knowledge of the system up to instant $k-1$. $\hat{\mathbf{x}}[k-1]$ is *a posteriori* estimate of the state vector $\mathbf{x}$ at the instant $k-1$. $\mathbf{\Phi}[k] = \frac{\partial f}{\partial x} \mid_{\hat{\mathbf{x}}[k-1],\mathbf{u}[k-1]}$ is the jacobian matrix of system function calculated at instant $k-1$.

Step 2: Correction

$$\begin{aligned}
\boldsymbol{\nu}[k] &= \mathbf{z}[k] - h(\mathbf{x}[k]) && \text{(B.5)}\\
\boldsymbol{\zeta}[k] &= \left(\mathbf{H}\mathbf{P}[k/k-1]\mathbf{H}^{\top} + \mathbf{R}[k]\right) && \text{(B.6)}\\
\mathbf{K}[k] &= \mathbf{P}[k/k-1]H^{\top}\boldsymbol{\zeta}[k]^{-1} && \text{(B.7)}\\
\hat{\mathbf{x}}[k] &= \hat{\mathbf{x}}[k/k-1] + \mathbf{K}[k]\boldsymbol{\nu}[k] && \text{(B.8)}\\
\mathbf{P}[k] &= (I - \mathbf{K}[k+1]\mathbf{H})\mathbf{P}[k/k-1] && \text{(B.9)}
\end{aligned}$$

where $\boldsymbol{\nu}[k]$ denotes the discrepancy between estimated and measured variable. The time series of this term is usually referred to as 'innovation process' as it provides the additional information to the filter. Whiteness property of the term indicates optimality of the filter. The iterative update of the Kalman gain $\mathbf{K}[k]$ ensures optimality of the estimated state vector $\hat{\mathbf{x}}[k]$ by minimizing the error covariance matrix $\mathbf{P}[k]$. For an observable system, the term $\boldsymbol{\zeta}[k]$ is always positive definite thus invertible [44].

Appendix C

PCA based fault detection and isolation

PCA is a *linear* dimensionality reduction technique. It determines a set of orthonormal vectors called principal components (PC), decreasingly ordered by the amount of variance explained in the direction of vectors. Consider the m number of observations of n number of variables stalked in the matrix $\mathbf{X} \in \mathbb{R}^{n \times m}$ as follows

$$\mathbf{X} = \begin{bmatrix} x_{11} & x_{12} & \cdots & x_{1m} \\ x_{21} & x_{22} & \cdots & x_{2m} \\ \vdots & \vdots & \ddots & \vdots \\ x_{n1} & x_{n2} & \cdots & x_{nm} \end{bmatrix} \tag{C.1}$$

If the variables are correlated, it is possible to summarize the variability of the data in a lower p dimensional subspace ($p \ll n$) of the measurement space. Here, p is the number of principal components. In order to obtain the PCA model, eigen-decomposition of the covariance matrix S is computed as

$$S = \frac{1}{m-1} X X^\top = \begin{bmatrix} P & \bar{P} \end{bmatrix} \begin{bmatrix} \Lambda & 0 \\ 0 & \bar{\Lambda} \end{bmatrix} \begin{bmatrix} P & \bar{P} \end{bmatrix}^\top \tag{C.2}$$

where the diagonal matrix $\Lambda \in \mathbb{R}^{p \times p}$ and the columns of the matrix $P \in \mathbb{R}^{n \times p}$ contain the first p largest eigenvalues in the descending order of magnitude and the

corresponding p eigenvectors of the covariance matrix S respectively. Similarly, the diagonal matrix $\bar{\Lambda} \in \mathrm{R}^{(n-p)\times(n-p)}$ and the columns of the matrix $\bar{P} \in \mathbb{R}^{n\times(n-p)}$ contain the remaining $n-p$ eigenvalues in the descending order of magnitude and the corresponding $n-p$ eigenvectors of the covariance matrix S respectively. Columns of matrix P and $\bar{P}$ span PCS and RS respectively.

It is widely accepted and theoretically justified that the principal components corresponding to largest eigenvalues of S characterize most of the dynamic process variations, and principal components corresponding to smaller eigenvalues of S characterize the random noise [123][124]. Therefore, it is important to select the optimum number of principal components to ensure the quality of the PCA model. If the number of PCs is underestimated, the model might miss-out important features of the data. On the contrary, if the number of PCs is overestimated, the model allows more noise which might mask the important features of the data. Various techniques like cumulative percent variance (CPV), the scree test, cross validation, parallel analysis, etc are used for this purpose. Among all these techniques CVP is commonly used its simplicity and ease of computation. It is defined as follows

$$\mathrm{CPV}(l) = \frac{\sum_{i=1}^{l} \lambda_i}{tr(S)}, \tag{C.3}$$

where l is the smallest number of PCs retaining desired % of total variance.

Fault Detection

Once PCA model is developed using the data collected under normal operating conditions, the multivariate sampled vector $\mathbf{x} \in \mathbb{R}^{1\times n}$ scaled to zero mean and unit variance is tested with the fault detection indices. Assuming that Λ is invertible, the Hotteling T-squarred index can be calculated as follows

$$T^2 = \mathbf{x}^\top P \Lambda^{-1} P^\top \mathbf{x} \tag{C.4}$$

T^2 index is sensitive to the variations into PCS as it directly assess the variations along each principal component vectors. In order to measure variations along the RS, SPE index (Q statistic) can be calculated as follows

$$Q = \mathbf{x}^\top \bar{P}\bar{P}^\top \mathbf{x} \tag{C.5}$$

Q statistic measures the random variations of the process. For three dimensional measurement space and two dimensional PCS, a graphical illustration of the T^2 and Q indices are illustrated in Fig. C.1(a). The samples marked with '×' are indicate normal process operation, the 'o' samples indicate the violation of T^2 index, and the samples marked with '+'indicate violation of Q index. It can be noted that the samples violating one index might not violate the other index. Therefore, both the indices need to monitored simultaneously. Alternately, a combined detection statistic, an optimal combination of both the statistics proposed by is defined as follows

$$\varphi = T^2/T_\alpha^2 + Q/Q_\alpha = \mathbf{x}^\top \left(\frac{P\Lambda^{-1}P^\top}{T_\alpha^2} + \frac{\bar{P}\bar{P}^\top}{Q_\alpha}\right)\mathbf{x} \tag{C.6}$$

where T_α^2 and Q_α are control limits for T^2 and Q indices respectively. A graphical illustation of the fault detection with the combined detection index is shown in Fig. C.1(b). In this case also, the samples marked with '×' indicate normal process variation and the samples marked with '-' indicate violation of detection index φ. The unified fault detection index proposed by Alcala et al. [93] is calculated as

$$\text{Index}(\mathbf{x}) = \mathbf{x}^\top \mathbf{M} \mathbf{x}. \tag{C.7}$$

The standard detection indices i.e., Hotelling T^2, SPE, and combined detection index φ can be calculated from this index if $\mathbf{M} = P\Lambda^{-1}P^\top$, $\mathbf{M} = \bar{P}\bar{P}^\top$ and $\mathbf{M} = P\Lambda^{-1}P^\top/T_\alpha^2 + \bar{P}\bar{P}^\top/Q_\alpha$ respectively. Assuming that the measured variables are normally distributed with known mean and variance, the control limit with $(1-\alpha)\times 100\%$ confidence level for the detection Index($\mathbf{x}$), as proposed by Alcala

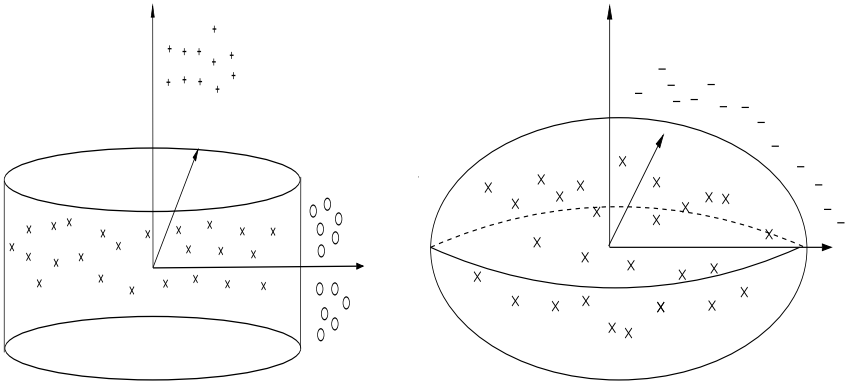

(a) T^2 and Q indices (b) Combined detection index

FIGURE C.1: A graphical illustration of the fault detection schemes

et al. [93] using the results of Box [125] are calculated as

$$\gamma_\alpha = g\chi^2_\alpha(h) \tag{C.8}$$

where $g = \frac{tr([\mathbf{SM}]^2)}{tr(\mathbf{SM})}$ and $h = \frac{[tr(\mathbf{SM})]^2}{tr(\mathbf{SM})}$. Depending upon the expression of M, γ_α will represent the control limit of SPE, Hotteling T^2 or combined detection index.

The fault in the sampled vector $\mathbf{x}$ is detected if Index($\mathbf{x}$) $> \gamma_\alpha$. Once the fault is detected, to identify the root cause of the event, it is necessary to isolate the faulty variables.

Fault isolation

Fault diagnosis task could be very complex for the plant operators and engineers because usually large amount of data are being monitored and as an effect of fault, many of variables could experience out-of-control transients. An objective of the fault isolation procedure is to determine a set of variables most relevant for fault diagnosis. A good assistance regarding the faulty variables can be very useful to the plant operators and engineers to significantly reduce the time to recover the out of control process operation.

Traditionally, univariate statistical methods were employed to isolate faulty variables. In which each variable of the multivariate observation vector was analyzed for its absolute deviations. As this technique do not consider the spacial correlation

among the variables, fault isolation process may fail to identify faulty variables, or it may give too many alarm signals for the variables which may mislead the diagnosis procedure[68].

Contribution analysis is the most popular technique for the fault isolation in PCA framework. It evaluates the contribution of the each variable of the sampled vector into the fault detection index. Consider an alternative expression of Index($\mathbf{x}$) of (C.7)

$$\begin{aligned} \text{Index}(\mathbf{x}) &= \mathbf{x}^\top \mathbf{M}\mathbf{x} = \|\mathbf{M}^{\frac{1}{2}}\mathbf{x}\|^2 \\ &= \sum_{i=1}^{m} \left(\zeta_i^\top \mathbf{M}^{\frac{1}{2}}\mathbf{x}\right)^2 \\ &= \sum_{i=1}^{m} C_i \end{aligned} \tag{C.9}$$

where

$$C_i = \left(\zeta_i^\top \mathbf{M}^{\frac{1}{2}}\mathbf{x}\right)^2 \tag{C.10}$$

denotes the contribution of the variable x_i into Index($\mathbf{x}$). $\boldsymbol{\zeta}_i$ is a column vector representing the suspected variable. It is of length equal to the number of sensors and its j^{th} element is one and the rest of its elements are zero. Moreover, the different forms of the contribution analysis based isolation indices like partial decomposition, angular decomposition, reconstruction based decomposition have also been reported. However, these techniques involve a linear transformation on the sampled vector, consequently a contribution index for the non-faulty variable might get influenced by the faulty variable. This effect is commonly known as 'fault smearing'which might lead to the misdiagnosis.

Bibliography

[1] E. Russell, L. Chiang, and R. Braatz, *Data-driven Methods for Fault Detection and Diagnosis in Chemical Processes*, ser. Advances in Industrial Control. Springer London, 2000.

[2] D. Nelson, *Chernobyl*, ser. PERSPECTIVES on MOD HIST Series. Greenhaven Press, 2010.

[3] T. Moss, D. Sills, and N. Y. A. of Sciences, *The Three Mile Island Nuclear Accident: Lessons and Implications*, ser. Annals of the New York Academy of Sciences. New York Academy of Sciences, 1981.

[4] S. Mukherjee and R. Rai, *Bhopal Gas Tragedy: The Worst Industrial Disaster in Human History, a Book for Young People*, ser. In focus. Tulika Publishers, 2002.

[5] Y. Du, H. Budman, and T. A. Duever, "Comparison of stochastic fault detection and classification algorithms for nonlinear chemical processes," *Computers and Chemical Engineering*, vol. 106, pp. 57 – 70, 2017.

[6] S. Yin, X. Li, H. Gao, and O. Kaynak, "Data-based techniques focused on modern industry: An overview," *IEEE Transactions on Industrial Electronics*, vol. 62, no. 1, pp. 657–667, Jan 2015.

[7] X.-J. Li and G.-H. Yang, "Fault detection for linear stochastic systems with sensor stuck faults," *Optimal Control Applications and Methods*, vol. 33, no. 1, pp. 61–80.

[8] M. Basseville, A. Benveniste, K. C. Chou, and A. S. Willsky, *Multiscale Statistical Signal Processing: Stochastic Processes Indexed by Trees*. Boston, MA: Birkhäuser Boston, 1990, pp. 279–286.

[9] B. R. Bakshi, "Multiscale analysis and modeling using wavelets," *Journal of Chemometrics*, vol. 13, no. 3-4, pp. 415–434, 1999.

[10] R. Braatz, R. Alkire, E. Seebauer, E. Rusli, R. Gunawan, T. Drews, X. Li, and Y. He, "Perspectives on the design and control of multiscale systems," *Journal of Process Control*, vol. 16, no. 3, pp. 193 – 204, 2006, selected Papers from Dycops 7 (2004), Cambridge, Massachusetts.

[11] P. Kokotovi, H. K. Khalil, and J. O'Reilly, *Singular Perturbation Methods in Control: Analysis and Design*. Society for Industrial and Applied Mathematics, 1999.

[12] L. Cohen, *Time-frequency Analysis*, ser. Electrical engineering signal processing. Prentice Hall PTR, 1995.

[13] X. Shen and A. Zayed, *Multiscale Signal Analysis and Modeling*. Springer New York, 2012.

[14] S. Glasstone and A. Sesonske, *Nuclear Reactor Engineering: Reactor Design Basics*, 4th ed., 1994.

[15] S. R. Shimjith, A. P. Tiwari, and B. Bandyopadhyay, "A three-time-scale approach for design of linear state regulator for spatial control of advanced heavy water reactor," *IEEE Transactions on Nuclear Science*, vol. 58, no. 3, pp. 1264–1276, June 2011.

[16] R. Ananthoju, A. P. Tiwari, and M. N. Belur, "A two-time-scale approach for discrete-time kalman filter design and application to ahwr flux mapping," *IEEE Transactions on Nuclear Science*, vol. 63, no. 1, pp. 359–370, Feb 2016.

[17] G. Y. Park, J. Park, and P. H. Seong, "Application of wavelet noise-reduction technique to water-level controller," *Nuclear Technology*, vol. 145, no. 2, pp. 177–188, 2004.

[18] G. Espinosa-Paredes, A. Nez-Carrera, A. Prieto-Guerrero, and M. Ceceas, "Wavelet approach for analysis of neutronic power using data of ringhals stability benchmark," *Nuclear Engineering and Design*, vol. 237, no. 10, pp. 1009 – 1015, 2007.

[19] M. Antonopoulos-Domis and T. Tambouratzis, "System identification during a transient via wavelet multiresolution analysis followed by spectral techniques," *Annals of Nuclear Energy*, vol. 25, no. 7, pp. 465 – 480, 1998.

[20] T. Bhatt, S. Shimjith, A. Tiwari, K. Singh, S. Singh, K. Singh, and R. Patil, "Estimation of sub-criticality using extended kalman filtering technique," *Annals of Nuclear Energy*, vol. 60, pp. 98 – 105, 2013.

[21] L. Hong, L. Chen, and C. Chui, "A filter-bank-based kalman filtering technique for wavelet estimation and decomposition of random signals," *Circuits and Systems II: Analog and Digital Signal Processing, IEEE Transactions on*, vol. 45, no. 2, pp. 237–241, Feb 1998.

[22] B. R. Bakshi, "Multiscale pca with application to multivariate statistical process monitoring," *AIChE Journal*, vol. 44, no. 7, pp. 1596–1610.

[23] E. Vanhatalo and M. Kulahci, "The effect of autocorrelation on the hotelling t2 control chart," *Quality and Reliability Engineering International*, vol. 31, no. 8, pp. 1779–1796, 2015.

[24] D. Gabor, "Theory of communication," *Journal of the Institution of Electrical Engineers - Part I: General*, vol. 94, no. 73, pp. 58–, January 1947.

[25] A. Haar, "Zur theorie der orthogonalen funktionensysteme," *Mathematische Annalen*, vol. 69, no. 3, pp. 331–371, 1910.

[26] A. Grossmann and J. Morlet, "Decomposition of hardy functions into square integrable wavelets of constant shape," *SIAM Journal on Mathematical Analysis*, vol. 15, no. 4, pp. 723–736, 1984.

[27] S. G. Mallat, "A theory for multiresolution signal decomposition: the wavelet representation," *IEEE Transactions on Pattern Analysis and Machine Intelligence*, vol. 11, no. 7, pp. 674–693, July 1989.

[28] M. Vetterli, "Filter banks allowing perfect reconstruction," *Signal Processing*, vol. 10, no. 3, pp. 219 – 244, 1986.

[29] J. E. Fowler, "The redundant discrete wavelet transform and additive noise," *IEEE Signal Processing Letters*, vol. 12, no. 9, pp. 629–632, Sep. 2005.

[30] H. S. Dhiman, P. Anand, and D. Deb, "Wavelet transform and variants of svr with application in wind forecasting," in *Innovations in Infrastructure*, D. Deb, V. E. Balas, and R. Dey, Eds. Singapore: Springer Singapore, 2019, pp. 501–511.

[31] G. Strang and T. Nguyen, *Wavelets and Filter Banks*. Wellesley-Cambridge Press, 1996.

[32] S. Mallat, *A Wavelet Tour of Signal Processing, Third Edition: The Sparse Way*, 3rd ed. Academic Press, Inc., 2008.

[33] P. Vaidyanathan, *Multirate Systems and Filter Banks*, ser. Prentice-Hall signal processing series. Prentice Hall, 1993.

[34] J. Kovacevic and M. Vetterli, *Wavelets and Subband Coding*, ser. Prentice-Hall signal processing series. Prentice Hall PTR, 1995.

[35] K. Ogata, *Modern Control Engineering*, ser. Instrumentation and controls series. Prentice Hall, 2010.

[36] R. E. Kalman, "A new approach to linear filtering and prediction problems," *Transactions of the ASME–Journal of Basic Engineering*, vol. 82, no. Series D, pp. 35–45, 1960.

[37] J. Patel and C. Read, *Handbook of the Normal Distribution, Second Edition*, ser. Statistics: A Series of Textbooks and Monographs. Taylor & Francis, 1996.

[38] M. Zingsheim, G. Mllemann, D. Shute, and K. Nienhaus, "Applications of kalman filtering and inertial navigation in future autonomous mining methods," *Mining Report*, vol. 149, no. 5, pp. 304–308, 2013.

[39] B. O. S. Teixeira, M. A. Santillo, R. S. Erwin, and D. S. Bernstein, "Spacecraft tracking using sampled-data kalman filters," *IEEE Control Systems Magazine*, vol. 28, no. 4, pp. 78–94, Aug 2008.

[40] K. P. Vishwakarma, "Prediction of economic time-series by means of the kalman filter," *International Journal of Systems Science*, vol. 1, no. 1, pp. 25–32, 1970.

[41] P. Zarchan and H. Musoff, *Fundamentals of Kalman Filtering: A Practical Approach*, ser. Fundamentals of Kalman filtering: a practical approach. American Institute of Aeronautics and Astronautics, Incorporated, 2000, no. v. 190.

[42] H. Sorenson, *Kalman Filtering: Theory and Application*, ser. IEEE Press selected reprint series. IEEE Press, 1985.

[43] A. Haug, *Bayesian Estimation and Tracking: A Practical Guide*. Wiley, 2012.

[44] P. Maybeck, *Stochastic Models, Estimation and Control*, ser. Mathematics in science and engineering. Academic Press, 1979, no. pt. 1.

[45] Y. Shimazu, Y. Nakano, Y. Tahara, and T. Okayama, "Development of a compact digital reactivity meter and a reactor physics data processor," *Nuclear Technology*, vol. 77, no. 3, pp. 247 – 254, 1987.

[46] J. Ma, J. Fan, L. Lv, and L. Ma, "Reactivity estimation of nuclear reactor combined with neural network and mechanism model," in *2012 IEEE Power and Energy Society General Meeting*, July 2012, pp. 1–6.

[47] J. Duderstadt and L. Hamilton, *Nuclear Reactor Analysis*. Wiley, 1976.

[48] J. H. Perez-Cruz and A. Poznyak, "Estimation of the precursor power and internal reactivity in a nuclear reactor by a neural observer," in *Electrical and Electronics Engineering, 2007. ICEEE 2007. 4th International Conference on*, Sept 2007, pp. 310–313.

[49] D. Simon, *Optimal State Estimation: Kalman, H Infinity, and Nonlinear Approaches*. Wiley, 2006.

[50] S. Ansari, "Development of on-line reactivity meter for nuclear reactors," *Nuclear Science, IEEE Transactions on*, vol. 38, no. 4, pp. 946–952, Aug 1991.

[51] S. Kay, *Fundamentals Of Statistical Signal Processing*, ser. Prentice-Hall signal processing series. Prentice Hall, 2001.

[52] A. Racz, "On the estimation of a small reactivity change in critical reactors by kalman filtering technique," *Annals of Nuclear Energy*, vol. 19, no. 9, pp. 527 – 538, 1992.

[53] Z. Dong, *Robust Kalman Filter with Application to State Estimation of a Nuclear Reactor*. INTECH Open Access Publisher, 2010.

[54] R. B. e Silva, A. Marques, J. Cruz, K. Shirvan, and M. Kazimi, "Reactivity estimation during a reactivity-initiated accident using the extended kalman filter," *Annals of Nuclear Energy*, vol. 85, pp. 753 – 762, 2015.

[55] Y. Shimazu and W. van Rooijen, "Qualitative performance comparison of reactivity estimation between the extended kalman filter technique and the inverse point kinetic method," *Annals of Nuclear Energy*, vol. 66, pp. 161 – 166, 2014.

[56] X. Peng, Y. Cai, Q. Li, and K. Wang, "Comparison of reactivity estimation performance between two extended kalman filtering schemes," *Annals of Nuclear Energy*, vol. 96, pp. 76 – 82, 2016.

[57] M. Z. Ygane and G. Ansarifar, "Extended kalman filter design to estimate the poisons concentrations in the p.w.r nuclear reactors based on the reactor power measurement," *Annals of Nuclear Energy*, vol. 101, pp. 576 – 585, 2017.

[58] S. B. Patel, S. Mukhopadhyay, and A. Tiwari, "Estimation of reactivity and delayed neutron precursors' concentrations using a multiscale extended kalman filter," *Annals of Nuclear Energy*, vol. 111, no. Supplement C, pp. 666 – 675, 2018.

[59] H. N. Nounou and M. N. Nounou, "Multiscale fuzzy kalman filtering," *Engineering Applications of Artificial Intelligence*, vol. 19, no. 5, pp. 439 – 450, 2006.

[60] E. L. Haseltine and J. B. Rawlings, "Critical evaluation of extended kalman filtering and moving-horizon estimation," *Industrial & Engineering Chemistry Research*, vol. 44, no. 8, pp. 2451–2460, 2005.

[61] C. V. Rao, J. B. Rawlings, and D. Q. Mayne, "Constrained state estimation for nonlinear discrete-time systems: stability and moving horizon approximations," *IEEE Transactions on Automatic Control*, vol. 48, no. 2, pp. 246–258, Feb 2003.

[62] D. Simon, "Kalman filtering with state constraints: a survey of linear and nonlinear algorithms," *IET Control Theory Applications*, vol. 4, no. 8, pp. 1303–1318, August 2010.

[63] N. Gupta, "Kalman filtering in the presence of state space equality constraints," in *2007 Chinese Control Conference*, July 2007, pp. 107–113.

[64] P. Vachhani, R. Rengaswamy, V. Gangwal, and S. Narasimhan, "Recursive estimation in constrained nonlinear dynamical systems," *AIChE Journal*, vol. 51, no. 3, pp. 946–959, 2005.

[65] S. Yin, S. Ding, X. Xie, and H. Luo, "A review on basic data-driven approaches for industrial process monitoring," *Industrial Electronics, IEEE Transactions on*, vol. 61, pp. 6418–6428, 11 2014.

[66] J. E. Jackson, "Quality control methods for several related variables," *Industrial Quality Control*, vol. 1, no. 4, pp. 359–377, 1959.

[67] J. Jackson, "Quality control methods for several related variables," *Technometrics*, vol. 1, no. 4, pp. 359–377, 1959.

[68] T. Kourti and J. F. MacGregor, "Multivariate spc methods for process and product monitoring," *Journal of Quality Technology*, vol. 28, no. 4, pp. 409–428, 1996.

[69] K. P. F.R.S., "Analysis of a complex of statistical variables into principal componentse," *The London, Edinburgh, and Dublin Philosophical Magazine and Journal of Science*, vol. 2, no. 11, pp. 559–572, 1901.

[70] B. Wise, N. Ricker, D. Veltkamp, and B. Kowalski, "A theoretical basis for the use of principal component models for monitoring multivariate processes," *Process Control and Quality*, vol. 1, 11 1990.

[71] S. Wold, K. Esbensen, and P. Geladi, "Principal component analysis," *Chemometrics and Intelligent Laboratory Systems*, vol. 2, no. 1, pp. 37 – 52, 1987.

[72] S. Yin, S. X. Ding, X. Xie, and H. Luo, "A review on basic data-driven approaches for industrial process monitoring," *IEEE Transactions on Industrial Electronics*, vol. 61, no. 11, pp. 6418–6428, Nov 2014.

[73] J. V. Kresta, J. F. Macgregor, and T. E. Marlin, "Multivariate statistical monitoring of process operating performance," *The Canadian Journal of Chemical Engineering*, vol. 69, no. 1, pp. 35–47, 1991.

[74] B. M. Wise and N. B. Gallagher, "The process chemometrics approach to process monitoring and fault detection," *Journal of Process Control*, vol. 6, no. 6, pp. 329 – 348, 1996.

[75] H. Hotelling, "On lines and planes of closest fit to systems of points in space," *Journal of Educational Psychology*, vol. 24, no. 7, pp. 498–520, 1993.

[76] S. J. Qin, "Data-driven fault detection and diagnosis for complex industrial processes," *IFAC Proceedings Volumes*, vol. 42, no. 8, pp. 1115 – 1125, 2009.

[77] H. Yue and J. Qin, "Reconstruction-based fault identification using a combined index," *Industrial and Engineering Chemistry Research*, vol. 40, pp. 4403–4414, 10 2001.

[78] W. Li and S. Qin, "Consistent dynamic pca based on errors-in-variables subspace identification," *Journal of Process Control*, vol. 11, no. 6, pp. 661 – 678, 2001.

[79] Q. Jiang, X. Yan, and B. Huang, "Performance-driven distributed pca process monitoring based on fault-relevant variable selection and bayesian inference," *IEEE Transactions on Industrial Electronics*, vol. 63, no. 1, pp. 377–386, Jan 2016.

[80] M. Mansouri, M. Nounou, H. Nounou, and N. Karim, "Kernel pca-based glrt for nonlinear fault detection of chemical processes," *Journal of Loss Prevention in the Process Industries*, vol. 40, pp. 334 – 347, 2016.

[81] S. Gajjar, M. Kulahci, and A. Palazoglu, "Real time fault detection and diagnosis using sparse principal component analysis," *Journal of Process Control*, vol. 67, pp. 112 – 128, 2018, big Data: Data Science for Process Control and Operations.

[82] M. Misra, H. Yue, S. Qin, and C. Ling, "Multivariate process monitoring and fault diagnosis by multi-scale pca," *Computers & Chemical Engineering*, vol. 26, no. 9, pp. 1281 – 1293, 2002.

[83] Haitoa Zhang, A. K. Tangirala, and S. I. Shah, "Dynamic process monitoring using multiscale pca," vol. 3, May 1999, pp. 1579–1584 vol.3.

[84] M. Z. Sheriff, M. Mansouri, M. N. Karim, H. Nounou, and M. Nounou, "Fault detection using multiscale pca-based moving window glrt," *Journal of Process Control*, vol. 54, pp. 47 – 64, 2017.

[85] A. A. Kalgonda and S. R. Kulkarni, "Multivariate quality control chart for autocorrelated processes," *Journal of Applied Statistics*, vol. 31, no. 3, pp. 317–327, 2004.

[86] J. E. Jarrett and X. Pan, "Monitoring variability and analyzing multivariate autocorrelated processes," *Journal of Applied Statistics*, vol. 34, no. 4, pp. 459–469, 2007.

[87] T. Rato, M. Reis, E. Schmitt, M. Hubert, and B. De Ketelaere, "A systematic comparison of pca-based statistical process monitoring methods for high-dimensional, time-dependent processes," *AIChE Journal*, vol. 62, no. 5, pp. 1478–1493, 2016.

[88] Y. Dong and S. J. Qin, "A novel dynamic pca algorithm for dynamic data modeling and process monitoring," *Journal of Process Control*, vol. 67, pp. 1 – 11, 2018, big Data: Data Science for Process Control and Operations.

[89] J. A. Westerhuis, S. P. Gurden, and A. K. Smilde, "Generalized contribution plots in multivariate statistical process monitoring," *Chemometrics and Intelligent Laboratory Systems*, vol. 51, no. 1, pp. 95 – 114, 2000.

[90] S. J. Qin and W. Li, "Detection and identification of faulty sensors in dynamic processes," *AIChE Journal*, vol. 47, no. 7, pp. 1581–1593, 2001.

[91] S. Yoon and J. F. MacGregor, "Fault diagnosis with multivariate statistical models part i: using steady state fault signatures," *Journal of Process Control*, vol. 11, no. 4, pp. 387 – 400, 2001.

[92] R. Dunia and S. J. Qin, "A unified geometric approach to process and sensor fault identification and reconstruction: the unidimensional fault case," *Computers & Chemical Engineering*, vol. 22, no. 7-8, pp. 927–943, 1998.

[93] C. F. Alcala and S. J. Qin, "Analysis and generalization of fault diagnosis methods for process monitoring," *Journal of Process Control*, vol. 21, no. 3, pp. 322 – 330, 2011.

[94] P. V. den Kerkhof, J. Vanlaer, G. Gins, and J. F. M. V. Impe, "Contribution plots for statistical process control: Analysis of the smearing-out effect," in *2013 European Control Conference (ECC)*, July 2013, pp. 428–433.

[95] Z. Zhou, C. Wen, and C. Yang, "Fault isolation based on k-nearest neighbor rule for industrial processes," *IEEE Transactions on Industrial Electronics*, vol. 63, no. 4, pp. 2578–2586, April 2016.

[96] C. F. Alcala and S. J. Qin, "Reconstruction-based contribution for process monitoring," *Automatica*, vol. 45, no. 7, pp. 1593 – 1600, 2009.

[97] J. Liu, "Fault diagnosis using contribution plots without smearing effect on non-faulty variables," *Journal of Process Control*, vol. 22, no. 9, pp. 1609 – 1623, 2012.

[98] K. Liu, X. Jin, Z. Fei, and J. Liang, "Adaptive partitioning pca model for improving fault detection and isolation," *Chinese Journal of Chemical Engineering*, vol. 23, no. 6, pp. 981 – 991, 2015.

[99] P. V. den Kerkhof], J. Vanlaer, G. Gins, and J. F. V. Impe], "Analysis of smearing-out in contribution plot based fault isolation for statistical process control," *Chemical Engineering Science*, vol. 104, pp. 285 – 293, 2013.

[100] Z. Yan and Y. Yao, "Process fault isolation via bayesian lasso-based reconstruction analysis," in *27th European Symposium on Computer Aided Process Engineering*, ser. Computer Aided Chemical Engineering, A. Espua, M. Graells, and L. Puigjaner, Eds. Elsevier, 2017, vol. 40, pp. 1669 – 1674.

[101] S. Ren, F. Si, J. Zhou, Z. Qiao, and Y. Cheng, "A new reconstruction-based auto-associative neural network for fault diagnosis in nonlinear systems," *Chemometrics and Intelligent Laboratory Systems*, vol. 172, pp. 118 – 128, 2018.

[102] D. Hetrick, *Dynamics of Nuclear Reactors*. University of Chicago Press, 1971.

[103] P. Maybeck, *Stochastic Models, Estimation, and Control*, ser. Mathematics in Science and Engineering. Elsevier Science, 1982.

[104] I. Daubechies, *Ten Lectures on Wavelets*. Philadelphia, PA, USA: Society for Industrial and Applied Mathematics, 1992.

[105] D. Coppersmith and S. Winograd, "Matrix multiplication via arithmetic progressions," *Journal of Symbolic Computation*, vol. 9, no. 3, pp. 251 – 280, 1990, computational algebraic complexity editorial.

[106] K. Sasidharan, D. Khatri, K. Singh, and A. Srivastav, "Refurbishment and core conversion of the apsara reactor," *Nuclear engineering and design*, vol. 236, no. 7, pp. 784–795, 2006.

[107] S. S. Amit Mishra, A. P. Tiwari, "Digital dynamic compensation techniques for delayed self-powered neutron detectors," *Symposium on Advances in Control and Instrumentation (SACI-2014)*, vol. 24, pp. 330–332, June 2014.

[108] G. M. Ljung and G. E. P. Box, "On a measure of lack of fit in time series models," *Biometrika*, vol. 65, no. 2, pp. 297–303, 1978.

[109] J. C. Venerus and T. E. Bullock, "Estimation of the dynamic reactivity using digital kalman filtering," *Nuclear Science and Engineering*, vol. 40, no. 2, pp. 199–205, 1970.

[110] P. Gill, W. Murray, and M. Wright, *Numerical linear algebra and optimization.* Addison-Wesley, 1991, vol. 1.

[111] F. A. Potra and S. J. Wright, "Interior-point methods," *Journal of Computational and Applied Mathematics*, vol. 124, no. 1, pp. 281 – 302, 2000.

[112] B. R. P. R. G. Srinivasan, K.V. Suresh Kumar, "The fast breeder test reactordesign and operating experiences," *Nuclear Engineering and Design*, vol. 236, pp. 796–811, 2006.

[113] C. S. Subudhi, T. U. Bhatt, and A. P. Tiwari, "A mathematical model for total power control loop of large phwrs," *IEEE Transactions on Nuclear Science*, vol. 63, no. 3, pp. 1901–1911, June 2016.

[114] "Design manual on reactor physics," *NPCIL Report no. TAPP-3 and 4/DM/01100/Rev.1*, 2006.

[115] D. L. Donoho and J. M. Johnstone, "Ideal spatial adaptation by wavelet shrinkage," *Biometrika*, vol. 81, no. 3, p. 425, 1994.

[116] E. Vanhatalo and M. Kulahci, "Impact of autocorrelation on principal components and their use in statistical process control," *Quality and Reliability Engineering International*, vol. 32, no. 4, pp. 1483–1500, 2016.

[117] J. Downs and E. Vogel, "A plant-wide industrial process control problem," *Computers & Chemical Engineering*, vol. 17, no. 3, pp. 245 – 255, 1993, industrial challenge problems in process control.

[118] L. Van Eykeren, Q. Chu, and J. Mulder, "Sensor fault detection and isolation using adaptive extended kalman filter*," *IFAC Proceedings Volumes*, vol. 45, no. 20, pp. 1155–1160, 2012, 8th IFAC Symposium on Fault Detection, Supervision and Safety of Technical Processes.

[119] M. B. Shams, H. Budman, and T. Duever, "Fault detection using cusum based techniques with application to the tennessee eastman process," *IFAC Proceedings Volumes*, vol. 43, no. 5, pp. 109–114, 2010, 9th IFAC Symposium on Dynamics and Control of Process Systems.

[120] W. H. Woodall and M. M. Ncube, "Multivariate cusum quality-control procedures," *Technometrics*, vol. 27, no. 3, pp. 285–292, 1985.

[121] J. Proakis and D. Manolakis, *Digital Signal Processing*, ser. Prentice Hall international editions. Pearson Prentice Hall, 2007.

[122] E. Chandrasekhar, V. Dimri, and V. Gadre, *Wavelets and Fractals in Earth System Sciences*. Taylor & Francis, 2013.

[123] J. MacGregor and T. Kourti, "Statistical process control of multivariate processes," *Control Engineering Practice*, vol. 3, no. 3, pp. 403 – 414, 1995.

[124] I. Jolliffe and Springer-Verlag, *Principal Component Analysis*, ser. Springer Series in Statistics. Springer, 2002.

[125] G. E. P. Box, "Some theorems on quadratic forms applied in the study of analysis of variance problems, i. effect of inequality of variance in the one-way classification," *The Annals of Mathematical Statistics*, vol. 25, no. 2, pp. 290–302, 1954.

Thesis Highlight

Name of the Student: Shri. Shrenik Babulal Patel
Name of the CI/OCC: Bhabha Atomic Research centre **Enrolment No.:** ENGG01201404022
Thesis Title: State Estimation and Multivariate Process Monitoring in Multiscale Framework
Discipline: Engineering Sciences **Sub-Area of Discipline:** Electrical Engineering
Date of viva voce: 10th April, 2021

In this thesis, various state estimation techniques for the complex nonlinear system, e.g., nuclear reactor are proposed. In order to exploit multi-scale nature of the system, a multiscale model structure is formulated by projecting the states of nonlinear autonomous system on the family of wavelets and scaling and functions as a basis. The Extended Kalman Filtering (EKF) algorithm is employed on the system model thus derived in the wavelet projection space. The performance of the proposed multi-scale EKF algorithm is assessed by comparing the same with the standard EKF algorithm using the simulation results obtained with various plant datasets. The simulation results suggest a significant improvement of the estimation results as compared with that with the standard EKF technique. However, the proposed technique has poses two key constraints in the its formulation, i.e., its applicable only to the class of autonomous systems, and estimation is non-casual. In order to overcome these limitations while retaining merits of multi-scale EKF, a formulation based on stationary wavelet transform (SWT) is also proposed. The proposed technique permits working with the forced nonlinear systems, and same is validated by simulation results obtained by a reference dataset of Pressurized Heavy Water Reactor (PHWR). In order to handle the physical constraints on the system, i.e., non-negative values of the reactor power and delayed neutron precursors' concentrations, a constrained state estimator based on the recursive non-linear dynamic data reconciliation (RNDDR) technique has been proposed. The effectiveness of the proposed RNDDR technique is assessed by the simulation results obtained for different transients. Moreover, a new multi-scale PCA based MSPM technique for effective fault-detection and isolation of variables associated with the onsite fault has been proposed. The proposed multi-scale PCA method is validated with the simulation results obtained for a numerical problem as well as for the benchmark Tennessee Eastman process data. The proposed multi-scale PCA method comply with the implicit assumptions of the PCA based multivariate statistical process monitoring. The simulation results suggest that the proposed technique outperform the standard PCA based technique.